Freie Universität Berlin

Magnetotelluric study of the Western Cordillera (Northern Chile), with a focus on Lascar volcano

Dissertation
zur Erlangung des Doktorgrades
der Naturwissenschaften
am Fachbereich Geowissenschaften
der Freien Universität Berlin

vorgelegt von

Daniel Díaz Alvarado

Berlin, 2011

Erster Gutachter: Prof. Dr. S. Shapiro
Zweiter Gutachter: PD Dr. O. Ritter
Tag der Disputation: 14.03.2011

Erklärung

Hiermit versichere ich, daß ich die vorliegende Arbeit selbständig verfaßt und keine anderen als die angegebenen Hilfsmittel benutzt habe. Die Stellen der Arbeit, die anderen Werken wörtlich oder inhaltlich entnommen sind, wurden durch entsprechende Angaben der Quellen kenntlich gemacht.

Diese Arbeit hat in gleicher oder ähnlicher Form noch keiner Prüfungsbehörde vorgelegen.

Abstract

The Andes are one of the best examples of active orogenic processes in the world, due to the interaction between the Nazca and South American plates. In the central part of this orogen, this interaction led to the Altiplano-Puna plateau, the second in height and extent after Tibet. This plateau is related with abundant arc magmatism, particularly between 21°45’S and 23°30’S, a zone characterized by the Altiplano-Puna volcanic complex, with huge volumes of Neogene ignimbrites and numerous volcanic centers of Miocene to Holocene age.

In zones where the temperature and presence of fluids are playing an important role, the application of geophysical methods recovering the electrical resistivity, strongly controlled by these factors, is particularly interesting. In the Central Andes, the subducted Nazca plate is releasing fluids which ascend and generate partial melts in the asthenospheric wedge. More locally, the active volcanic centers are normally associated with hydrothermal systems and the presence of magma. Both processes, at their different scales, are directly linked and conform the aim of this work.

Between September and November 2007 and during a second field campaign in January and February 2010, long period magnetotelluric (LMT) stations were set following an E-W profile around 23°40’S, starting at the Cordillera de Domeyko, crossing the Salar de Atacama and reaching the Puna. A more focused study, using audio magnetotelluric (AMT) sites, was carried out around Lascar volcano, a subduction-related stratovolcano located in the Altiplano-Puna volcanic complex, with an historical activity characterized by fumarolic emissions and occasional vulcanian explosions, the largest one observed during April 1993.

Remote reference and robust techniques were used in the data processing. Induction arrows, phase tensor ellipses and strike direction of the conductivity distribution have been calculated for both data sets as dimensionality indicators, obtaining different results. The AMT sites around the volcano are showing a strong 3D behavior for shallower depths, with induction vectors at the closest sites to the volcano pointing away from it, influenced by the topography and by local conductivity heterogeneities. For the large period data from the profile, the behavior is more 2D with a more stable strike direction which is coherent with the induction vectors and the largest semi axis of the phase tensor ellipses. All these parameters are strongly influenced for the longer periods by a large highly conductive anomaly in the backarc, beneath the Argentinean Puna.

Sensitivity analysis for different cases of synthetic magmatic chambers beneath Lascar volcano have been performed using 3D forward modeling tools. Conductive zones with different shapes and sizes were tried at various depths beneath the volcano in order to check the presence of a magma chamber, but no single conductive zone below the volcanic edifice could explain the magnetotelluric responses of the stations around it. However, models including a conductive zone extending to the south-southeast of the volcano improved strongly the fit with the measured data. This conductive zone is located in the middle of several volcanic centers, limited to the north by Lascar and Aguas Calientes volcanoes, and to the south by the Puntas Negras volcanic chain and the Chiliques volcano, suggesting a more complicated magmatic system which could be related with more than one of the volcanic centers in the area.

2D models obtained from the inversion of the LMT profile data are showing good agreement with the largest features of this area, as the Cordillera de Domeyko or the Salar de Atacama basin, and also showing the presence of the highly conductive anomaly previously referred by the dimensionality parameters, extending between 20 and at least 80 km depth. The presence of this conductive anomaly beneath the Puna and not beneath the active volcanic arc in the Western Cordillera, may provide new evidence on the upward pathway of fluids from the subducting slab, and therefore on the formation of volcanic centers in the Central Andes.

Zusammenfassung

Die Anden, entstanden durch die Subduktion der Nazca-Platte unter die Südamerikanische Platte, sind eines der besten Beispiele für aktive orogene Prozesse auf der Erde. Im zentralen Bereich dieses Orogens führte diese Interaktion zur Herausbildung des Altiplano-Puna-Plateaus, dem nach Tibet zweithöchsten weltweit. Dieses Plateau ist durch ausgedehnten Magmatismus gekennzeichnet, speziell in der Region zwischen 21°45’S und 23°30’S. Diese Zone ist geprägt durch große Volumen neogener Ignimbrite und zahlreiche vulkanische Zentren miozänen und holozänen Alters.

In Gebieten, in denen Temperaturanomalien und die Anwesenheit von Fluiden eine große Rolle spielen, ist insbesondere die Anwendung von geophysikalischen Methoden von Interesse, die die elektrische Leitfähigkeit bestimmen, da diese stark durch Temperatur und Fluide beeinflusst wird. In den Zentralen Anden steigen aus der subduzierten Nazca-Platte Fluide auf, welche in der Asthenosphäre zu partiellen Schmelzen führen. In einem lokalen Maßstab assoziiert man die vulkanischen Zentren allgemein mit hydrothermalen Systemen und der Anwesenheit von Magma. Beide Prozesse, in ihrem unterschiedlichen Maßstab, sind direkt miteinander verbunden und das Ziel dieser Arbeit.

Zwischen September und November 2007 und während einer zweiten Messkampagne im Januar und Februar 2010 wurden langperiodische magnetotellurische (LMT) Meßstationen auf einem E-W streichenden Profil bei ungefähr 23°40’S aufgebaut, beginnend in der Cordillera de Domeyko, über den Salar de Atacama und den Vulkanbogen bis zur Puna. Eine genauere Untersuchung mit

Hilfe von Audiomagnetotellurik (AMT) wurde um den Vulkan Lascar durchgeführt. Dieser durch Subduktionsprozesse entstandene Stratovulkan zeigte in historischer Zeit fumarolische Aktivität und gelegentlich explosive Eruptionen, die größte davon beobachtet im April 1993.

Zum Processing der Daten wurden Remote-Reference und robuste Verfahren angewendet. Induktionspfeile, Phasentensor-Ellipsen und Streichrichtungen der Leitfähigkeitsverteilungen wurden für beide Datensätze als Dimensionalitätsindikatoren berechnet, mit unterschiedlichen Ergebnissen. Die AMT-Stationen um den Vulkan zeigen bei geringen Tiefen starke 3D-Effekte. Die Induktionspfeile der dem Vulkan am nächsten gelegenen Stationen zeigen von diesem weg, da sie durch Topographie und lokale Leitfähigkeitsheterogenitäten beeinflusst sind. Für die langperiodischen Profildaten ist das Verhalten eher 2D mit einer stabileren Streichrichtung, welche kohärent mit den Induktionspfeilen und den großen Halbachsen der Phasentensor-Ellipsen ist. Alle diese Parameter sind stark von einer hochleitfähigen Anomalie im Backarc unter der argentinischen Puna beeinflusst.

Für verschiedene synthetische Magmakammern-Geometrien unterhalb des Lascar wurden Sensitivitätsanalysen mit Hilfe von 3D-Vorwärts-Modellierungen durchgeführt. Leitfähigkeitszonen unterschiedlicher Gestalt und Größe wurden in verschiedenen Tiefen getestet, um das Vorhandensein einer Magmakammer zu überprüfen. Jedoch konnte kein einzelner Leiter unterhalb des vulkanischen Komplexes die magnetotellurischen Daten an den vulkannahen Stationen erklären. Erst Modelle, die eine Leitfähigkeitszone beinhalten, welche sich süd-südöstlich vom Vulkan erstreckt, konnten die Anpassung des Modells signifikant verbessern. Diese Leitfähigkeitszone befindet sich im Zentrum verschiedener vulkanischer Zentren, im Norden begrenzt durch die Vulkane Lascar und Aguas Calientes, im Süden durch die Puntas Negras-Kette und den Vulkan Chiliques. Dies lässt ein komplizierteres magmatisches System vermuten, welches mit mehr als einem vulkanischen Zentrum in der Region verbunden sein könnte.

2D-Modelle, die durch die Inversion der LMT-Profildaten erzeugt wurden, zeigen eine gute Übereinstimmung mit den größten in dieser Region vorkommenden Strukturen, wie der Cordillera de Domeyko oder dem Salar de Atacama-Becken im Forearc. Sie zeigen außerdem eine hochleitfähige Anomalie zwischen 20 und 80 km Tiefe im Backarc. Die Lage der Leitfähigkeitsanomalie unterhalb der Puna und nicht etwa unterhalb des aktiven Vulkanbogens in der Western Cordillera gibt neue Hinweise auf den Pfad der von der subduzierten Platte aufsteigenden Fluide und damit auf die Entstehung der vulkanischen Zentren in diesem Teil der Anden.

Resumen

Los Andes es uno de los mejores ejemplos de procesos orogénicos activos en el mundo, debido a la interacción entre las placas de Nazca y Sudamericana. En la parte central de este orógeno, esta interacción llevó a la formación de la meseta del Altiplano-Puna, la segunda en altura y extensión después de Tíbet. Esta meseta está relacionada con abundante magmatismo de arco, en particular entre los 21°45'S y 23°30'S, una zona caracterizada por el complejo volcánico Altiplano-Puna, que presenta enormes volúmenes de ignimbritas Neógenas y numerosos centros volcánicos formados durante el Mioceno y el Holoceno.

En zonas donde la presencia de fluidos y la temperatura juegan un rol importante, la aplicación de métodos geofísicos que permitan obtener la resistividad eléctrica, fuertemente controlada por estos factores, es particularmente interesante. En los Andes Centrales, la subducción de la placa de Nazca libera fluidos que al ascender generan fusión parcial en la Astenósfera. A nivel más local, los centros volcánicos activos están normalmente asociados con sistemas hidrotermales y la eventual presencia de magma. Ambos procesos, en sus diferentes escalas, están directamente vinculados y forman parte de los objetivos de este trabajo.

Entre Septiembre y Noviembre de 2007, y durante una segunda campaña de terreno en Enero y Febrero de 2010, se instalaron estaciones magnetotelúricas de período largo (LMT) en el perfil EW en torno a los 23°40'S, desde de la Cordillera de Domeyko, cruzando el Salar de Atacama y el arco volcánico, hasta llegar a la Puna. Un estudio más enfocado, con el uso de estaciones de audiomagnetotelúrica (AMT), se llevó a cabo alrededor del volcán Lascar, un estratovolcán de orígen subductivo situado en el complejo volcánico del Altiplano-Puna, con una actividad histórica caracterizada por constantes emisiones fumarólicas y explosiones vulcanianas ocasionales, la mayor de ellas observada durante abril de 1993.

Técnicas de referencia remota y procesamiento robusto fueron utilizados en el procesamiento de datos. Flechas de inducción, elipses de tensor de fase y la dirección de rumbo geoeléctrico se han calculado para ambos conjuntos de datos como indicadores de dimensionalidad, obteniendo diferentes resultados. Las estaciones de AMT alrededor del volcán muestran un comportamiento claramente 3D a escasa profundidad, con las flechas de inducción en los sitios más cercanos al volcán apuntando lejos de él, influenciadas por la topografía y la presencia de heterogeneidades conductivas locales. Para los datos de periodo largo en el perfil EW, el comportamiento se acerca a un caso 2D con una dirección de rumbo más estable, que es coherente con los vectores de inducción y el semi-eje mayor de las elipses del tensor de fase. Todos estos parámetros están fuertemente influenciados para los períodos más largos por una anomalía de alta conductividad en el tras-arco, bajo la Puna argentina.

Utilizando herramientas de modelamiento 3D, se han realizado análisis de sensibilidad considerando distintos casos de cámaras magmáticas sintéticas bajo el volcán Lascar. Zonas conductoras con diferentes formas y tamaños fueron analizadas a distintas profundidades bajo el volcán a fin de verificar la presencia de una posible cámara magmática, pero ninguna zona conductora

individual bajo el edificio volcánico ha logrado explicar las respuestas magnetotelúricas de las estaciones a su alrededor. Sin embargo, los modelos que incluyen una zona conductora que se extiende al sur-sureste del volcán, mejoran notablemente el ajuste con los datos medidos. Esta zona conductora se encuentra en medio de varios centros volcánicos, siendo limitada al norte por los volcanes Lascar y Aguas Calientes, y al sur por la cadena volcánica de Puntas Negras y el volcán Chiliques, lo que sugiere un sistema magmático complejo que podría estar relacionado con más de uno de los centros volcánicos en la zona.

Los modelos 2D obtenidos de la inversión de los datos del perfil LMT muestran una buena concordancia con los rasgos más característicos de esta zona, como son la Cordillera de Domeyko y la cuenca del Salar de Atacama, e incluye también la presencia de la anomalía de alta conductividad previamente inferida por los parámetros de dimensionalidad, que se extiende bajo el trasarco, entre 20 y al menos 80 km de profundidad. La presencia de esta anomalía conductora bajo la Puna y no bajo el arco volcánico activo en la Cordillera Occidental, puede proporcionar nuevas evidencias sobre el recorrido ascendente de los fluidos liberados en el proceso de subducción, y por lo tanto de la formación de centros volcánicos en los Andes Centrales.

Contents

Abstract, Zusammenfassung, Resumen **1**

1 Introduction **8**

2 Geology of the study zone **12**

2.1 Regional Geologic and Tectonic setting 12

2.2 Evolution of Lascar volcano 21

3 Theoretical background of Magnetotellurics **25**

3.1 1-D case 27

3.2 2D case, TE and TM modes 29

3.3 Impedance Tensor 30

4 Data processing and analysis **33**

4.1 Data processing 33

4.2 Dimensionality and distortion analysis 36

4.2.1 Induction vectors 37

4.2.2 Galvanic distortions and Skew parameters 40

4.2.3 Determination of the regional strike direction 44

4.2.4 Phase tensor analysis 48

5 Inversions and Models **54**

5.1 2D Inversion of LMT data 54

5.2 3D forward modeling 64

5.2.1 The effect of different scenarios around a measuring point 66

5.2.2 Topographic effect 70

5.2.3 Modeling the conductivity structure beneath the volcano 73
5.3 3D inversion of AMT data 86
6 Interpretation of the measured data 92
6.1 3D modeling results around Lascar volcano 92
6.2 LMT data and 2D inversion 100
7 Conclusions and comments 108
References 110
List of figures 120
Acknowledgments 126
Curriculum Vitae 127

Chapter 1

Introduction

The Central Andes have formed in a long lasting convergent system where, since Jurassic times, several oceanic plates were subducted under the South American plate. Subduction resulted in the formation of a magmatic arc that, due to tectonic erosion, has migrated about 200 km eastwards since 120 Ma, moving from the Coastal Cordillera to its present position in the Western Cordillera (Scheuber et al., 2006). Here, at the western border of South America, the Central Andes are characterized by the Altiplano-Puna plateau, one of the largest plateaus in the world, and the highest related with abundant arc magmatism, with the main volcanic located at its western border, along the Western Cordillera. These structures and other characterizing this area are shown in figure 1.1.

In the subduction zone of the Central Andes several high conductivity zones have been detected (e.g. Schilling et al. (1997); Lezaeta and Brasse (2001); Brasse and Eydam (2008)), mostly in areas where shear zones are present and/or magmatism has occurred recently, for which fluids and/or partial melting are the most common explanations. Fluids released from the slab facilitate partial melting at lower crustal - upper mantle depths, by reducing the melting point of the rocks. At shallow depths, fluids may circulate in the crust without leading to partial melting, particularly in a brittle crust which has been folded and fractured by tectonic deformation, resulting in a considerable electrical conductivity enhancement provided that these are rich in minerals and that they find a pathway to circulate, which is possible in fault zones. Around active volcanic centers, hydrothermal systems as well as magmatic sources are characterized by a high electrical conductivity, and consequently form ideal targets for geophysical techniques sensitive to conductivity, as the magnetotelluric sounding method.

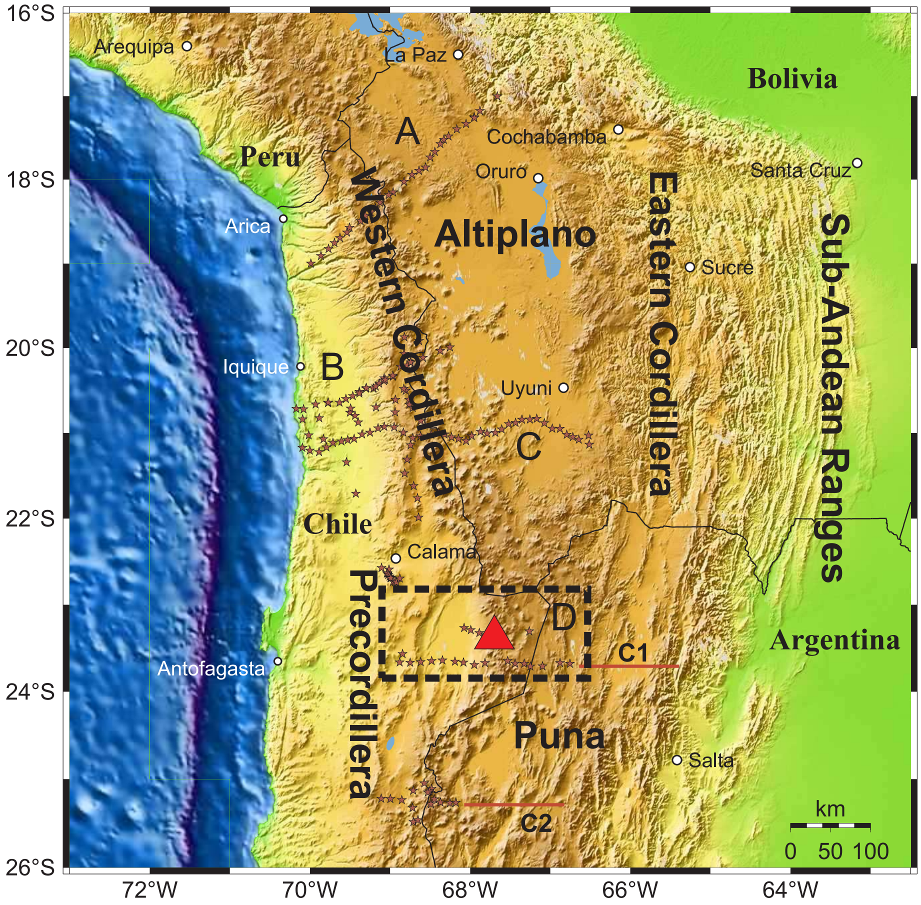

Figure 1.1: Main structures characterizing the Central Andes. Red stars show the location of magnetotelluric profiles (A, B, C and D) in the Central Andes, with results described in: A) Brasse and Eydam (2008); B) Echternacht et al. (1997); Lezaeta (2001); C) Lezaeta (2001); Brasse et al. (2002); Schwalenberg et al. (2002); D) this work. Lines C1 and C2 are planned profile prolongations for future field campaigns. Red triangle indicates the position of Lascar volcano, and the dashed rectangle the location of figure 1.2.

Magnetotellurics (MT) is an electromagnetic sounding method which belongs to the geophysical techniques governed by the diffusion equation. Measurements of period-dependent fluctuations in the electric and magnetic fields on the surface of the Earth can be used to obtain information of the resistivity distribution in depth. As the resistivity of rocks in the Earth extends over a very wide range, the MT method is a useful tool to image the resistivity distribution of the subsurface, in shallow crustal to mantle depth studies. Several magnetotelluric studies have been developed in different volcanic zones around the world during the last years, interpreting electrical conductors as hydrothermal fluids (Ingham et al., 2009), clays (Matsushima et al., 2001), and also magmatic conduits or chambers, included in several 3-D modeling studies (Ingham et al., 2009; Müller and Haak, 2004; Hill et al., 2009).

The area enclosed by a segmented line in figure 1.1 is a very particular zone in the Central Andes, where the volcanic arc, following a characteristic north-south trend, is interrupted by one of the largest sedimentary basins of the Central Andes, the Salar de Atacama. The volcanic arc, at the western border of the Salar de Atacama, is shifted 50 km to the east compared to its north and southward continuations. In this segment is located one of the most active volcanoes of the Central Andes during the last 20 years, the Lascar volcano. This volcano, with an activity characterized by repetitive dome growth and subsidence, accompanied by degassing and explosive eruptions of different magnitudes, was particularly active during the 1990's, with its largest recorded eruptive episode in April 1993, with an eruptive column reaching more than 20 km height. Tephra fell over large areas of Brazil, Argentina, Paraguay and Uruguay (Matthews et al., 1997).

Data acquisition was performed during October and November of 2007, and during a second field campaign in early 2010, following the few access routes crossing the volcanic arc in this zone. The AMT stations were placed in the area around Lascar volcano, forming a ring and a short profile across the volcano. The LMT stations were set up more to the south as a profile from the highest lands to the Atacama basin. Figure 1.2 shows the study zone and the sites where the magnetotelluric stations were built.

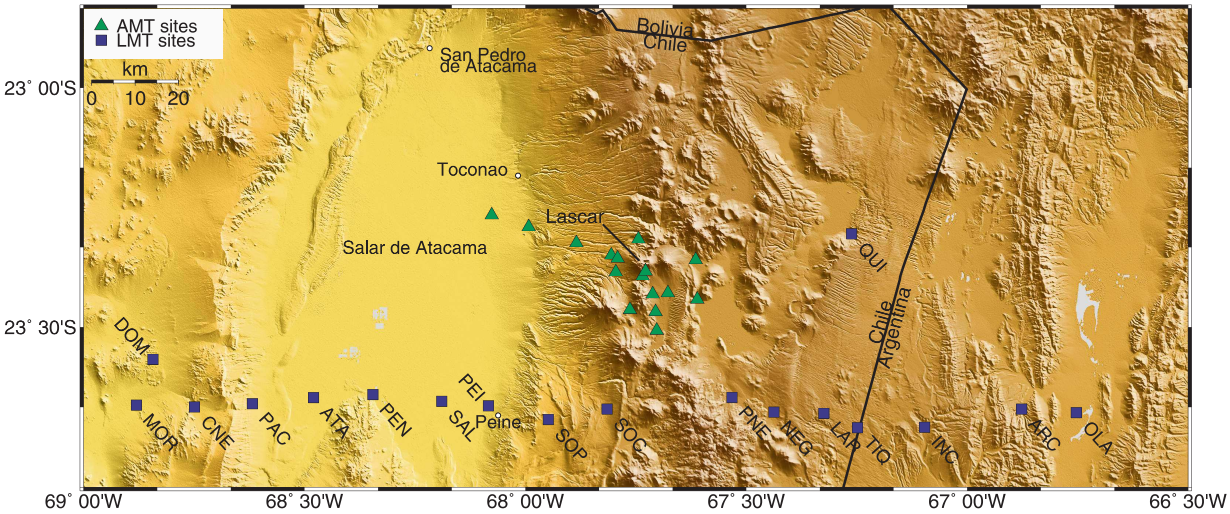

Figure 1.2: Study zone and location of sites. Green triangles are AMT stations and blue squares are LMT stations.

In this thesis, the goal is to obtain two models:

- An electric conductivity model of the crust and upper mantle of the forearc, magmatic arc and backarc in the Central Andean subduction zone, at latitudes around 23.7 °S and longitudes between 66.5 - 69 °W, using long-period instruments (LMT), comparing the results obtained from the magnetotellurics with other geophysical observations and the geological background, trying to obtain a joint interpretation.

- An electric conductivity model of Lascar volcano and its surroundings using broadband instruments (AMT), trying to check the electrical properties of the shallower crust around the volcano, and the presence of a magmatic chamber associated with it.

The first part of this work comprises the geological background of the study zone (chapter 2), followed by the theoretical basis of the magnetotelluric sounding method in chapter 3. The data processing will be clarified in chapter 4, together with a dimensionality analysis considering both data sets (from the AMT and LMT data) separately, showing the convenience of a three-dimensional or two-dimensional approach in each case. In chapter 5 the 3D and 2D models obtained for each case will be presented, and the interpretation of the most important features of these results will be discussed in chapter 6, followed by some final remarks in chapter 7.

Chapter 2

Geology of the study zone

Since the origins of the plate tectonics theory, the Andes have been quoted as one of the best examples in the world, of active orogenic processes due to interaction between oceanic and continental plates. Due to these interactions, the Andes have become a place of great interest for scientists of all over the world. Here it is possible to observe the result of millions of years of deformation processes which have transformed the landscape several times, and that are still in motion.

Starting with an overview of the geology of the Central Andes, this chapter will focus in the area between the Coastal Cordillera and the Puna around 23.5°S, and finally in the Lascar volcano area.

2.1 Regional Geologic and Tectonic setting

The Central Andes are formed in a long lasting convergent system in which, since Jurassic times, several oceanic plates were subducted under the South American plate. Subduction resulted in the formation of a magmatic arc that, due to tectonic erosion, has migrated about 200 km eastwards since 120 Ma, moving from the Coastal Cordillera to its present position in the Western Cordillera (Scheuber et al., 2006). Between 15° and 34°S, this segment of the Andes is constituted principally of continental material, which differs from the northern and southern part of the Andes, partly constituted by oceanic material accreted in the continent. It comprises the highest peaks of this mountain range and some of the most active volcanoes in the world.

The convergence between these two plates has been estimated in several studies (DeMets et al., 1990; Norabuena et al., 1998; Kendrick et al., 2003), with an average convergence velocity of 79 mm/y under the Central Andes and a direction of N77°E (DeMets et al., 1994; Somoza, 1998). The direction of convergence has not varied significantly in the last 20 Ma, while the velocity seems to have experienced some variations during this period (Pardo-Casas and Molnar, 1987; Somoza, 1998).

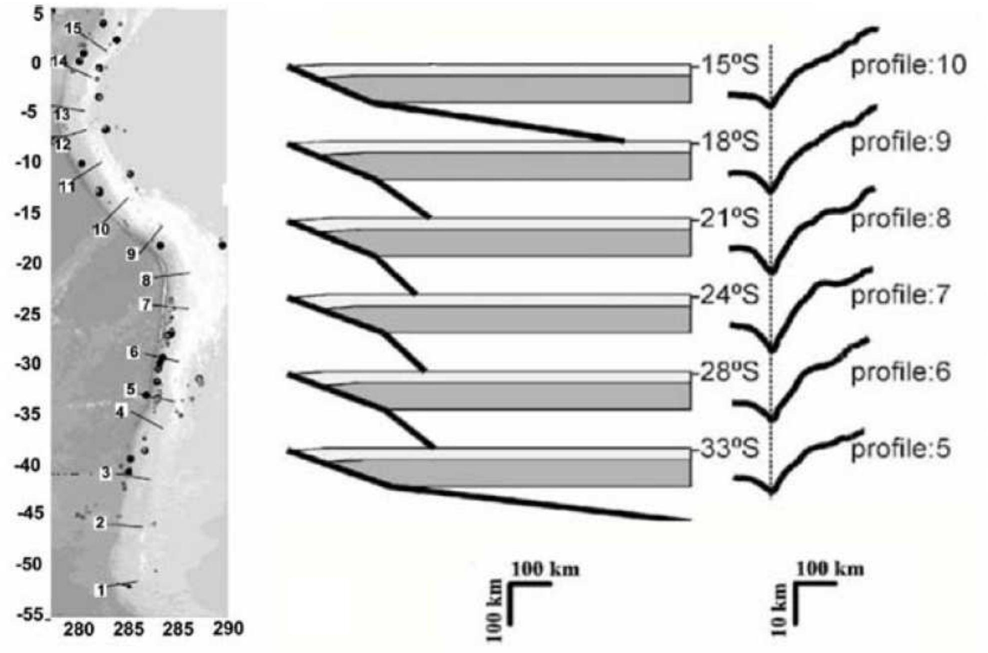

Figure 2.1: Variation of the Wadati-Benioff plane in the Central Andes and bathymetric-topographic profiles (Yañez and Cembrano, 2004)

The region in study is placed at the western border of the Bolivian Orocline (13°-28°S), a morphological division between the northern and southern Central Andes. In this zone, the Central Andes consist of major structural units which approximately parallel the trend of the mountain range. In the central part, where the Andes attain their maximum width, they comprise four regions, from west to east, (1) the offshore and onshore fore-arc region, (2) the Western Cordillera that marks the location of the presently active magmatic arc, (3) the Altiplano-Puna high plateau, and (4) an eastern belt of fold and thrust structures comprising the Eastern Cordillera, the Sub-Andean Ranges and the Sierras Pampeanas (Oncken et al., 2006). With around 1800 km of extent in the back-arc region, from southern Peru through Bolivia (Altiplano), northern Argentina and Chile (Puna), a width between 350 - 400 km, and an average altitude of $\sim$ 4 km (higher in the Puna), the Altiplano-Puna plateau is the second only to Tibet in height and extent, and the highest plateau in the world that is associated with abundant arc magmatism (Allmendinger et al., 1997). This plateau is mainly considered to be a consequence of large crustal shortening. However, there are still some discrepancies between the observed tectonic shortening, and the amount of material needed to explain the entire crustal thickness (Farías et al., 2005).

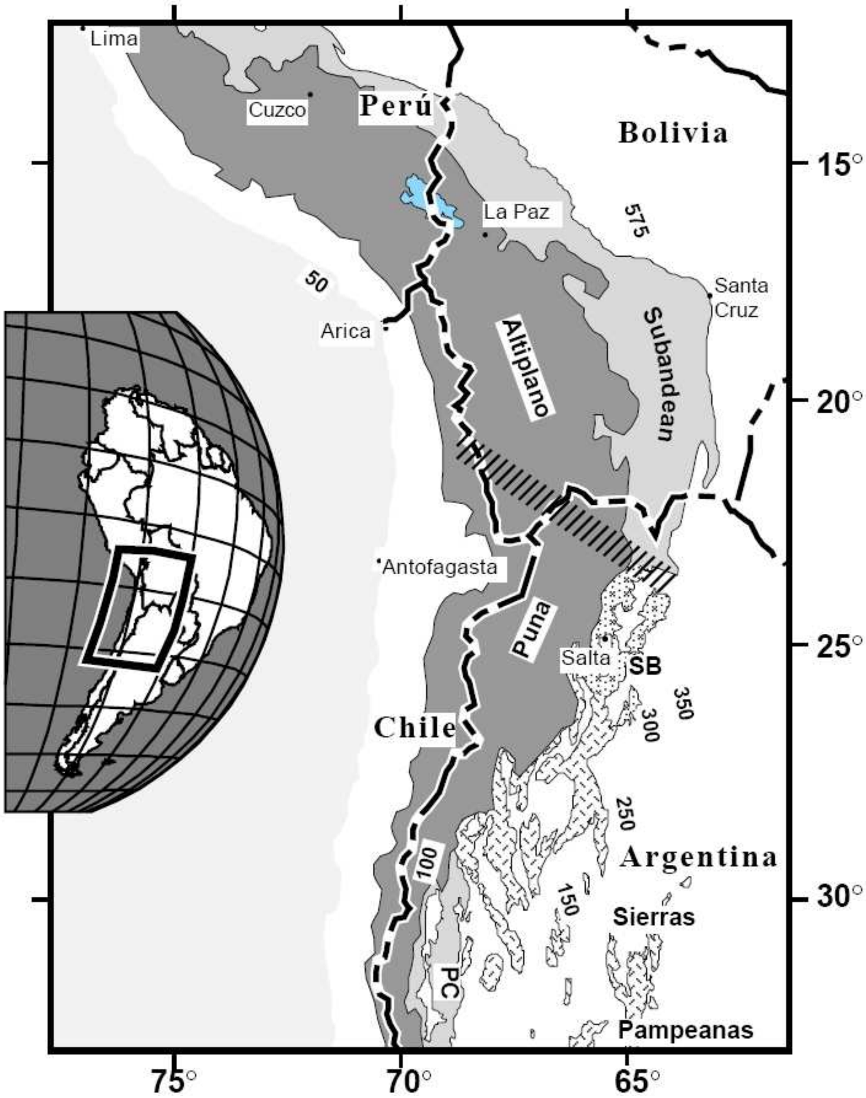

Figure 2.2: Location map showing the extent of the high plateau of the Central Andes. Dark gray shows area above 3 km elevation; the plateau is defined by the wide area above 3 km between 13 and 27°S. The light gray zones are thin-skinned thrust belts in the Subandean ranges of Bolivia/Peru and the Precordillera (PC) in Argentina. The Sierras Pampeanas and Santa Barbara System (SB) are thick-skinned foreland provinces. The hachured zone trending NW-SE across the Argentine-Bolivian border corresponds to a variety of lateral change in Andean and pre-Andean features, and can be considered as the Altiplano-Puna boundary (Allmendinger et al., 1997).

Morphological differences between the Altiplano and the Puna, has an average elevation nearly a kilometer higher in the Puna than in the Altiplano, has been attributed to greater thinning of the lithosphere beneath the Puna (Whitman et al., 1996).

The Altiplano-Puna plateau is limited in the north and south by an almost horizontal Benioff plane angle at depth, estimated between 7° and 9° (Gutscher et al., 1999, 2000), while under the Bolivian Orocline, this Benioff plane angle in depth reaches 44° (David et al., 2002). This variation of the Benioff plane seems to be a consequence of the subduction of the Nazca and the Juan Fernandez ridges at the northern and southern border of the Bolivian Orocline, respectively.

Concentrating in the westernmost regions, the geology of the fore-arc is influenced by earlier magmatic arcs and associated sedimentary basins of Jurassic to Paleogene age. It records at least two pre- Neogene shortening events, the Cretaceous Peruvian stage and, most notably, the late Eocene Incaic phase. Neogene tectonism has produced in the Chilean fore-arc normal faulting with uplift in the west (Coastal Cordillera) and thrust or reverse faults of limited throw in the east (Kuhn, 2002; Victor et al., 2004). Young volcanics cover almost all of the Western Cordillera, which apparently experienced little Neogene deformation (Scheuber and Reutter, 1992).

Around 23°S, the Central Andean arc is retreated 60 km eastwards from its regional north-south trend, reaching a maximum distance from the Perú-Chile trench of about 400 km. To the west, the Central Andean arc is limited by the Salar de Atacama, a major topographic anomaly placed at 2300 m above sea level, and following to the west is possible to find morphological features such as the Cordillera de La Sal, Llano de la Paciencia, El Bordo Escarpment, and the Cordillera de Domeyko.

The Cordillera de Domeyko is an Eocene magmatic and tectonic belt exhuming late Palaeozoic felsic igneous rocks (Mpodozis and Ramos, 1989), which north of 25°S is related to a west-verging, high-angle structural system that propagated slowly to the west during the Neogene (Muñoz and Charrier, 1996; Victor et al., 2004). Its eastern border coincides with the El Bordo Escarpment where, overlying the Paleozoic and Triassic basement, a thick succession of Cretaceous to Miocene continental sediments, including the Purilactis Group, is exposed. Further east the Llano de la Paciencia is a narrow 80 km long N-S, and 8 km wide sub-basin filled by coalescing Quaternary alluvial fans separated from the main Salar de Atacama basin by the Cordillera de la Sal, a still tectonically active N-S ridge of complexly deformed Oligocene-Pliocene, evaporite-rich, continental sediments and ignimbrites. Further to the east, but unexposed, the Purilactis Group also forms the lower section of the Llano de la Paciencia and part of the modern Salar de Atacama basin sedimentary fill (Mpodozis et al., 2005).

On the Salar de Atacama, multiple models of its tectonic evolution have been published. Flint et al. (1993) propose that the Salar de Atacama Basin evolved under extensional tectonic conditions through the Mesozoic and Cenozoic periods. Muñoz et al. (1997) propose that the basin began as a Cretaceous extensional basin that was subsequently inverted by east-directed thrusting during the late Cretaceous. Arriagada et al. (2002) and Mpodozis et al. (2005) present evidence that during the late Cretaceous, the basin began in a compressional setting as a foreland basin linked to the initial stages of uplift of the Cordillera de Domeyko, emphasizing that the basin forming event was the inversion of the Jurassic-early Cretaceous extensional Tarapacá backarc basin.

The main structural style of the Salar de Atacama area is given by first-order kilometric scale ∼NS and east-vergent thrust faults (Aron et al., 2008). Subsidiary to these main faults, there is a second order thin-skinned system (Kuhn, 2002) with similar orientation to the first-order structures. The fold and thrust belt architecture related to the first and second-order faults, controls the landscape of the Precordillera and the Salar de Atacama basin.

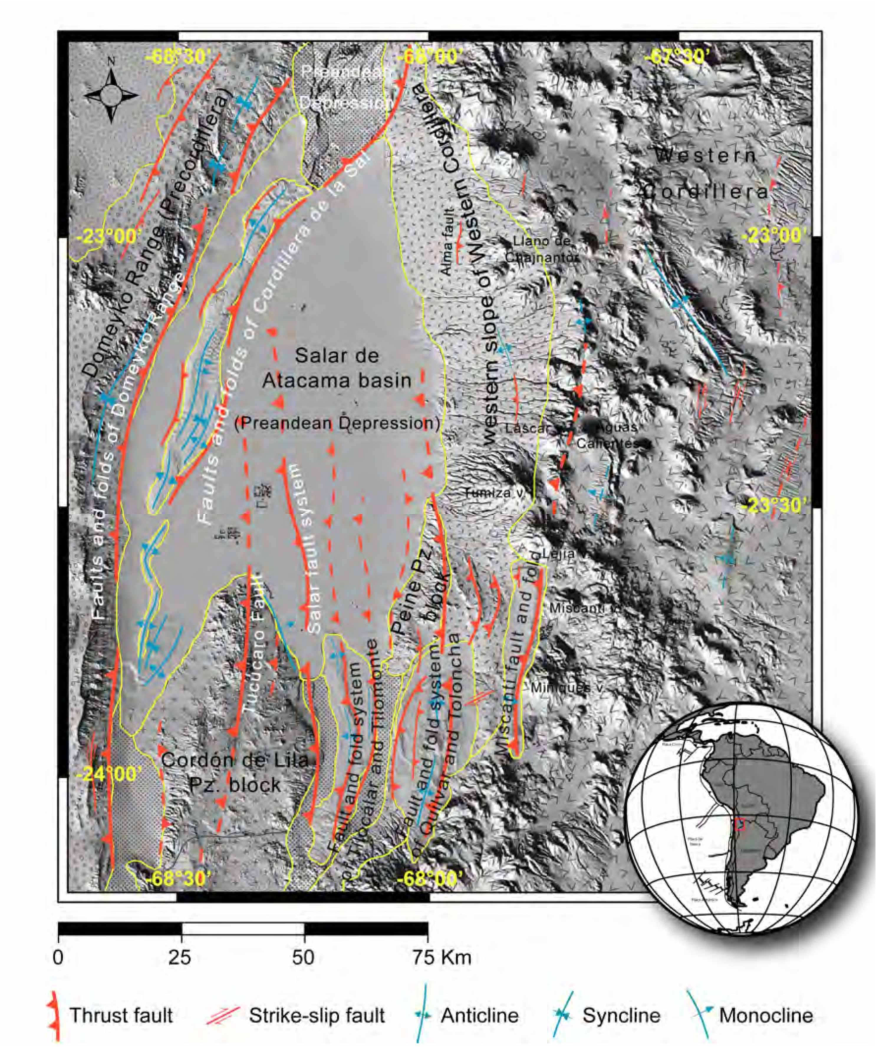

Figure 2.3: Structural map of the Salar de Atacama area showing some of the first and second order faults controlling the structural style of this area. Extracted from Aron et al. (2008).

There is evidence of an 80 km long structure along the active magmatic arc, the so-called Miscanti Fault (also called Callejón Varela). This fault represents the easternmost expression of the fold-and-thrust belt. The ca. 400 meters high structural relief of the Miscanti Fault controls the development of intra-arc lakes (Miscanti and Miñiques lakes) and the local and spatial extension of andesitic-basaltic lavas erupted from nearby volcanic centers (Aron et al., 2008). Some of these structures are shown in figure 2.3.

Several geophysical studies have been developed in this zone, including refraction seismics (Schmitz et al., 1999), local earthquake tomography (Graeber and Asch, 1999; Schurr and Rietbrock, 2004), receiver functions studies (Yuan et al., 2000), and gravity field measurements (Götze et al., 1994). These studies support the idea of a thick crust (>60 km) beneath the Salar de Atacama, finding a rheologically strong block with low attenuation (high Q_p) and high v_p values (see figure 2.4) surrounded by a relatively weak zone and a high in the residual gravity around this basin, which supports the idea of this strong block, called the Atacama Block by Schurr and Rietbrock (2004). According to this last referred study the composition of the Atacama Block should be an even mixture of quartz-rich gneiss and metabasites, because with this mixed composition it is possible to fit the v_p and v_p/v_s ratio and because this composition can be related to investigated high-pressure, low-temperature rocks that crop out in the Sierra de Limon Verde (NW of the Salar de Atacama).

The western Altiplano-Puna plateau margin forms a huge monocline that lacks prominent Neogene deformation structures. The origin of this monocline has been a subject of debate, putting in the table several hypothesis. Isacks (1988) has suggested that uplift of this margin was the result of flexure of the crust as a response to late Miocene underthrusting from the east. More recently,Muñoz and Charrier (1996), Farias et al. (2002) and García et al. (2002) have reported the occurrence of steeply east dipping reverse faults with low shortening magnitudes at the base of the monocline between 18°30’ and 19°30’S that they dated to be Miocene in age. They suggested a thrust-related uplift of the western Altiplano crust paralleled by surface tilting from deep processes. Lamb et al. (1997) explained the monocline as a gigantic tilted block of upper crust that collapsed and rotated between the subvertical Atacama and Precordilleran Fault Systems during Plio-Pleistocene plateau uplift. On a smaller scale,Wörner et al. (2000) describe similar large-scale antithetic block rotations at 18°S induced by gravitational collapse of the plateau flank. In addition, deformation of parts of the forearc has been shown to be dominated by vertical axis block rotations that have been either attributed to oroclinal bending of the Andes (Isacks, 1988; MacFadden et al., 1995; Kuhn, 2002) or to oblique subduction during the Cenozoic (Beck, 1988; Randall et al., 1996).

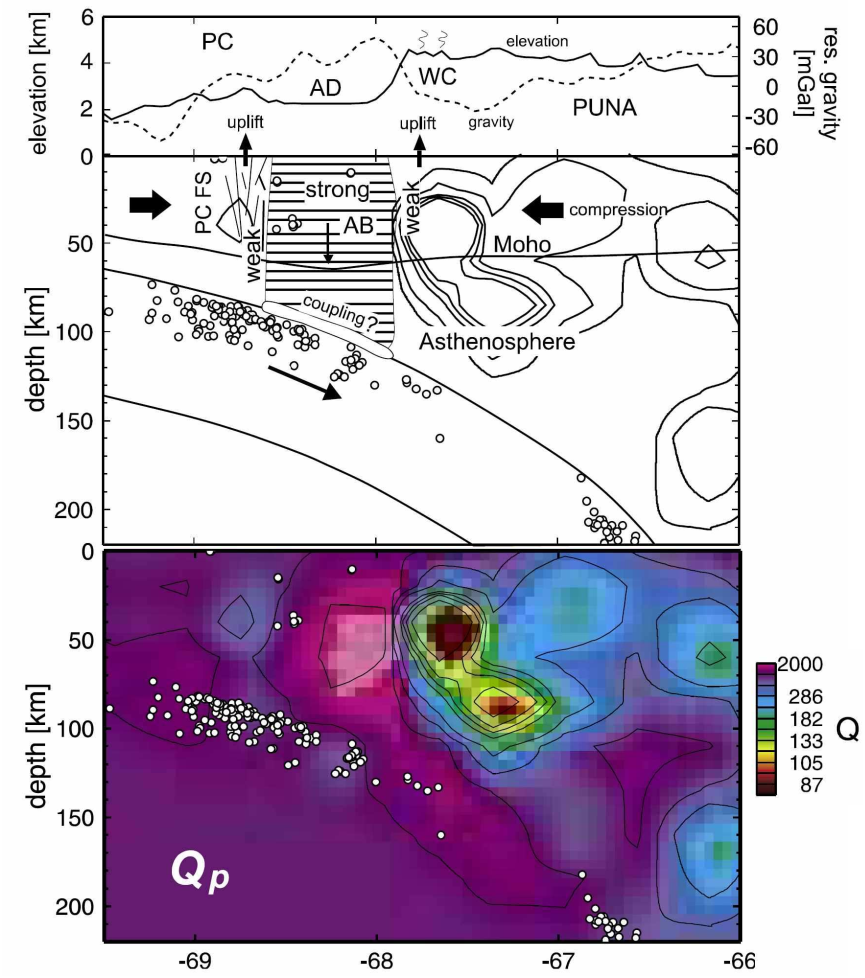

Figure 2.4: Topography, residual gravity, and interpretational cross section through the Salar de Atacama basin at 23.2°S. Abbreviations are as follows: PC - Precordillera, PCFS - Precordilleran fault system, AD - Salar de Atacama depression, AB - Atacama block, WC - Western Cordillera (extracted and edited from Schurr and Rietbrock (2004)).

Concentrating on our study area, the Neogene deformation zones are controlled by fault systems following preferably three directions, Orogen parallel (N-S), as the Precordillera fault system, NE-striking faults, such as the Uyuni-Kehnayani fault, and NW-trending faults (Salfity, 1985), as the Olacapato-El Toro (or Calama-Olacapato-El Toro) fault system. The NW-striking fault zones are generally associated with Neogene volcanic centers (Matteini et al., 2002b; Petrinovic et al., 2005) and are characterized by a significant component of horizontal, fault-normal dilation (Riller et al., 2001). In contrast to these zones, the orogen-parallel and NE-trending fault systems consist mostly of reverse faults, which generally follow mountain fronts of uplifted ranges that were formed by displacement on reverse faults that affected pre-Cenozoic basement rocks (Gangui, 1998; Riller and Oncken, 2003). The curvature of individual fault zones of the NE-striking system toward parallelism with faults of the orogen-parallel system indicates that the two fault systems are geometrically and kinematically linked. As a result, the curvilinear faults of both fault systems enclose compressive basins of rhombohedral shape in plan view, as the Atacama basin. This suggests that the morphology of the southern central Andes is largely a result of reverse faulting on the two fault systems (Riller and Oncken, 2003).

In this region, as part of the Central Volcanic Zone between 21° and 24°S, is developed the Altiplano-Puna Volcanic Complex in response to a late Miocene ignimbrite “flare up” in the Altiplano-Puna plateau (De Silva, 1989). This major volcano-tectonic province occupies an area over 70.000 km^2 and is the site of the largest concentration of voluminous late-Miocene to Pliocene ignimbrite eruptions on earth. This region has been continuously active since 23 Ma, ending a period of magmatic quiescence in the Oligocene to early Miocene. While andesite volcanism dominated from the late Tertiary until the late Miocene, since then the volcanism was dominated by voluminous ignimbrite eruptions, producing regionally extensive, crystal-rich, dacitic and large volume ignimbrites (Lindsay et al., 2001).

For a regional description of the different units over which Lascar volcano is placed, from the eastern border of the Salar de Atacama until the western border of the Puna, a temporal classification can be made, starting from volcano sedimentary units of Paleozoic age until the Pleistocene-Holocene volcanic deposits.

Some of the oldest rocks of this region can be identified as volcano sedimentary successions representing the product of a magmatic zone at the Pacific margin of Gondwana that can be traced from the Peruvian Andes until the Antarctic Peninsula (Breitkreuz and Zeil, 1994). In the north Chilean Precordillera and Western Cordillera, these units are grouped in the Peine Group (Bahlburg and Breitkreuz, 1991).

East of the Salar de Atacama a long chain of outcrops of volcano sedimentary units of the Peine Group is exposed (see figure 2.5), considering basic lavas intercalated with volcanogenic sandstones in the Peine formation which overlies unconformably the Cas formation, formed mainly by siliceous ash, lapilli tuffs and flows. Peine formation has been dated between 290 and 229 Ma (Gardeweg et al., 1998; Breitkreuz and Zeil, 1994). The Allana and Cuyuguas hills formed by sedimentary and volcanic rocks are lithologically similar to the Cas formation, and are intruded by different granites, aplites and andesitic dykes (Breitkreuz and Zeil, 1994; Gardeweg et al., 1994).

In the whole area of study, it is possible to distinguish a Cenozoic cover mainly formed by volcano sedimentary rocks of different ages. Paleogene deposits can be found to the south and west of Lascar volcano, identified as the Quepe strata, composed of sandstones, volcano-clastic conglomerates and lutites. Much more extended in the surface of the area around Lascar are the rocks formed by the Miocene to Pliocene magmatism of the Altiplano-Puna volcanic complex (De Silva, 1989).

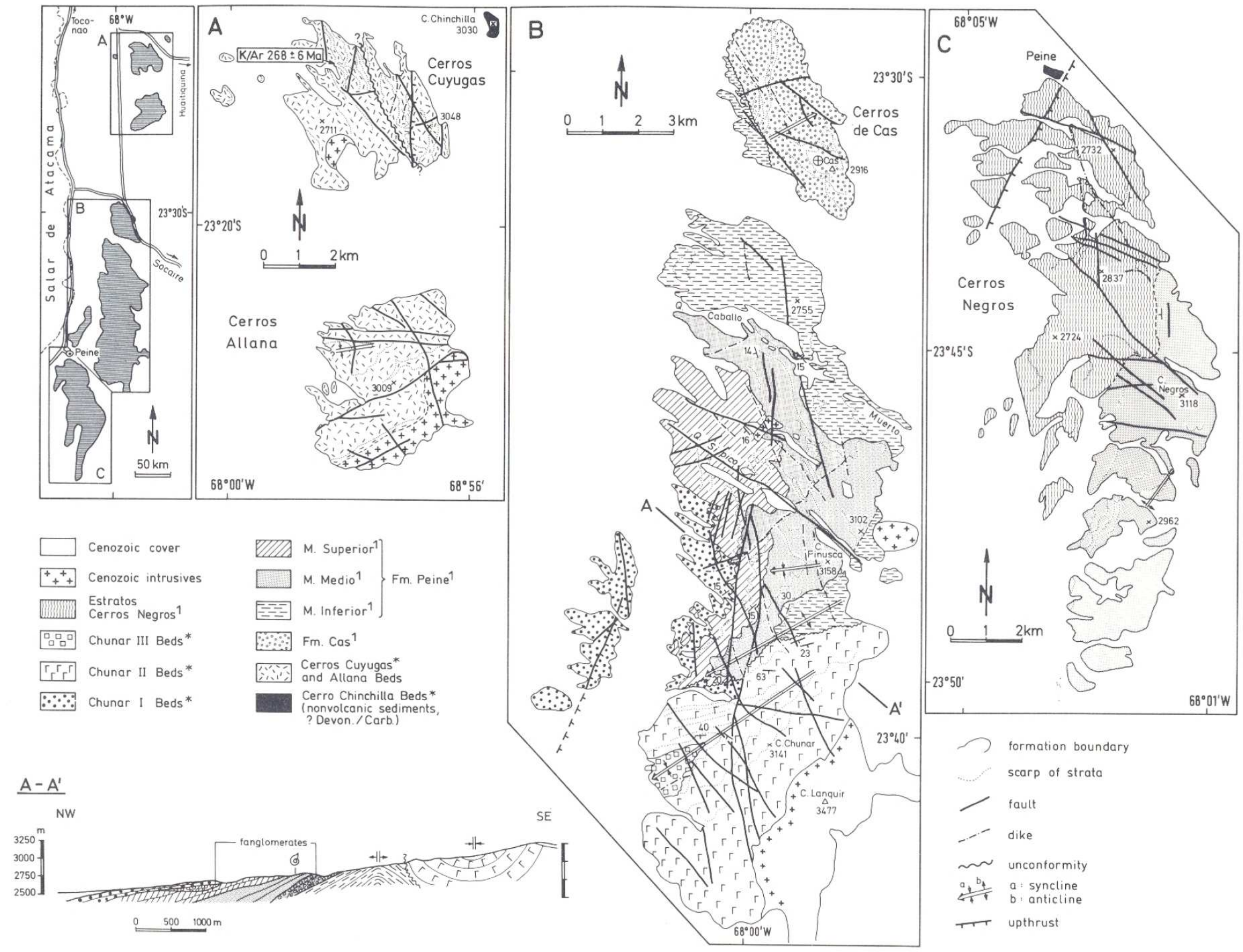

Figure 2.5: Geological map of the area east of Salar de Atacama, from Breitkreuz and Zeil (1994). A, B and C represent 3 zones to the E of the Salar de Atacama, as shown in the leftmost image.

The ignimbrites asociated with the evolution of the Pliocene volcanism form a slightly sloping plateau which covers most of the pre-Cenozoic rocks. Toconao and Atana ignimbrites appear to have been generated from La Pacana caldera, one of the largest resurgent calderas in South America (60 x 35 km^2), and part of the Altiplano Puna Volcanic Complex. Toconao is a smaller volume, crystal poor and rhyolitic ignimbrite. With an age between 4.0-5.8 Ma (Gardeweg and Ramírez, 1987; Lindsay et al., 2001), it is considered as a pre caldera ignimbrite. The Atana ignimbrite is a large volume, homogeneous, crystal rich and dacitic ignimbrite, with an age of 4 Ma and it is associated with the formation (collapse) of the La Pacana caldera (Gardeweg and Ramírez, 1987), with a volume estimation of 2500 km^3 (Lindsay et al., 2001). Following caldera collapse and formation of the resurgent Atana block, several crystal-rich dacitic-rhyolitic domes formed along the margin of the resurgent block. K-Ar ages show that this post-caldera volcanism continued from 4 to 2 Ma, indicating that the La Pacana magmatic system was active for at least 2 Ma after the main eruption.

Other younger ignimbrites present in the zone are:
- Tucucaro and Patao ignimbrites, rhyolitic poor in crystals, with ages between 2.9 and 3.2 Ma (Gardeweg and Ramírez, 1987).
- Pampa Chamaca ignimbrite, rhyolitic of age between 2.4 and 2.5 Ma (Gardeweg and Ramírez, 1987; Lindsay et al., 2001).

2.2 Evolution of Lascar volcano

Lascar volcano developed in the western margin of the Altiplano about 30 km east of the Salar de Atacama on Pre-Cenozoic basement rocks. It is located at 23°22′S, 67°41′W and has an altitude of 5592m above sea level. It corresponds to a volcanic massif composed of two stratovolcanoes with ejection centers separated by 1.6 km. Its craters reach 900 m diameter each. An aerial view of this volcano is presented in figure 2.6.

Lascar is bounded by two major volcanic centers. To the SW, the Tumisa volcano consists of a dome complex of highly porphyritic dacite, surrounded by a fan of pyroclastic flow deposits (Matthews et al., 1997). The Tumisa complex has K-Ar dates ranging between 2.5 and 0.4 Ma. Aguas Calientes volcano, east of Lascar consists of hornblende andesite and dacite lavas. All Lascar pyroclastic deposits are younger than Aguas Calientes.

The edifice of Lascar, from the first eruptive stage, is constituted essentially by lavas and andesitic pyroclasts (60.44% SiO_2). A second eruptive cycle developed three craters in row throw which were ejected pyroclastic fluxes and andesitic-dacitic to dacitic lavas (70.87% SiO_2). The most recent lava flux corresponds to an andesitic-basaltic (58.0% SiO_2) reaching 5.5 km through the N-NW slope, maybe 500 or 600 years ago.

Its most recent activity has been characterized by explosive eruptions such as the one on April 1993, with vulcanian explosions, strombolian activity and plinian eruptions, with a column of tephra and gases reaching 12000 m.

Its activity started before the last glacial maximum but less than 50 ka years ago. According to Matthews et al. (1997) the volcanic history can be separated into four evolutionary stages, which created an edifice aligned in an E-W direction. Stage I built an edifice on the eastern side and erupted pyroxene-andesite lavas, producing at the end of this stage two andesitic pyroclastic flow deposits (Saltar and Chaile). In stage II the activity shifted to the western side. Evidences indicate that this stage produced a substancial dome complex which has been largely destroyed. The stage II Soncor eruption (radiocarbon age of 26.45 ka), the largest explosive eruption of the volcano, produced 10-15 km^3 of mixed andesitic to dacitic pyroclastic flow deposits and a large Plinian fallout deposit. In stage III a stratocone was constructed of silicic andesitic and dacitic lavas and pyroclasts, built on top of the site of the Soncor eruption. This stage finished in a major andesitic explosive eruption, which generated scoria flow deposits known as the Tumbres deposits (9.2 ka). Finally, stage IV activity shifted eastwards again to the currently active part of the volcano. The most significant eruption from stage IV was the Tumbres-Talabre Lava in the N-W (7.1 ka). This flow was truncated by the formation of the first of three deep collapse craters that document a progressive westward migration of the center of activity.

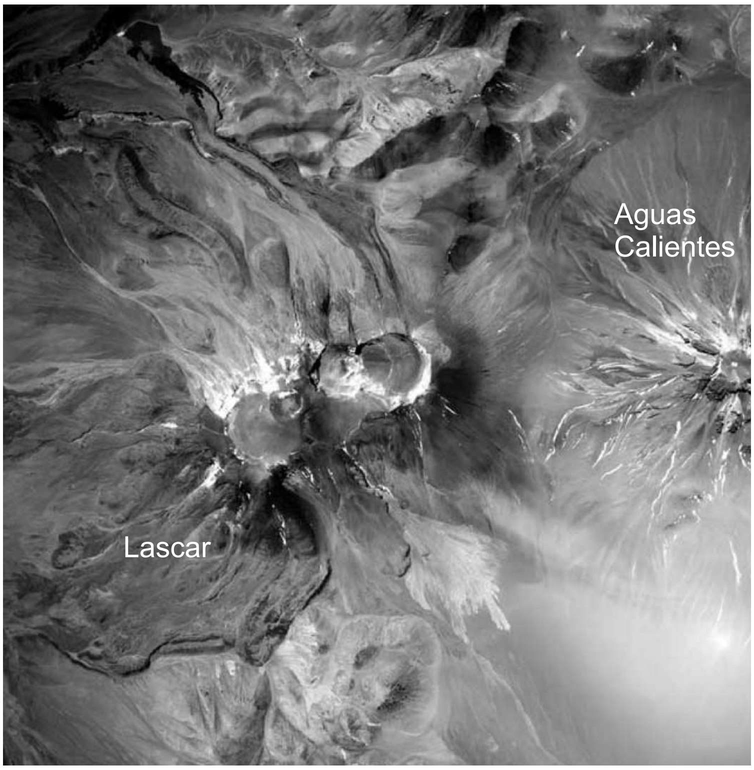

Figure 2.6: Aerial photograph of the active area of Lascar volcano acquired in 1998 (extracted and edited from Pavez et al. (2006)).

The volcanic rocks of Lascar are dominantly pyroxene andesite and dacite, although hornblende-andesite and dacite have been identified from the Piedras Grandes and Soncor deposits. The magmas commonly show evidence for mixing between mafic and evolved components, indicating that a fractionating magmatic system is periodically replenished with basaltic andesite magma. Samples of andesite lava (57.2-59.3 wt.% SiO_2) from the recent explosive activity (1986-1990) show little or no evidence for mixing with more evolved components, but the products of the April 1993 and subsequent dome contain conspicuous compositionally banded ejecta and lava (57.2-60.8 wt.% SiO_2). The presence of anhydrite phenocrysts in many samples, including the 1993 ejecta, indicate high volatile pressure and the presence of a coexisting magmatic gas with high sulphur content (Matthews et al., 1997).

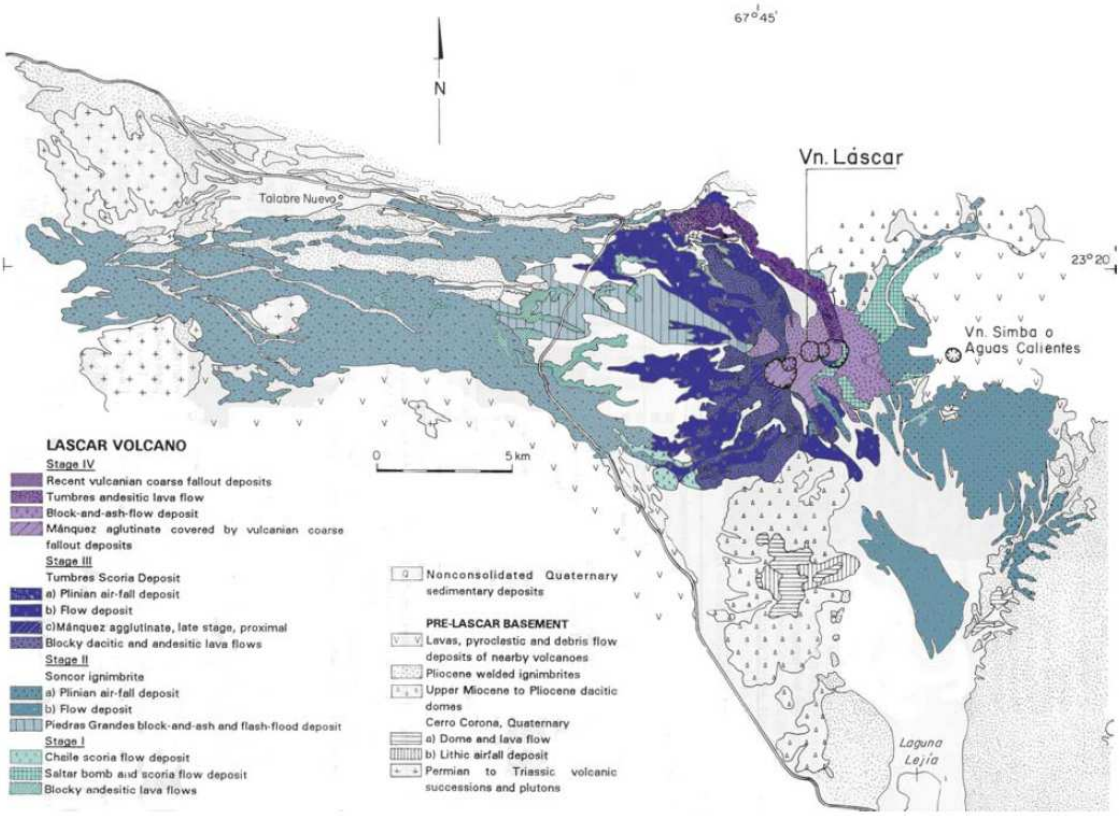

Figure 2.7: Geology around Lascar volcano (Gardeweg et al., 1998) showing the different evolutionary stages. Scale 1:50.000.

Historically, its behavior has been recorded since 1848 and it has been characterized by continuous fumarolic emissions and occasional vulcanian explosions. The activity of the volcano itself, since 1984, can be described in terms of four eruptive cycles, according to the work and measurements of different authors in the zone, summarized by Matthews et al. (1997) as four cycles, involving growth and subsidence of the lava dome and crater system, completed by an explosive event.

Cycle 1: Beginning with a reactivation of Lascar in 1984, presenting strong degassing. A violent vulcanian eruption occurred on 14-16 September 1986, ejecting a column of ash and water vapor to an altitude of 10 km above the crater. There is not direct observation of lava dome subsidence prior to the eruption, but there was a major decrease in high level thermal activity, based on remote sensing observations (Oppenheimer et al., 1993) from 1984-1986.

Cycle 2: Between February and April 1989 a lava dome extruded, accompanied by strong fumarolic emissions, subterranean noise and crater glow. By October 1989 the dome started to subside, and developed concentric annular fractures, due to subsidence in the center. Strong steam eruptions were observed on 17 and 21 December 1989, producing dense, white clouds up to 2 km above the crater. Three intense vulcanian explosions occurred on 20 February 1990 over a period of 5-10 minutes, forming eruption columns 8-14 km above the crater. Bombs of dense vesicular andesite, up to 1.5 m in diameter, are interpreted to be fragments of the dome, and were found up to 4 km from the vent.

Cycle 3: By March 1990 the dome had almost completely disappeared. Between February and March 1992 a new lava dome was observed in the active crater, related with a peak in 1.6 μm thermal radiance detected from satellites (Oppenheimer et al., 1993). Several minor explosive eruptions occurred on 15 and 21 May and between June and September 1992. The initiation of dome subsidence was first directly observed in November 1992, disappearing almost completely by March 1993. There was pronounced seismicity in January-March 1993, consisting of abundant long period earthquakes, which are conventionally interpreted to indicate degassing or magma movement. On 19-20 April a substantial explosive eruption occurred. This eruption was preceded by two intense vulcanian eruptions on 18 April 1993, maintaining an eruption column during 19-20 April between 5 and 25 km above the volcano, and generating collapse pyroclastic flows to the northwest, northeast and southeast of the volcano.Tephra fell over a large area of Paraguay, Uruguay, Brazil and Argentina. Bombs up to 1.5 m diameter were found in impact craters up to 5 km from the vent. An estimated 0.1 km^3 of magma was erupted, accompanied by 400 kTon SO_2.

Cycle 4: On 26 April 1993 a new dome was observed in the crater, with a flat surface and an estimated diameter of 380 m. Observations made on 19 May indicated that the dome had begun to subside. An aerial photograph made by Fuerza Aerea de Chile on 11 June 1993 showed that further collapse had occurred. A small vulcanian explosive eruption occurred in August. By 12 December the shortwave infrared signal had fallen to zero, showing that dome activity and degassing were very low. On 17 December 1993 a vulcanian explosion produced a column 8-10 km high. Bombs of around 1 m diameter were ejected up to 2 km from the crater.

During April and May 1994, one year after the previously detailed eruption of 1993, three short-period, three component seismometers were placed on the flanks of the volcano, together with a broadband seismometer located on the NW flank of Lascar during the PISCO ’94 experiment (Proyecto de Investigación Sismológica de la Cordillera Occidental 94). The results of this study, detailed in Hellweg (1999a,b, 2000), show the presence of two different kinds of tremors, rapid-fire and harmonic, and both seem to be generated by movement of fluids in the volcano, most probably water, steam or gas.

A SAR interferometry study developed during the last decade in Lascar, detailed in Pavez et al. (2006), shows the ground deformation in the volcano based on time series data from European and Japanese satellites acquired between 1993 and 2000. This study indicates that no persistent large scale deformation could be detected for the sequence of vulcanian eruptions after the April 1993 eruption. Post eruptive crater subsidence associated with degassing at subsurface levels beneath the central crater was evidenced and quantified.

Chapter 3

Theoretical background of Magnetotellurics

Magnetotellurics is a geophysical method which uses electromagnetic induction to investigate the electrical conductivity distribution in the Earth. MT is a passive method which uses as signal source the variations of the natural external electromagnetic field originating from diverse extraterrestrial processes and encompassing a broad spectrum of frequencies. The field variations can be generally classified in: solar daily variations (Sq-variations), magnetic storms, pulsations and spherics. The spectra of these variations cover periods ranging from 10^{-3} to 10^{5} s and are generated by interaction between the solar wind and the magnetosphere and ionosphere of our planet. This method can be also active when the source is a controlled artificial signal, receiving the name of CSMT (Controlled Source MT). The relationship between the period of the electromagnetic waves and the penetration depth is given by the *skin effect*, showing that with a broad frequency band, depths up to several hundreds of kilometers can be imaged.

The first publications about this theory, based on Maxwell's equations, where made by Tikhonov (1950) and Cagniard (1953), who designed the magnetotelluric sounding as a method for studying the vertical variations in the electrical conductivity distribution, in 1-D. It was not until the 1960's when different experiments (e.g. Tikhonov and Berdichevsky, 1966) showed that horizontal geoelectric inhomogeneities can be the cause of great distortions in the results of MT sounding, and that magnetotellurics needed a theory considering the electromagnetic field within the horizontally inhomogeneous Earth.

The time varying external magnetic field in the Ionosphere induces according to Faraday's law in the Earth's interior an electric field which in turn induces a secondary, internal magnetic field (Ampere's law). The induction process in a homogeneous isotropic medium is governed by the Maxwell equations, which can be written as follows.

$$\begin{aligned} \nabla \times \vec{E} &= -\frac{\partial \vec{B}}{\partial t} && \textit{Faraday's law of induction } (1^{st} \textit{ Maxwell's law}) && (3.1)\\ \nabla \times \vec{H} &= \vec{j_f} + \frac{\partial \vec{D}}{\partial t} && \textit{Ampere's law } (2^{nd} \textit{ Maxwell's law}) && (3.2)\\ \nabla \cdot \vec{B} &= 0 && \textit{Gauss' law for magnetism} && (3.3)\\ \nabla \cdot \vec{D} &= q_f && \textit{Gauss' law} && (3.4) \end{aligned}$$

Where $\vec{E}$ is the electric field (in V/m), $\vec{B}$ is the magnetic field (in T), $\vec{H}$ is the magnetizing field (in A/m), $\vec{j_f}$ the current density owing to free charges (in A/m^2), $\vec{D}$ the electric displacement field (in C/m^2) and q_f the electric charge density owing to free charges.
Assuming that time-varying displacements currents (arising from polarization effects) are negligible compared with time-varying conduction currents, Ampere's law reduces to

$$\nabla \times \vec{H} = \vec{j_f} \tag{3.5}$$

For a linear isotropic medium, the material equations have been shown to hold:

$$\vec{B} = \mu \vec{H} \tag{3.6}$$
$$\vec{D} = \epsilon \vec{E} \tag{3.7}$$

For MT studies, variations in electrical permittivities (ϵ) and magnetic permeabilities (μ) of rocks are negligible compared with variations in bulk rock conductivities, and free space values ($\epsilon_0 = 8.85 \times 10^{-12} Fm^{-1}$ and $\mu_0 = 1.2566 \times 10^{-6} Hm^{-1}$) are assumed.
Considering equations 3.5, 3.6 and 3.7, and also that $\vec{J} = \sigma \vec{E}$ (Ohm's law), with σ the conductivity (in S/m), the Maxwell equations can be written in a compact form.

$$\nabla \times \vec{E} = -\frac{\partial \vec{B}}{\partial t} \tag{3.8}$$
$$\nabla \times \vec{B} = \mu_0 \sigma \vec{E} \tag{3.9}$$
$$\nabla \cdot \vec{B} = 0 \tag{3.10}$$
$$\nabla \cdot \vec{E} = \frac{q_f}{\epsilon} \tag{3.11}$$

Given the following identity,

$$\nabla \times \nabla \times \vec{\Psi} = \nabla(\nabla \cdot \vec{\Psi}) - \nabla^2 \vec{\Psi}$$

and considering that $\nabla \cdot \vec{B} = 0$ (Gauss' law for magnetism) and also the fact that no free charges can be accumulated in a medium of uniform conductivity ($\Delta\sigma = 0$), i.e. $\nabla \cdot \vec{D} = 0$ and $\nabla \cdot \vec{E} = 0$, if the curl is applied to equations 3.8 and 3.9, the result will be the following:

$$\begin{aligned} \nabla \times \nabla \times \vec{E} &= \nabla(\underbrace{\nabla \cdot \vec{E}}_{0}) - \nabla^2 \vec{E} = \nabla \times (-\frac{\partial \vec{B}}{\partial t}) \\ &\Rightarrow \nabla^2 \vec{E} - \mu_0 \sigma \frac{\partial \vec{E}}{\partial t} = 0 \qquad (3.12) \\ \nabla \times \nabla \times \vec{B} &= \nabla(\underbrace{\nabla \cdot \vec{B}}_{0}) - \nabla^2 \vec{B} = \nabla \times (\mu\sigma\vec{E} \\ &\Rightarrow \nabla^2 \vec{B} - \mu_0 \sigma \frac{\partial \vec{B}}{\partial t} = 0 \qquad (3.13) \end{aligned}$$

An important approximation adopted is the assumption of a plane polarized wave vertically incident on the conductive Earth, which means that the vertical variations of the electromagnetic field are much more important than the horizontal ones. This assumption is based in the large distance between the source of these electromagnetic waves, which is in the Ionosphere, and the observation point, which is in the Earth's surface, more than 100 km away.

3.1 1-D case

Starting now with the simplest case of an homogeneous half-space (extending in z-direction), and considering the fields with harmonic temporal variation e^{iwt}, equation 3.12 can be solved with a solution of the form:

$$\vec{E} = E_1 e^{i\omega t - qz} + E_2 e^{i\omega t + qz} \qquad (3.14)$$

Assuming that the Earth does not generate electromagnetic energy, only dissipates or absorbs it, $\vec{E}$ should diminish as z increases (z→Earth's radius), implying that $E_2 = 0$.
Taking the second derivative of the previous equation,

$$\frac{\partial^2 \vec{E}}{\partial z^2} = q^2 E_1 e^{i\omega t - qz} = q^2 \vec{E} \qquad (3.15)$$

And considering that in an half-space model $\frac{\partial \vec{E}}{\partial x} = 0$ and $\frac{\partial \vec{E}}{\partial y} = 0$, we can evaluate our solution in equation 3.12, obtaining:

$$\begin{aligned} \nabla^2 \vec{E} = \frac{\partial^2 \vec{E}}{\partial z^2} \quad &\Rightarrow \quad i\omega\mu_0\sigma\vec{E} = q^2\vec{E} \\ &\Rightarrow \quad q = \sqrt{i\omega\mu_0\sigma} = \sqrt{\omega\mu_0\sigma/2} + i\sqrt{\omega\mu_0\sigma/2} \end{aligned} \tag{3.16}$$

and the inverse of the real part of q:

$$p = 1/Re(q) = \sqrt{2/\mu_0\sigma\omega} \tag{3.17}$$

is known as the electromagnetic *skin depth*. This penetration factor depends on the angular frequency and conductivity of the medium in which the wave is propagating. As larger is the frequency, the stronger is the attenuation, and the penetration depth becomes smaller. The value $C = 1/q = p/2 - ip/2$ is referred to as the Schmucker-Weidelt transfer function. The transfer function C establishes a linear relationship between the physical properties that are measured in the field. Considering $E_x = E_{1x}e^{i\omega t - qz}$:

$$\frac{\partial E_x}{\partial z} = -qE_x \tag{3.18}$$

Comparing equations 3.18 and 3.8,

$$\frac{\partial E_x}{\partial z} = -\frac{\partial B_y}{\partial t} = -i\omega B_y = -qE_x \Rightarrow C = 1/q = \frac{E_x}{i\omega B_y} = -\frac{E_y}{i\omega B_x} \tag{3.19}$$

Therefore, C can be calculated from measured E_x and B_y fields, or equivalently E_y and B_x fields, and if C is known, the resistivity of the homogeneous half-space can be calculated combining equations 3.16 and 3.19, obtaining:

$$\rho = 1/\sigma = \frac{1}{|q|^2}\mu_0\omega = |C|^2\,\mu_0\omega[VmA^{-1}] \tag{3.20}$$

Now, extending the previous result for a N-layered half-space, within every layer with conductivity σ_n we can find a solution of the form given in equation 3.14:

$$\begin{aligned} E_{xn}(q_n, \omega) &= E_{1n}e^{i\omega t - q_n z} + E_{2n}e^{i\omega t + q_n z} \\ &= a_n(q_n, \omega)e^{-q_n z} + b_n(q_n, \omega)e^{+q_n z} \end{aligned} \tag{3.21}$$

In the same way, the magnetic field within the nth layer is given by:

$$B_{yn}(q_n, \omega) = a_n(q_n, \omega)e^{-q_n z} + b_n(q_n, \omega)e^{+q_n z} \tag{3.22}$$

Assuming that we could measure E_{xn} and B_{yn}, the transfer function C according to eq. 3.19 will be given by:

$$C_n(z) = \frac{E_{xn}(z)}{i\omega B_{yn}(z)} \tag{3.23}$$

Substituting equations 3.21 and 3.22 into equation 3.23, it is possible to derive expressions for the transfer functions at the top and bottom of the nth layer, $C_n z_{n-1}$ and $C_n(z_n)$ respectively. Based on the continuity of the field components at the transition from the nth to the (n-1)th layer,

$$C_n(z_n) = \lim_{z \to z_n - 0} C_n(z) = \lim_{z \to z_n + 0} C_{n+1}(z) = C_{n+1}(z_n) \tag{3.24}$$

Wait obtained, in 1954, a recursion formula to calculate the transfer function at the top of the nth layer, if the transfer function at the top of the (n+1)th layer is known:

$$C_n(z_{n-1}) = \frac{1}{q_n} \frac{q_n C_{n+1}(z_n) + tanh(q_n l_n)}{1 + q_n C_{n+1}(z_n) tanh(q_n l_n)} \tag{3.25}$$

Where $l_n = z_n - z_{n-1}$. In this n-layer scenario, it is possible to define the concept of *apparent resistivity* as the average resistivity of an equivalent homogeneous half-space as follows:

$$\rho_a(\omega) = |C(\omega)|^2 \mu_0 \omega$$

And the correspondent *impedance phase*,

$$\phi_{1-D} = tan^{-1}(E_x/B_y)$$

Weidelt, in 1972, linked these two parameters via the Kramers-Kronig relationship, which states that $\rho_a(T)$ can be predicted from $\phi(T)$ except for a scaling factor, ρ_0. The impossibility to predict the absolute level of the $\rho_a(T)$ curve from the impedance phase in some 2D and 3D conductivity distributions, whereas the shape can be predicted, reflects the *static shift* phenomenon.

3.2 2D case, TE and TM modes

The 1-D situation in magnetotellurics is clearly a very simplified case, and in practice one should be able to resolve this problem in at least 2 dimensions, assuming continuity in one direction. This could be the case of a dyke or a fault with an approximately constant conductivity along its strike.

For a body with infinite along-strike direction and with a constant conductivity along its strike, let us define the x-direction as the strike of this body, and the 2D conductivity to be $\sigma(y, z)$, as well as its reciprocal, the 2D resistivity as $\rho(y, z)$. The 2D profile direction, y, is also horizontal, and z is vertical and increases downwards. Since the EM-fields are treated as plane waves, which means that the interaction between electric and magnetic fields are always orthogonal with each other and therefore the horizontal component of the magnetic field tangential to the conductivity strike does not depend on the magnetic field component perpendicular to it, the Maxwell equations can be decoupled into two polarization modes:

- The TE-mode (sometimes called E-parallel, B-perpendicular or E-polarization), refers to the tangential electric field with respect to the strike, in which the electric currents flow perpendicular to the 2D profile (along strike).
- The TM-mode (sometimes called E-perpendicular, B-parallel or B-polarization) refers to the tangential magnetic field with respect to the strike, in which the currents flow along the 2D profile (perpendicular to strike).

Thus, this decoupling can be expressed as follows,

TE-mode

$$\begin{aligned} \frac{\partial B_z}{\partial y} - \frac{\partial B_y}{\partial z} &= \mu_0 \sigma E_x \\ \frac{\partial E_x}{\partial z} &= -i\omega B_y \\ \frac{\partial E_x}{\partial y} &= i\omega B_z \end{aligned} \tag{3.26}$$

TM-mode

$$\begin{aligned} \frac{\partial E_z}{\partial y} - \frac{\partial E_y}{\partial z} &= i\omega B_x \\ \frac{\partial B_x}{\partial z} &= -\mu_0 \sigma E_y \\ \frac{\partial B_x}{\partial y} &= \mu_0 \sigma E_z \end{aligned} \tag{3.27}$$

3.3 Impedance Tensor

Considering the fluctuations in the components of the natural electric and magnetic fields, measured in orthogonal directions at the surface of the Earth, the orthogonal components of the horizontal electric and magnetic fields are related via the electrical impedance Z [mV/T], which is the ratio between the electrical and magnetic field components.

In an homogeneous media, the ratio of the orthogonal components is given by (from equation 3.19):

$$Z = \frac{i\omega}{q} \tag{3.28}$$

In a general 3D Earth, the impedance is expressed in matrix form:

$$\begin{bmatrix} E_x \\ E_y \end{bmatrix} = \underbrace{\begin{bmatrix} Z_{xx} & Z_{xy} \\ Z_{yx} & Z_{yy} \end{bmatrix}}_{\underline{Z}} \begin{bmatrix} B_x \\ B_y \end{bmatrix} \tag{3.29}$$

Where each element of the impedance tensor is defined as $Z_{ij} = E_i/B_j$, with $i, j = x$ or y

In the 1-D case with conductivity varying only with depth, due to the symmetry of the problem it can be verified that $Z_{xy} = -Z_{yx}$ and that $Z_{xx} = Z_{yy} = 0$.

In the 2D case, with the x or y direction aligned along the electromagnetic strike, the measured horizontal electric and magnetic fields at the Earth-air interface in the frequency domain are related by:

$$\begin{bmatrix} E_x \\ E_y \end{bmatrix} = \begin{bmatrix} 0 & Z_{xy} \\ Z_{yx} & 0 \end{bmatrix} \begin{bmatrix} B_x \\ B_y \end{bmatrix} \tag{3.30}$$

Where the off-diagonal impedances Z_{xy} and Z_{yx} correspond to the TE and TM modes.

The impedance tensor can be rotated in any other coordinate system by an angle θ, with the rotation matrix R

$$\underline{Z}_m = R\underline{Z}R^T, \text{ where } R = \begin{bmatrix} cos\theta & sin\theta \\ -sin\theta & cos\theta \end{bmatrix}$$

with positive θ describing a clockwise rotation from the coordinate system of $\underline{Z}_m$.

In the general case, the apparent resistivity related to each component of the impedance tensor is defined by:

$$\rho_{a,ij} = \frac{\mu_0}{\omega} |Z_{ij}(\omega)|^2 \tag{3.31}$$

while the phase of the impedance element, describing the phase shift between the electric and magnetic field components:

$$Z_{ij} = |\frac{E_{ij}}{B_{ij}}|e^{i\phi} \Rightarrow \phi_{ij} = \varphi_{E_i} - \varphi_{B_j} = tan^{-1}\left(\frac{Im\left\{Z_{ij}(\omega)\right\}}{Re\left\{Z_{ij}\right\}}\right) \tag{3.32}$$

where $i, j = x, y$ and φ_{E_i} and φ_{B_j} are the phase of the electric and magnetic field components respectively.

In an homogeneous space, the impedance phase is:

$$Z = \frac{i\omega}{q} = \sqrt{\frac{\omega}{\mu_0\sigma}}\sqrt{i} \Rightarrow \phi = \pi/4 \tag{3.33}$$

which means that the electric field precedes the magnetic field by 45°, given by the diffusive process of the EM plane waves propagation.

In a 1-D layered earth the phase increases over 45° when the EM-response penetrates into a higher conductivity media. By analogy, the phase drops below 45° for the electromagnetic response penetrating into a less conductive media, meaning that by the diffusive process, the phase shift between the orthogonal electric and magnetic field components attenuates when the fields penetrates into a less conductive media.

In the 1D/2D case the phases lie in the I or III quadrant ([0, π/2] or [π, 3π/2]), which means that the real and imaginary parts of Zxy (or Zyx) have equal sign. This is due to the principle of causality of the interaction between electric and magnetic fields induced in the earth, i.e., any secondary field induced due to a conductivity contrast should necessarily postdate the primary incident field. By convention, the element Zxy is defined as positive and therefore Zyx is negative, implying an impedance phase in the I and III quadrant, respectively.

One of the primary purposes of MT impedance tensor analysis is to determine what the intrinsic dimensionality and directionality of the tensor are, and how those change with decreasing frequency (increasing depth). Several parameters will be introduced in order to analyze properly the measured data and determine correctly the dimensionality of the problem that we have to solve. This analysis, carried out in the next chapter, will define if a 2D assumption is sufficient to explain our data, or if the development of 3D models is necessary.

Chapter 4

Data processing and analysis

In order to improve the quality, visualize and analyze the magnetotelluric data collected during the field campaigns, before use it in inversions or models, a first data processing was performed, followed by a dimensionality analysis. Both procedures will be clarified in this chapter.

4.1 Data processing

The digital time series collected in the field campaign can simultaneously contain information about many periods and, therefore, about many penetration depths. The first step in data processing consists in a preprocessing of the time series, in order to remove spikes and errors in the data. The following step is to change to the frequency domain, for this purpose a spectral analysis is carried out considering the following procedure:

- Classical Spectral Estimations, applying the Fast Fourier transformation to the time series.
- Window tapering, in order to reduce spectral leakage and hence the bias.
- Cascade decimation, where each decimation step involves anti-aliasing low-pass filtering of the time series with a recursive filter and then decimation.
- Spectral resolution, choosing the length of the data segment.

After the spectral analysis, transfer functions need to be calculated, by solving the linear expansion of equation 3.29:

$$E_x = Z_{xx}(\omega)B_x(\omega) + Z_{xy}(\omega)B_y(\omega) \tag{4.1}$$

$$E_y = Z_{yx}(\omega)B_x(\omega) + Z_{yy}(\omega)B_y(\omega) \tag{4.2}$$

Because the plain wave source field assumption is only an approximation, a statistical solution for the MT impedance is required, so the remainder function $\delta E(\omega)$ is minimized, assuming that errors in the measurements of the magnetic field are negligible compared to the errors in the electric field, and considering the N independent segments in which the time series have been divided in the Fast Fourier Transformation, equations 4.1 and 4.2 can be re-written as follows:

$$E_{xk} = Z_{xx}B_{xk} + Z_{xy}B_{yk} + \delta E_{xk} \tag{4.3}$$

$$E_{yk} = Z_{yx}B_{xk} + Z_{yy}B_{yk} + \delta E_{yk} \tag{4.4}$$

for $k = 1 \ldots N$. Then the standard least squares approach to solve this problem (e.g. Sims et al. (1971)) leads to:

$$\underline{Z} = (\vec{E}\vec{B}^*)(\vec{B}\vec{B}^*)^{-1} \tag{4.5}$$

$$\tag{4.6}$$

where $*$ denotes the complex conjugate transpose, and

$$(\vec{E}\vec{B}^*) = \begin{pmatrix} \langle E_x {B_x}^* \rangle & \langle E_x {B_y}^* \rangle \\ \langle E_y {B_x}^* \rangle & \langle E_y {B_y}^* \rangle \end{pmatrix}$$

with

$$\langle XY^* \rangle = \frac{1}{N}\sum_{k=1}^{N} X_k Y_k^*$$

In this work, a program developed by Egbert and Booker (1986) has been used for the estimation of the transfer function, which incorporates a robust scheme that iteratively down-weights data that do not fit the model of Gaussian distributed variables (the regression M-estimator, adopted from Huber (1981)). In this approach, we seek estimates of the transfer function $\underline{Z}$ which minimizes an expression of the form:

$$\sum_k \rho\left(\frac{\vec{E}_k - \vec{B}_k \underline{Z}}{\sigma}\right) \tag{4.7}$$

where σ is a scale parameter used for normalizing the residuals, $r_0 = 1.5$, and $\rho(r)$ is a function of the form:

$$\rho(r) = \begin{cases} r^2/2 & |r| < r_0 \\ r_0|r| - {r_0}^2/2 & |r| \geq r_0 \end{cases}$$

instead of $\rho(r) = r^2/2$, which corresponds to a Weighted Least Squares approach.

If the errors in the magnetic field measurements are not negligible (against the initial hypothesis), the autopowers may amplify the noise in the measured fields, severely biasing the impedance estimates (Gamble et al., 1979). The use of a remote magnetometer was proposed to obtain reference fields, as the uncontaminated (natural) part of the induced field can be expected to be coherent over a spatial scale of many kilometers and noise is generally random and incoherent, the noise of the remote station should be uncorrelated with any of the four fields at the MT station. Correlated noise that is present in both, local and remote sites cannot be removed by this method. The use of magnetic field as remote reference is preferred over the electric field because horizontal magnetic fields exhibit greater homogeneity than electric fields in the vicinity of lateral heterogeneities, are less susceptible to being polarized and are generally less contaminated by noise than electric fields. The distance between local and remote site that is necessary to realize the assumption of uncorrelated noise depends on the noise source, intended frequency range and conductivity of the sounding medium. Normally, the instruments are placed several kilometers apart, ensuring the simultaneous data recording with the use of GPS clocks.

With remote reference processing, only cross spectra of horizontal magnetic field components of local and remote sites appear in the solution of $\underline{Z}$, obtaining an unbiased estimation.

Also the elements of the induction vectors (explained in detail in section 4.2.1 of this chapter) can be estimated similarly to $\underline{Z}$, and unbiased estimations can be obtained analogously with the horizontal magnetic field of a remote site.

With these estimations of the impedance tensor is possible to obtain the apparent resistivity and phase curves, according to the definitions given in equations 3.31 and 3.32. A comparison between the apparent resistivities and phases for the Z_{xy} and Z_{yx} components of the impedance tensor, obtained using single station processing and remote reference processing for one of the AMT stations measured close to Lascar volcano is shown in figure 4.1.

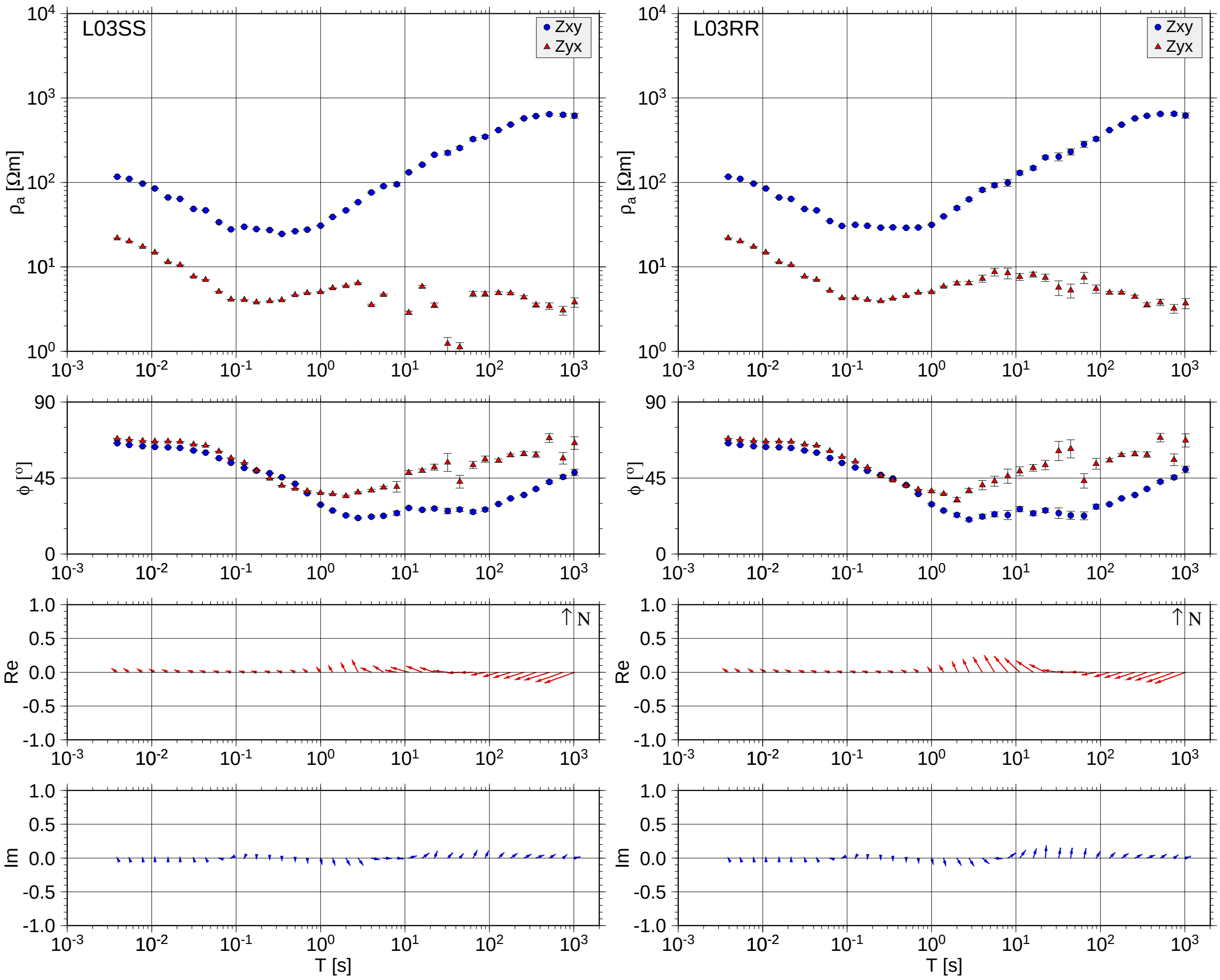

Figure 4.1: Apparent resistivity and phase curves, for the AMT station L03. In this case, the phase curves for both polarization modes are plotted in the first quadrant. Curves obtained with single site processing (left) and remote reference processing (right) are shown for comparison.

4.2 Dimensionality and distortion analysis

The MT transfer functions can be affected by DC-currents, in MT referred to as galvanic distortion, produced by local conductive bodies, small 3D structures which can impede the regional exploration of the underground. In this sense, they are a cause of distortion for the regional fields and therefore the goal is to remove this effect and recover the regional information.

The separation of local and regional effects is a critical issue in magnetotellurics. One way of approaching this problem is by the use of distortion matrices, which are used to represent the distortion of electric fields by near-surface inhomogeneities. Using distortion matrices, the distorted electric field is written as a function of the values the electric field would have had if the inhomogeneities were not present. Distortion matrices are useful when they can be determined well enough that their effect on data can be removed, and the data can be interpreted using a simpler model, such as a 2D model. The determination of a strike angle for the corresponding 2D case using distortion matrix analysis was developed for the measured AMT and LMT data.

For some of the apparent resistivity curves of the measured data, the transfer functions of some sites are affected by static shift, caused by small scale conductivity contrasts. This shift is called “static” because the conservation of current at conductivity discontinuities is not a time dependent process, and therefore, this phenomenon does not affect the phase of the transfer function. The phase tensor analysis is another way of approach to this problem, and allows to work with our measured data without the influence of these small scale conductivity contrasts.

The first parameter in study will be the *induction vectors*, which are vector representations of the complex ratios of vertical to horizontal magnetic field components. Since vertical magnetic fields are generated by lateral conductivity gradients, induction vectors can be used to infer the presence or absence of lateral variations in conductivity.

4.2.1 Induction vectors

The first parameter in study for this dimensionality analysis will be the geomagnetic transfer functions. Comparing them in different period ranges one can have an idea of the different conductivity gradients that are playing a role in the studied zone, and how good is the agreement between the possible conductivity distribution and the supposition of a 2D or a 3D situation.

The vertical component of the magnetic field, as well as both horizontal components were measured at every site, a good way to display these data is using induction vectors, which are a representation of the geomagnetic transfer functions calculated as follows:

$$B_z = (T_x \quad T_y) \begin{pmatrix} B_x \\ B_y \end{pmatrix}$$

where $\underline{T} = (T_x \quad T_y)$ is often termed “tipper”, because the secondary field of a lateral conductivity variation tilts the magnetic field out of its horizontal direction in a one-dimensional setting (Brasse et al., 2009).

Both T_x and T_y are complex numbers. By taking the real and imaginary part of these values, one can obtain the following.

$$\vec{P} = Re(T_x)\vec{e_x} + Re(T_y)\vec{e_y} \tag{4.8}$$

$$\vec{Q} = Im(T_x)\vec{e_x} + Im(T_y)\vec{e_y} \tag{4.9}$$

Where $\vec{e_x}$ and $\vec{e_y}$ are unitary vectors. $\vec{P}$ and $\vec{Q}$ are the induction vectors, and with them it is possible to identify conductive and resistive zones for the different frequencies, depending on the behavior of these vectors. According to the “Wiese convention”, used in this work, induction vectors point away from conductive zones.

These vectors were calculated for every measured period at each station. Some periods representing data in each decade for the LMT profile is shown in figure 4.2.

For periods between 10 s and 300 s, the induction vectors calculated along the LMT profile seem to be influenced by local conductivity heterogeneities, as no regional behavior can be noticed. One of the local effects present in the western border of the profile is the effect of the Salar de Atacama, as the induction vectors for the stations placed in the Salar (ATA and SAL) are showing a very small effect as they are surrounded by a highly conductive zone, and in its borders (PAC, PEI and PEN in the southern border) show very strong induction vectors pointing away from this basin for periods between 10 s and 100 s.

Different is the situation between 300 s and 3000 s. For this period range the induction vectors at every station behave in the same way, pointing to the W-SW with similar intensities as is shown in the image C of figure 4.2. This result, obtained during the processing of the data measured in 2007 was one of the motivations to extend the profile to the Argentinian Puna in the following field campaign conducted during January and February 2010. The new stations placed at the eastern border of this profile are not showing strong induction vectors as it is the case for all the other stations in the profile. This result, pointing to a strongly conductive anomaly under the Puna will be treated in depth in the following chapters. After 3000 seconds, the effect of this highly conductive zone at the eastern border of the profile decreases, and the induction vectors become weaker as shown in the image D of figure 4.2.

The same behavior can be seen in the induction vectors calculated for the AMT stations. Also between 300 s and 1000 s all the induction vectors are pointing in direction W-SW (F in figure 4.3), showing the same influence as the LMT stations, and indicating that the anomaly causing this behavior for this period range extends also to the north of the LMT profile. For the shortest periods the influence of the topography can be noticed especially in the stations closer to the volcanic edifice (L07 and L08 in image A and B in figure 4.3).

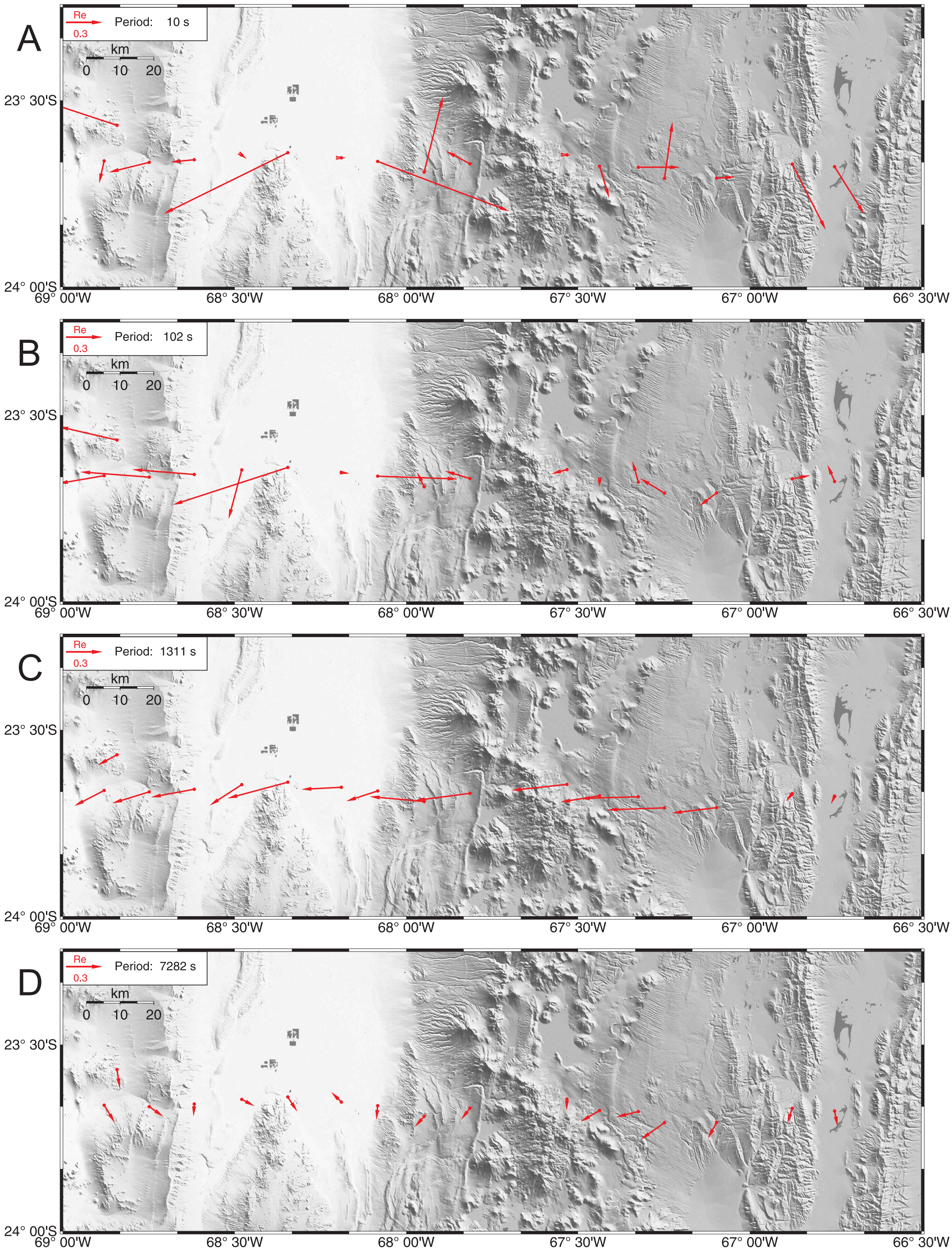

Figure 4.2: Real induction vectors of LMT stations for periods of 10 s, 102 s, 1311 s and 7282 s.

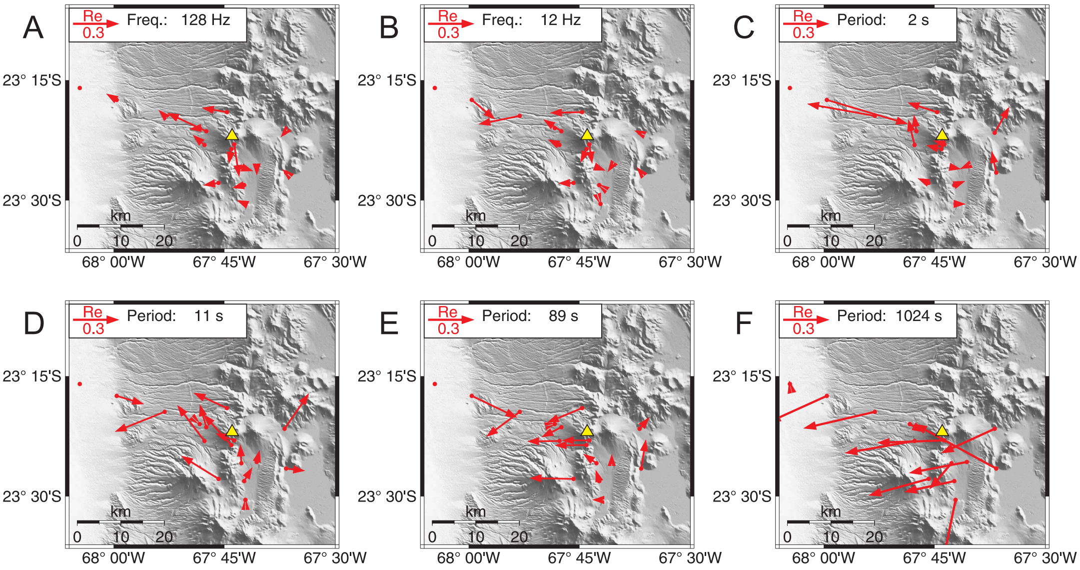

Figure 4.3: Real induction vectors of AMT stations for periods of 0.0078 s (frequency 128 Hz), 0.083 s (frequency 12 Hz), 2 s, 11 s, 89 s and 1024 s. Yellow triangle shows the position of Lascar volcano.

At first sight, no large conductive anomaly under Lascar volcano could be inferred from the analysis of the induction vectors of the stations surrounding it. For the shortest periods, the topography seems to play an important role as at the stations closer to the volcanic edifice the induction vectors point away from it, as can be seen in the images A and B in figure 4.3. However, for the period range between 1 s and 80 s, the AMT stations show a behavior which could be indicating the presence of a conductive anomaly in the SE of Lascar volcano (image D in figure 4.3), where small induction vectors are surrounded by larger ones pointing away from this zone.

4.2.2 Galvanic distortions and Skew parameters

In magnetotelluric surveys, localized heterogeneities in conductivity near the Earth's surface distort the electromagnetic response produced by the underlying conductivity structure under investigation. As the period of the MT signals increases, inductive effects produced by the near-surface structures decrease and eventually become negligible compared with the inductive response produced by the regional conductivity structure.

However, the presence of these small 3D structures at shallow depths in the study area produce distortions that are usually referred to as *static shift* effect, which can be caused by a multi-dimensional conductivity contrast having depths and dimensions less than the true penetration depth of the electromagnetic fields. Conductivity discontinuities cause local distortion of the amplitudes of electric fields as a result of conservation of electric charge, causing impedance magnitudes to be enhanced or diminished by real scaling factors. As a result, the apparent resistivity curves are affected by a parallel offset, but impedance phases are not affected. Except of some unusual cases where the distortion is very severe, the horizontal magnetic field components are not significantly affected and the distortion in the electromagnetic field is almost entirely confined to the electric field (Jiracek, 1990).

In order to solve this problem, distortion matrices are used to represent the distortion of electric fields by near-surface inhomogeneities. Using distortion matrices the distorted electric field is written as a function of the values the electric field would have had if the inhomogeneities were not present. Distortion matrices are useful when they can be determined well enough so that their effect on data can be removed, and the data can be interpreted using a simpler model, such as a 2D model (Smith, 1995).

A non-dimensional rotational invariant parameter which measures the departure from an ideal 2D model is the skew given by Swift (1967), considering:

$$S_1 = Z_{xx} + Z_{yy}; S_2 = Z_{xy} + Z_{yx} \tag{4.10}$$

$$D_1 = Z_{xx} - Z_{yy}; D_2 = Z_{xy} - Z_{yx} \tag{4.11}$$

The skew is given by:

$$\kappa \quad = \quad |S_1| \,/\, |D_2| \tag{4.12}$$

In the case of multi-dimensional heterogeneities with spatial dimensions significantly less than the inductive scale length of the data, superposed on a regional 2D structure, and decomposing the data into a local, non inductive response (galvanic) and a regional inductive response, the elements of the measured impedance tensor $\underline{Z}$ in the regional coordinate (x', y') system will be proportional to and in-phase with the elements of the regional impedance $\underline{Z}^r$ in the form (Bahr, 1988):

$$\underline{Z} = C \begin{bmatrix} 0 & Z^r_{x'y'} \\ Z^r_{y'x'} & 0 \end{bmatrix} = C\underline{Z}_{2D}$$

where C is the distortion matrix of frequency independent real numbers, a consequence of the distorted current which is in-phase with the regional electric field. However, in an arbitrary coordinate system (x, y), the phases of the two regional impedances will be mixed, as the elements of the tensor are linear combinations of the Z_{xy} and Z_{yx}.

$$\underline{Z} = \beta C \underline{Z}_{2D} \beta^T$$

The condition that in the coordinate system of the regional strike, the tensor elements within each column should have the same phase, allows to calculate the rotation angle which defines the rotation matrix β.

For cases in which no rotation angle can be found for which the phases in the respective columns of the impedance tensor are equal, Bahr (1991) proposes minimizing the phase difference between the elements of each column, δ.

$$\underline{Z} = \beta C \begin{bmatrix} Z_{yx} e^{i\delta} & Z_{xy} \\ Z_{yx} & Z_{xy} e^{-i\delta} \end{bmatrix} \beta^T$$

The presence of a phase difference between the elements of each column is expected if the anomalous magnetic fields are not negligible. In this sense Bahr (1988) found a non-dimensional rotational invariant parameter which is a measure for these phase differences, identified as the phase sensitive skew, η:

$$\eta = \frac{(|[D_1, S_2] - [S_1, D_2]|)^{1/2}}{|D_2|} \tag{4.13}$$

where,

$$[A, B] = Re(A)Im(B) - Re(B)Im(A)$$

with D_1, D_2, S_1 and S_2 as define in equations 4.10 and 4.11.

A skew value of zero supports the validity of the telluric distortion hypothesis, i.e., a perfect regional 2D model can be identified, while greater values indicate the departure of this assumption. Bahr gave a limit of 0.1 to test the validity of the galvanic model, and 0.3 for the validity of this model with small phase differences. A surpass of this limit could reflect the non-validity of this model, which means that 3D inductive structures are present.

The skew according to Swift's model, and also the phase sensitive skew for all the period range were calculated along the LMT profile. Considering both definitions given in equations 4.12 and 4.13, these values are shown as contour plots in figure 4.4.

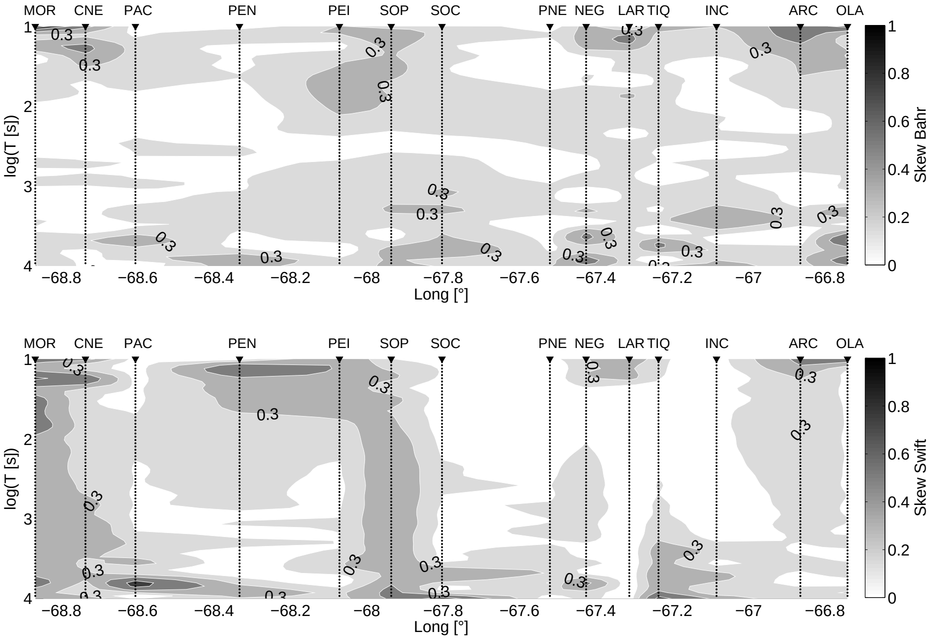

Figure 4.4: LMT profile showing the skewness in the definitions of Bahr (above) and Swift (below). White and light tones indicate a skewness below 0.3, as a tentative measure for two-dimensionality.

The same situation as in the induction vectors analysis is present, with a relatively high skewness for the shorter periods in several stations. A strong influence of the Salar de Atacama basin can be seen in the Swift's skew values for the stations PEN and PEI, but that does not affect the phase sensitive skew. For periods around 100 s (and larger for Swift's skew) between stations PEI and SOP, the rise in the skewness until 0.3 could be related with the presence of intrusive rocks belonging to the Cas formation. However, the small skew values in a wide period range and for most of the stations measured along this profile shows the good agreement with the 2D assumption in this zone, for periods between 10 s and 10000 s.

Analyzing now shallower depths with the AMT data, the skew is showing small values for shortest periods at most stations, but an increase in the skewness starts at 0.1 or 1 s, extending until 10 s in some cases (stations L01 or L02 in figure 4.5) and until almost 100 s for some other stations (stations L03, L08 or L09 in figure 4.5).

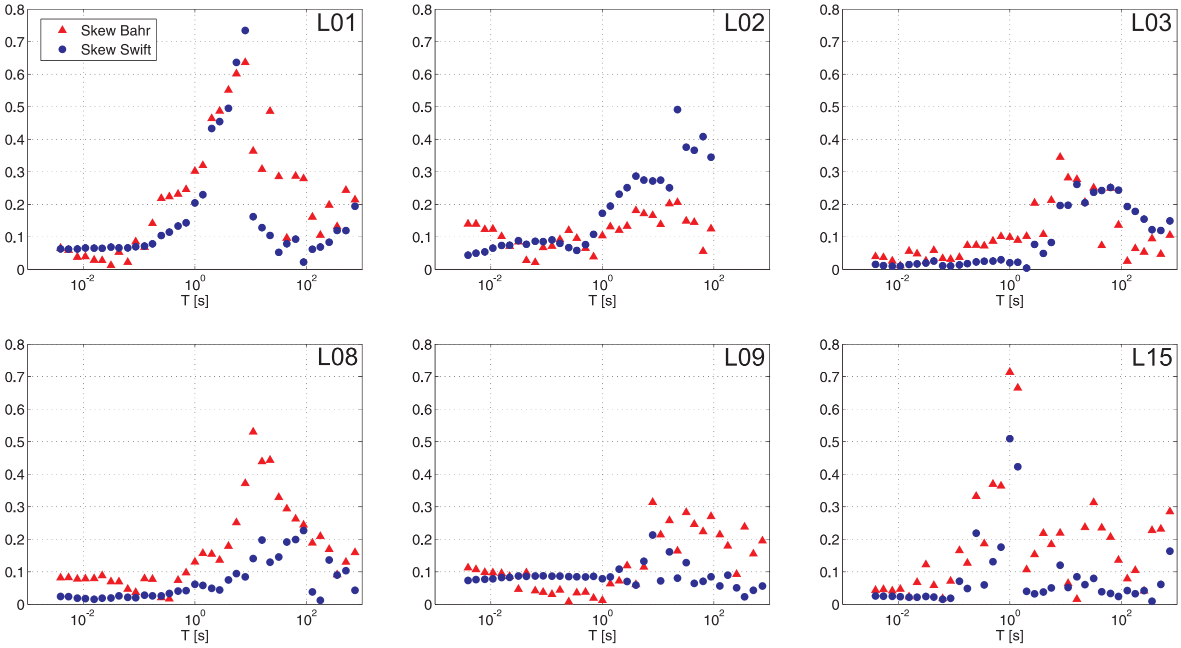

Figure 4.5: Skew for six AMT stations according to Swift (blue circles) and Bahr (red triangles) definitions. Note that very high skew values in L01 and L15 between 1 s and 10 s are due to noise.

4.2.3 Determination of the regional strike direction

There are many occasions on which the magnetotelluric impedance tensor is affected by local galvanic distortion of electric currents arising from induction in a conductive structure which is approximately 2D on a regional scale. Even though the inductive behavior is 2D, the resulting impedance tensor can be shown to have a 3D behavior. Decompositions of the impedance tensor which separates the effects of 3-D channeling from those of 2-D induction have been presented by Bahr (1988), Groom and Bailey (1989) and Smith (1995).

Considering a galvanic electric field E^g caused by electric charges that accumulate along conductivity boundaries, and a regional electric field E^r, the galvanic electric field can be written in terms of the regional electric field, following Smith (1995).

$$E^g(E^r_x) = \begin{pmatrix} a \\ b \end{pmatrix} E^r_x$$

$$E^g(E^r_y) = \begin{pmatrix} c \\ d \end{pmatrix} E^r_y$$

Then, the measured electric field can be written as a sum of the galvanic and regional electric fields.

$$\begin{pmatrix} E_x^m \\ E_y^m \end{pmatrix} = \begin{pmatrix} 1+a & c \\ b & 1+d \end{pmatrix} \begin{pmatrix} E_x^r \\ E_y^r \end{pmatrix} = DE^r$$

This matrix D is then the distortion matrix, similar to the matrix C in the previous section. Now, using a different parametrization, D can be written in a different way, as follows.

$$D = \left[g_x \begin{pmatrix} cos\beta_x \\ sin\beta_x \end{pmatrix} \quad g_y \begin{pmatrix} -sin\beta_y \\ cos\beta_y \end{pmatrix} \right] \tag{4.14}$$

The quantity g_x is the amount in which the regional electric field in the x direction is amplified, and β_x is the amount this electric field has been rotated clockwise. The values g_y and β_y have an equivalent meaning but for the y direction.

Considering now equation 4.14 and using this distorion matrix to relate Z^m and Z^r.

$$\underline{Z}^m = D\underline{Z}^r = \begin{bmatrix} cos\beta_x & -sin\beta_y \\ sin\beta_x & cos\beta_y \end{bmatrix} \begin{bmatrix} g_x Z_{11}^r & g_x Z_{12}^r \\ g_y Z_{21}^r & g_y Z_{22}^r \end{bmatrix}$$

As there are four known complex components in the Z^m matrix (measured) and twelve unknowns ($g_x, g_y, \beta_x, \beta_y$, and the 4 complex $Z_i^r j$), the system has eight real equations for twelve unknowns. To solve this undetermined system, the least restrictive assumption is that the regional geology is 2D. Then, in a coordinate system aligned with the regional strike, the diagonal elements of the regional impedance vanish, and the previous equation is reduced to

$$\underline{\tilde{Z}}^m = \begin{bmatrix} cos\beta_x & -sin\beta_y \\ sin\beta_x & cos\beta_y \end{bmatrix} \begin{bmatrix} 0 & g_x Z_{12}^r \\ g_y Z_{21}^r & 0 \end{bmatrix}$$

Now the system can be solved with eight real equations for six real unknowns, and the problem is now overdetermined.

Since β_x and β_y are frequency independent, estimates of their values can be improved by estimating them together with a set of values of $g_x Z^r_{12}$ and $g_y Z^r_{21}$ simultaneously at n different frequencies, by minimizing the total misfit between the measured $\underline{Z}^m$ and the estimated $\underline{\tilde{Z}}^m$ over the n frequencies. Previous equation can be re-written as.

$$\underline{\tilde{Z}}^m_i = \begin{bmatrix} 1 & \tilde{c} \\ \tilde{b} & 1 \end{bmatrix} \begin{bmatrix} 0 & Z^i_{12} \\ Z^i_{21} & 0 \end{bmatrix}$$

Where $Z^i_{12} = g_x Z^r_{12} cos\beta_x$, $Z^i_{21} = g_y Z^r_{21} cos\beta_y$, and $\underline{\tilde{Z}}^m_i$ is referred to the value at the ith frequency, while $\tilde{b} = tan\beta_x$ and $\tilde{c} = -tan\beta_y$ are frequency independent.

Using an iterative program based on the previous theory, developed by Smith (1995), it was possible to calculate the strike direction for different ranges of frequencies. The strike direction determination for the LMT profile, with data between 10 s and 10000 s was calculated for the whole period range and also for three subdivisions, trying to show the behavior of the shallower (10-100 s), intermediate (100-1000 s) and deeper structures (1000-10000 s).

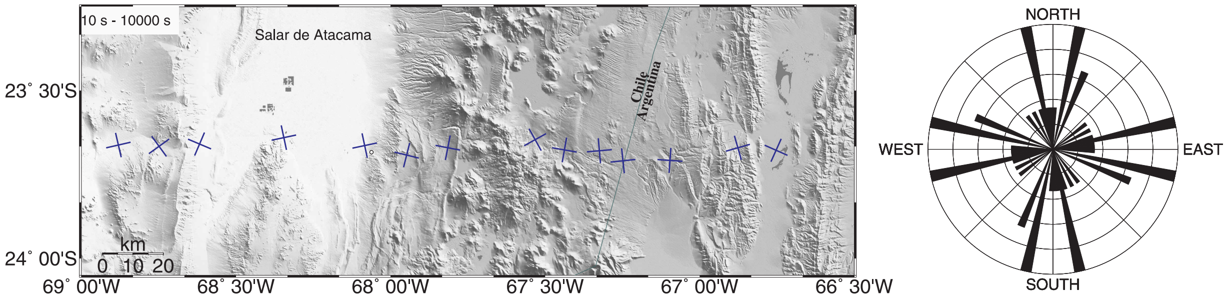

Figure 4.6: Strike direction determined for each LMT station and rose diagram calculated for the total period range between 10 s and 10000 s.

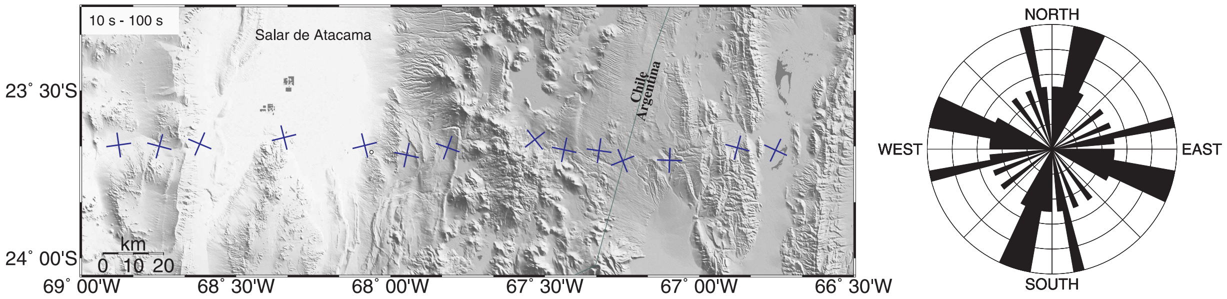

Figure 4.7: Strike direction determined for each LMT station and Rose diagram calculated for a period range between 10 s and 100 s.

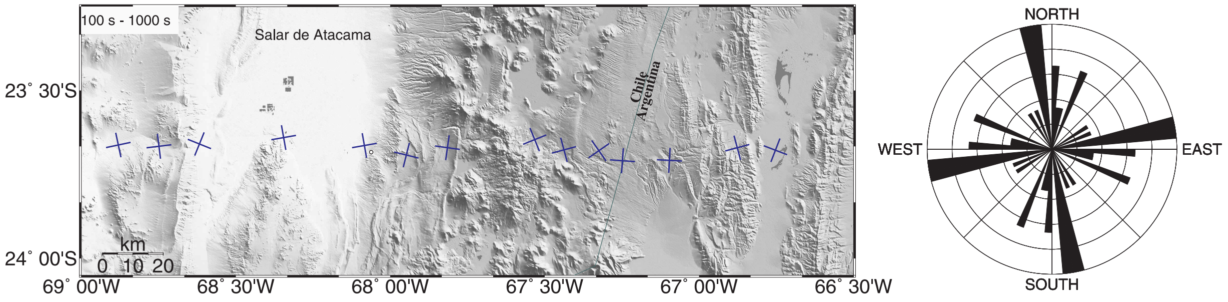

Figure 4.8: Strike direction determined for each LMT station and Rose diagram calculated for a period range between 100 s and 1000 s.

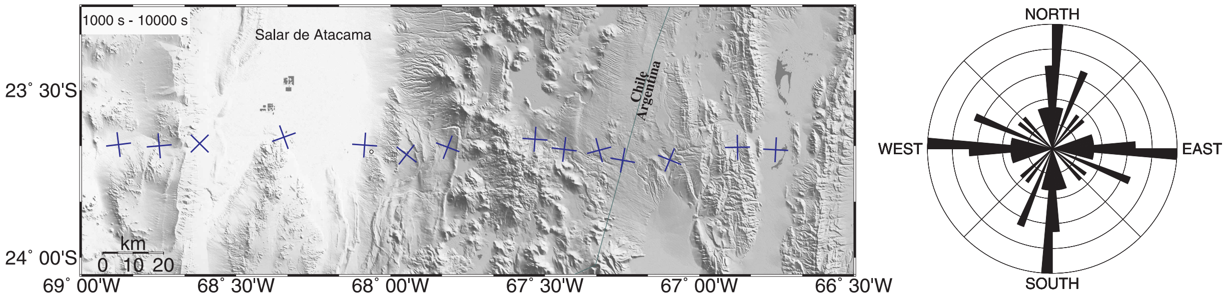

Figure 4.9: Strike direction determined for each LMT station and Rose diagram calculated for a period range between 1000 s and 10000 s.

Looking at this analysis for the three decades of periods separately, it becomes clear that the data for shallower depths has a 3D behavior, especially in the forearc where the influence of the Salar de Atacama basin in the stations close to it is very strong. The presence of a regional strike can be well determined for the period range between 100 s and 10000 s with a value close to -10° from the north. This result is consistent with the previously calculated induction vectors, showing no general pattern for the shorter periods until 80 s, and behaving more uniformly from there on.

The strike direction was also calculated for the AMT data, obtaining a similar result as in the LMT case, with no clear direction for periods shorter than 10 s, as can be seen in figure 4.10. The strike direction for the shortest period range (0.01 s - 0.1 s), not shown in this figure, is also not showing a clear direction.

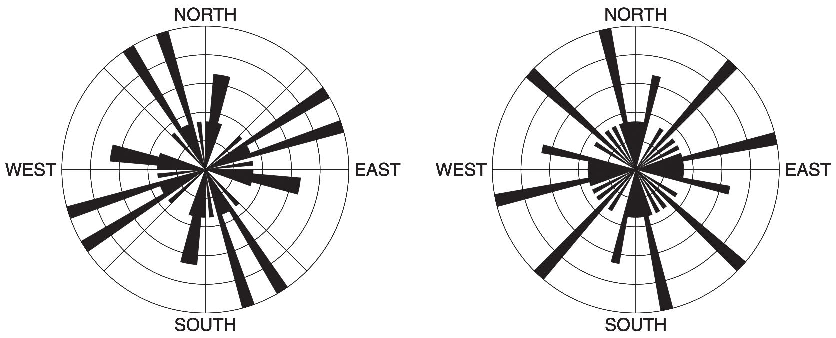

0.1 s - 1 s 1 s - 10 s

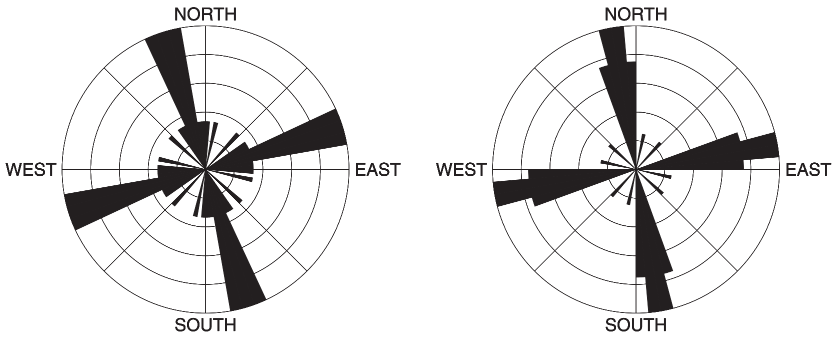

10 s - 100 s 100 s - 1000 s

Figure 4.10: Strike direction for the AMT stations calculated for 4 period ranges.

As with the AMT stations we measured periods between 0.0039 s and 1000 s, this result is more critical as in the LMT case, because a large part of our data can not be treated as 2D. Therefore, a 3D model is required to explain the data measured around Lascar volcano, especially for the first km in depth. Different is the case for the LMT profile, for which the 2D supposition seems to fit the measured data well.

4.2.4 Phase tensor analysis

Although the amplitude of the observed electric field may be drastically distorted by a near surface heterogeneity, the phase relationship between the electric and magnetic field vectors will be virtually unaffected for this galvanic distortions. MT distortion analysis seeks then to recover the regional phase relationship from a set of distorted measurements, even when both the near surface heterogeneity and the regional conductivity structures are 3D.

It is possible to write E^m (measured field) in terms of the impedance tensor considering, as in the previous sections, a 2x2 real distortion matrix D, and the regional fields (E^r and B^r) as follows:

$$\vec{E}^r(\omega) = \underline{Z}^r(\omega)\vec{B}^r(\omega) \Rightarrow \vec{E}^m = D\vec{E}^r = D(\underline{Z}^r\vec{B}^r) = (D\underline{Z}^r)\vec{B}^m \Rightarrow \underline{Z}^m = D\underline{Z}^r$$

The conditions under which $B^m = B^r$ is a good approximation are discussed in Groom and Bahr (1992), Singer (1992), Chave and Smith (1994) and Utada and Munekane (2000).

According to these representations, $\underline{Z}$ can be separated in its real (R) and imaginary (I) part as follows.

$$\underline{Z}^m = R^m + iI^m$$
$$\underline{Z}^r = R^r + iI^r \Rightarrow R^m = DR^r \text{ and } I^m = DI^r$$

Defining the phase tensor now, and using the equations above:

$$\Phi^m = (R^m)^{-1}I^m = (DR^r)^{-1}DI^r = (R^r)^{-1}D^{-1}DI^r = (R^r)^{-1}I^r = \Phi^r$$

Thus the observed and regional phase tensors are identical and independent of the distortion tensor. No assumptions have been made about the nature or dimensionality of the regional conductivity structure.

Written in terms of the real and imaginary components of $\underline{Z}$ in a Cartesian coordinate system (x,y), the phase tensor Φ can be written as the following matrix.

$$\Phi = \begin{bmatrix} \Phi_{xx} & \Phi_{xy} \\ \Phi_{yx} & \Phi_{yy} \end{bmatrix} = \frac{1}{det(R)} \begin{bmatrix} R_{yy}I_{xx} - R_{xy}I_{yx} & R_{yy}I_{xy} - R_{xy}I_{yy} \\ R_{xx}I_{yx} - R_{yx}I_{xx} & R_{xx}I_{yy} - R_{yx}I_{xy} \end{bmatrix}$$

Where $det(R) = R_{xx}R_{yy} - R_{yx}R_{xy}$ is the determinant of R.

For a graphical representation of the phase tensor, it is necessary to introduce some other parameters. These are the following.

$$
\begin{aligned}
\beta &= \frac{1}{2}tan^{-1}\left(\frac{\Phi_{xy}-\Phi_{yx}}{\Phi_{xx}+\Phi_{yy}}\right)\\
\alpha &= \frac{1}{2}tan^{-1}\left(\frac{\Phi_{xy}+\Phi_{yx}}{\Phi_{xx}-\Phi_{yy}}\right)\\
\Phi_{max} &= ({\Phi_1}^2+{\Phi_3}^2)+({\Phi_1}^2+{\Phi_3}^2-{\Phi_2}^2)^{1/2}\\
\Phi_{min} &= ({\Phi_1}^2+{\Phi_3}^2)-({\Phi_1}^2+{\Phi_3}^2-{\Phi_2}^2)^{1/2}
\end{aligned}
\tag{4.15}
$$

with Φ_1, Φ_2 and Φ_3 defined by,

$$
\begin{aligned}
\Phi_1 &= trace(\Phi)/2 = (\Phi_{xx}+\Phi_{yy})/2\\
\Phi_2 &= \sqrt{det(\Phi)} = \sqrt{\Phi_{xx}\Phi_{yy}-\Phi_{xy}\Phi_{yx}}\\
\Phi_3 &= skew(\Phi)/2 = (\Phi_{xy}-\Phi_{yx})/2
\end{aligned}
$$

With the parameters defined in equations 4.15, the graphical representation of the phase tensor as an ellipse can be shown with the following figure.

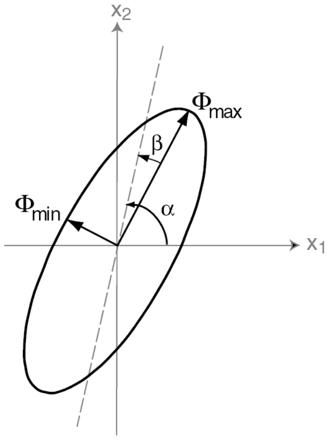

Figure 4.11: Graphical representation of the phase tensor (Caldwell et al., 2004).

The major and minor axes of the ellipse represent the principal axes and values of the tensor with the orientation of the major axis specified by the angle $\alpha-\beta$. If the phase tensor is symmetric ($\beta = 0$), the orientation of the major axis is given by α. In the general case, the skew angle (β) is non-zero and represents the rotation of the major axis of the phase tensor ellipse away from an identically shaped ellipse represented by a symmetric tensor.

Different cases can be represented by the phase tensor ellipses. For an uniform half-space, a circle of unit radius represents the phase tensor at all periods. If the conductivity is both isotropic and 1-D, the radius of the circle will vary with period according to the variation of conductivity with depth. In a 2D, or quasi 2D, situation where β is zero or close to zero, respectively, the phase-tensor ellipse will have either its major or minor axes aligned with the geoelectric strike direction.

The phase tensor analysis was applied to our AMT and LMT data. Starting with the LMT data, we obtain the following results.

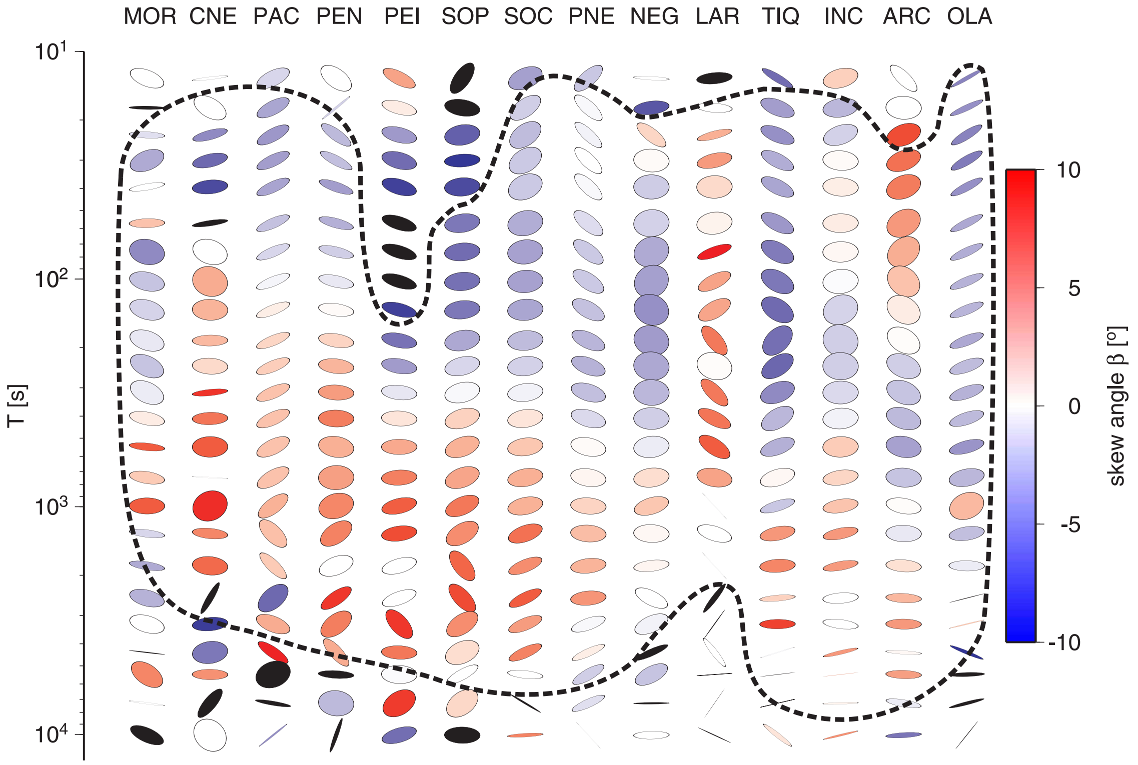

Figure 4.12: Phase tensor ellipses for the LMT profile normalized by the maximum phase value, color scale represents β. The ellipses are plotted so that the horizontal axis corresponds to an east-west orientation. The segmented line encloses the ellipses with $|\beta| < 5$

As seen in figure 4.12, the small β values together with a consistent direction of the major semi axis is showing a behavior consistent with the 2D case in a large part of the period range for most of the measured stations. Many of the stations present an unsettled behavior for longer periods, probably due to a poor data quality. A different case seems to be present under stations PEI and SOP, where larger values of β were obtained, until periods around 100 s. This result is consistent with the Bahr's and Swift's skew values shown in section 4.2.2, with a high skew value in the same part of the profile.

Now, the color of the ellipses shows Φ_{min}, parameter which is an indicator of the vertical conductivity gradient; values greater than 45° indicate increasing conductivity with increasing depth.

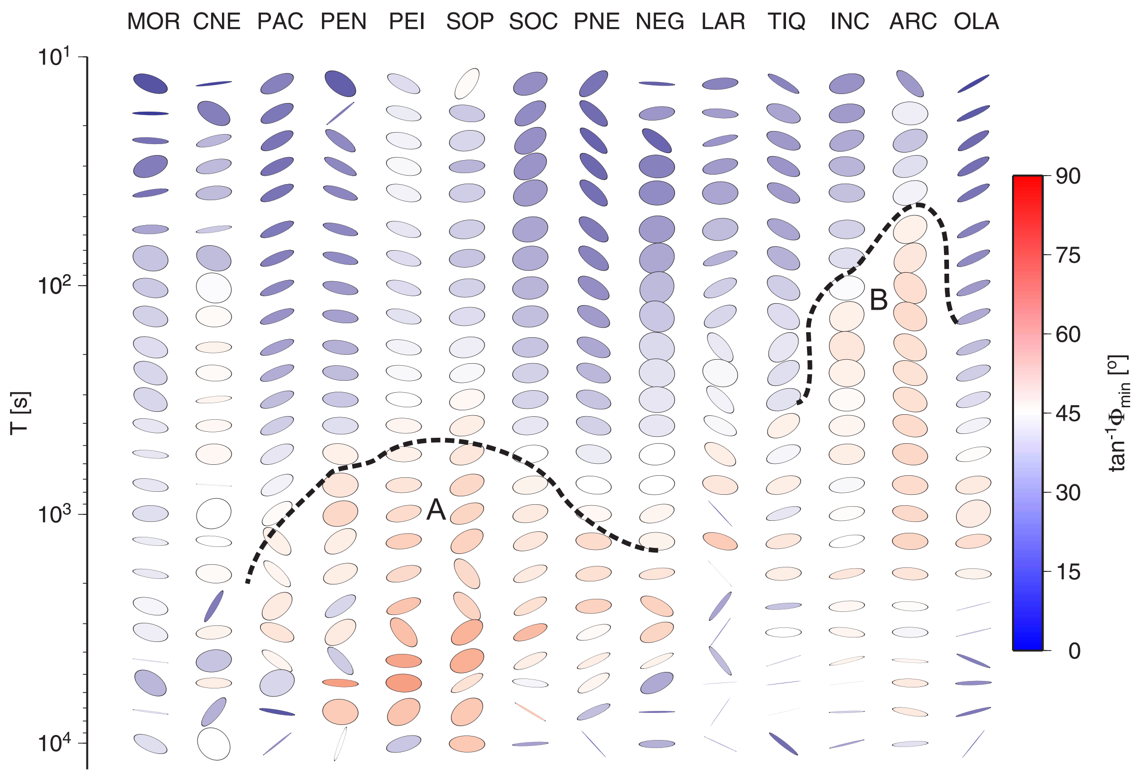

Figure 4.13: Phase tensor ellipses for the LMT profile normalized by the maximum phase value, color scale represents Φ_{min}. The segmented line encloses the ellipses with a $tan^{-1}\Phi_{min} > 45$, indicating increasing conductivity with depth.

Two zones with a relatively high Φ_{min} are present in the LMT profile, which could be indicating the presence of conductive zones. Especially interesting is the zone marked as B in figure 4.13, which is coincident with the hypothesis of a conductive zone under the Puna, signaled by the analysis of the induction vectors for periods between 100 s and 1000 s.

A phase tensor analysis was also developed for the AMT stations. In this case, the phase tensor ellipses are showing a relatively small β value, but with large variation in the major axis direction of the ellipses, especially for the shorter periods, indicating the inappropriateness of a 2D analysis. In figure 4.14, the phase tensor ellipses for the AMT data are colored representing Φ_2, a coordinate invariant which represents the geometric mean of the maximum and minimum phase differences between the magnetic and electric field, that is, the phase averaged over the inducing field's polarization direction (Heise et al., 2008; Hill et al., 2009). As Φ_{min}, this parameter provides an indicator of the vertical conductivity gradient.

For the AMT stations, a high value of Φ_2 is present in the stations placed to the S-SE of the volcano. At periods between 0.1 s and 1 s this behavior is also present in stations L07 and L08, placed at the southern slope of the volcanic edifice, and also at the stations to the S.

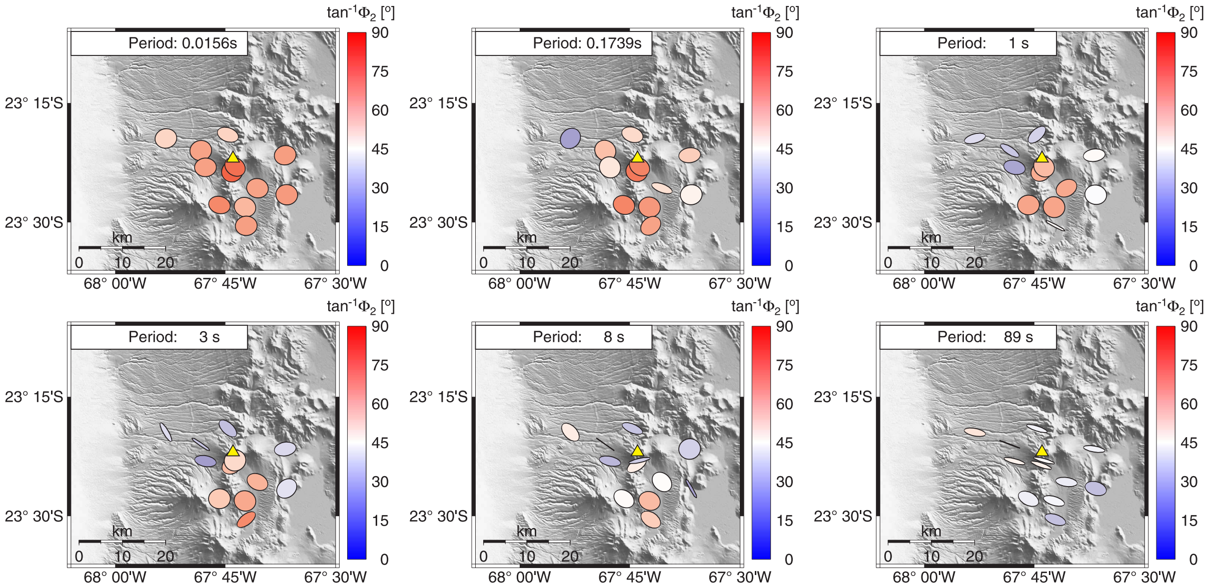

Figure 4.14: Phase tensor ellipses for the AMT stations normalized by the maximum phase value, color scale represents the $\tan^{-1}\Phi_2$, with $\Phi_2 = \sqrt{\Phi_{max}\Phi_{min}}$. Yellow triangle shows the position of Lascar volcano.

Beyond 1 s, and until almost 10 s, Φ_2 becomes slowly smaller for the stations closer to the volcano (L07 and L08), but the stations to the south (L09, L16, L15 and L12) are still showing higher values. This could indicate the presence of a highly conductive zone located at 1-5 km depth to the south of the volcano, which is getting closer to the volcano from the south as the depth decreases. The presence of a conductive zone to the south of the volcano at these periods was also mentioned in the induction vectors analysis section. In order to clarify the presence of features such as the one indicated in the previous lines, 3D models were developed, and the results are presented in the following chapters.

Chapter 5

Inversions and Models

5.1 2D Inversion of LMT data

According to the results obtained in the dimensionality analysis shown in the previous chapter, a 2D model along the LMT profile could describe successfully the measured data. A 2D inversion model was obtained using the Nonlinear Conjugate Gradients algorithm (NLCG), implemented by Rodi and Mackie (2001).

The strongly ill-posed nonlinear inverse problem of calculating the subsurface conductivity distribution from magnetotelluric data, is solved with a 2D smooth model inversion routine which finds regularized solutions (Tikhonov-type regularization) using the method of nonlinear conjugate gradients by minimizing the objective function:

$$S(m) = ||W_d(d - F(m))||^2 + \tau ||W_m(m - m_0)||^2 \tag{5.1}$$

with d denoting the data vector, m the model vector, W_d a data weight matrix (usually the data variances) and τ the regularization parameter. $F(m)$ is the model response, m_0 the starting or an a priori model, $||...||$ the norm, and W_m the regularization operator, often set as the Laplacian $(\nabla^2 m)^2$. W_m incorporates a weighting function $w(x, z)$ allowing to penalize horizontal or vertical exaggeration of model structures (R. Mackie, 2-D inversion manual):

$$m^t W_m^t W_m m \approx \int w(x, z)(\nabla^2 m)^2 dA \tag{5.2}$$

integration is over model area A. If an uniform grid is chosen for W_m, then

$$
\begin{aligned}
w(z) &= (z(k)/z_0)^\beta \;\; for \;\; z_k > z_0 \;\; and && (5.3) \\
w(z) &= 1 \;\; for \;\; z_k \leq z_0 && (5.4)
\end{aligned}
$$

where $z(k)$ is the thickness of the k-th row and z_0 the minimum block thickness, which has to be set manually.

As a graded grid was used (which is common in broadband electromagnetic modeling), this procedure may lead to artifacts if vertical and horizontal grid spacings are very different. Therefore grid spacing was kept as uniform as possible within the region of interest. We used this code to invert tipper data, E and B polarization resistivities and phases separately and also jointly.

The misfit between data and model response is calculated as a root mean square error according to:

$$
RMS = \sqrt{\frac{(d - F(m))^t {W_d}^{-1} (d - F(m))}{N}} \tag{5.5}
$$

with N = number of data points. Under practical conditions, W_d contains only the main diagonal, i.e., the data variances. Note that this misfit measure depends on the data errors and care must be taken if analyzing a model fit by looking at the RMS alone; this is particularly important if an error floor is set.

In the NLCG implemented in the WinGLink software package (version 2.20.02), some of the main parameters which control the inversion are the following.

- Smoothest model or variations: The program can solve for the smoothest model or the smoothest variations away from the starting model. Choosing smoothest variations is a useful way to do hypothesis testing for different model parameters or features.
- Regularization Laplacian: It is possible to specify either a uniform grid Laplacian (which assumes for the purposes of computing the regularization function that the dimensions of the model are all equal) or standard Laplacian on the actual model mesh. The uniform grid Laplacian may produce smoother models, but at the expense of smearing features both vertically and horizontally. The standard Laplacian may produce a rougher-looking model, but the definition of smoothness is consistent with the model dimensions.
- Regularization Order: It's possible to minimize the gradients $|\nabla m|^2$ of the model, or the Laplacian $(\nabla^2 m)^2$ of the model.
- τ for smoothing operator: Is the regularization parameter that controls the trade-off between fitting the data and adhering to the model constraint. Larger values cause a smoother model at the expense of a worse data fit.
- Weighting function: The first option specifies the α factor to multiply horizontal derivatives. A value of 1.0 is recommended unless you want to increase the horizontal smoothness. The second line specifies β in the weighting function. A value of 3.0 is recommended if minimizing $(\nabla^2 m)^2$

and a value of 1.0 is recommended if minimizing $|\nabla m|^2$. If one set the value to zero, then no weighting is applied to the regularization term.
- Error Floor: Input errors that are below this value will be reset to this value. The error floor for phase is entered in percentage.

Numerous experiments have to be conducted to achieve a best-fitting and reliable final model. These tests, which should be a standard procedure in non-linear, regularized inversion, are briefly mentioned here: 1) variation of the starting model and influence of the ocean; 2) exploration of model space by varying the regularization parameter τ, yielding a trade-off curve (ideally L-shaped) between RMS fit (root mean square) and model roughness (Asters et al., 2005); 3) assigning specific error floors to individual components, i.e., TE and TM mode resistivities and phases, and tipper data, as well as checking for static effects; 4) sensitivity tests and tests of (in)significant model features; 5) discretization; 6) convergence and number of iterations. Another important aspect is to check individual components separately: due to different boundary conditions at interfaces, TE and TM mode impedances and geomagnetic transfer functions are sensitive to different subsurface structures

Typical values used for the different parameters controlling the inversion are the following.
- Solve for the smoothest model
- Minimize the integral of the Laplacian $(\nabla^2 m)^2$
- Error Floor for ρ: 20 %
- Error Floor for ϕ: 5°
- T_{yz} Data (error floor for H_z): 0.02 (abs.)
- Minimum frequency: 0.0001 for LMT data
- τ for smoothing operator: For the determination of this parameter, an analysis of the trade-off between data fitting (RMS) and smoothness of the model is necessary. Figure 5.1 is showing a plot relating these two values.

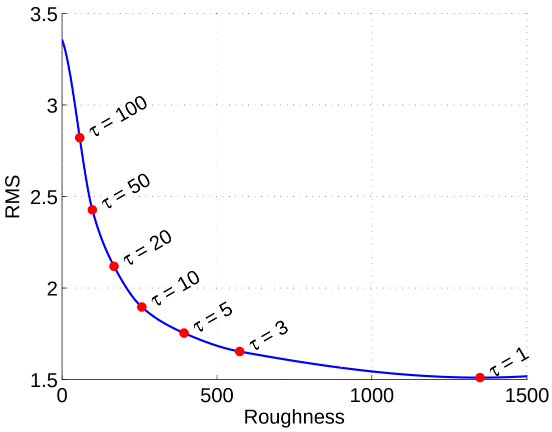

Figure 5.1: Tradeoff between roughness and RMS. The roughness is controlled by τ indicated in this plot next to the red dots.

A value of τ = 10 was selected as a good trade-off between data fitting and smoothness. For larger values, the RMS increase rapidly, while for smaller values, the RMS become smaller but the smoothness of the model decreases strongly.

With the previously defined parameters and the data measured in the first field campaign (2007), during 2008 and 2009 several 2D inversions were run in order to achieve a reliable result, obtaining the model shown in figure 5.2.

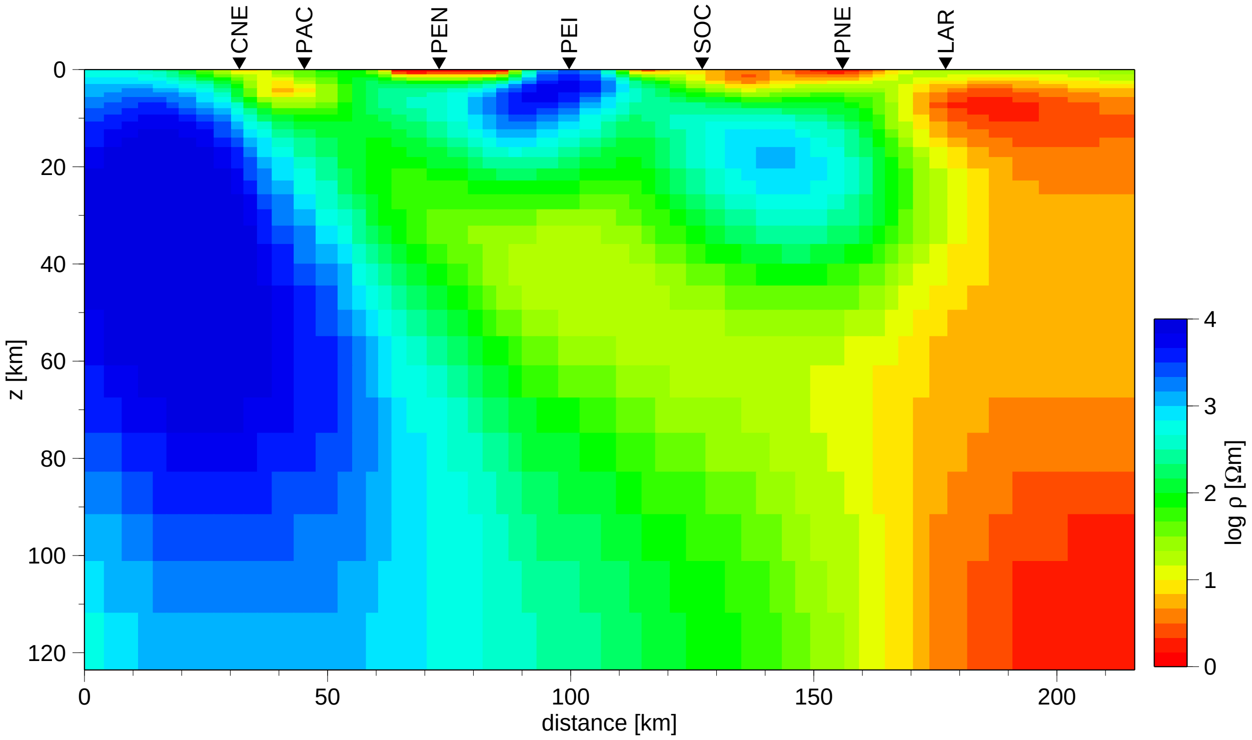

Figure 5.2: 2D inversion of LMT data (10 s - 10000 s) measured during the first field campaign in 2007. RMS: 1.759

One of the most interesting features of the 2D inversion result shown in figure 5.2 is the large highly conductive zone present at the eastern border of the profile, which seems to be the source of the induction vector's behavior at 500-1000 s, and which can be seen in all the stations. The presence of this conductive zone just outside the profile was tested by several sensitivity tests, but in order to constrain its size and extension, more stations to the east of the profile were needed. The lack of stations in this part of the profile, as well as some gaps in the original profile were solved in the second field campaign carried out during January and February 2010.

Now including the new data set available, new 2D inversions for this profile were made considering a starting model which includes the Pacific Ocean in the westenrmost side, the Salar de Atacama basin and the subducting slab. The sea was represented as a very conductive layer of 0.3 Ωm, extending from the coast and reaching depths of 6 km in the trench. The other very conductive zone, the Salar de Atacama basin, was also represented with a resistivity of 0.1 Ωm, but reaching a depth of 1 km. On the other hand, the subducting slab was represented as a resistive zone of 500 Ωm, extending in depth from the trench to the east, approximating the depths of the Wadati-Benioff zone indicated by Cahill and Isacks (1992). These features were part of the starting solution, but were not locked in the grid, so they could change their values with every iteration.

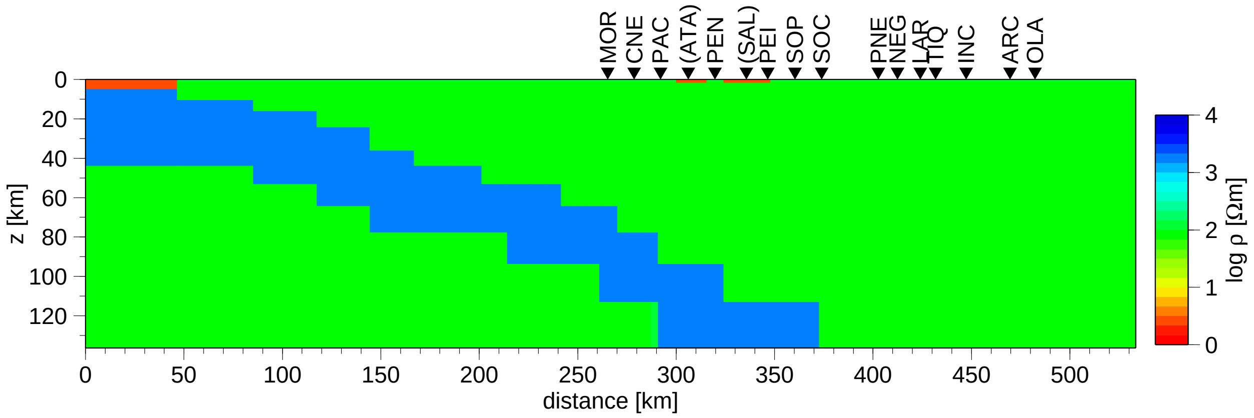

Figure 5.3: Starting model for the inversion of LMT data including the sea (red layer, top left) and the Salar de Atacama basin (red layer, top center) as conductive layers, and the subducting slab as a resistive zone (in light blue).

The frequency range used in the inversion of this profile is between 0.0001 Hz and 0.1 Hz for the LMT data. Several inversions were calculated, in order to see the changes that each of the parameters that control the inversion produce.

Stations ATA and SAL were placed directly in the Salar de Atacama basin and due to the impossibility of digging holes for electric probes, due to the extremely hard saline cover found in the central part of this basin, their data consist of magnetic field measurements and no electric field data is available for these stations. Without the impedance tensor, both stations were used only in the inversions of tipper data. The 2D inversion of tipper data and a 2D inversion (without stations ATA and SAL) with a starting model as shown in figure 5.3 and the typical values described previously, is also presented in figure 5.4

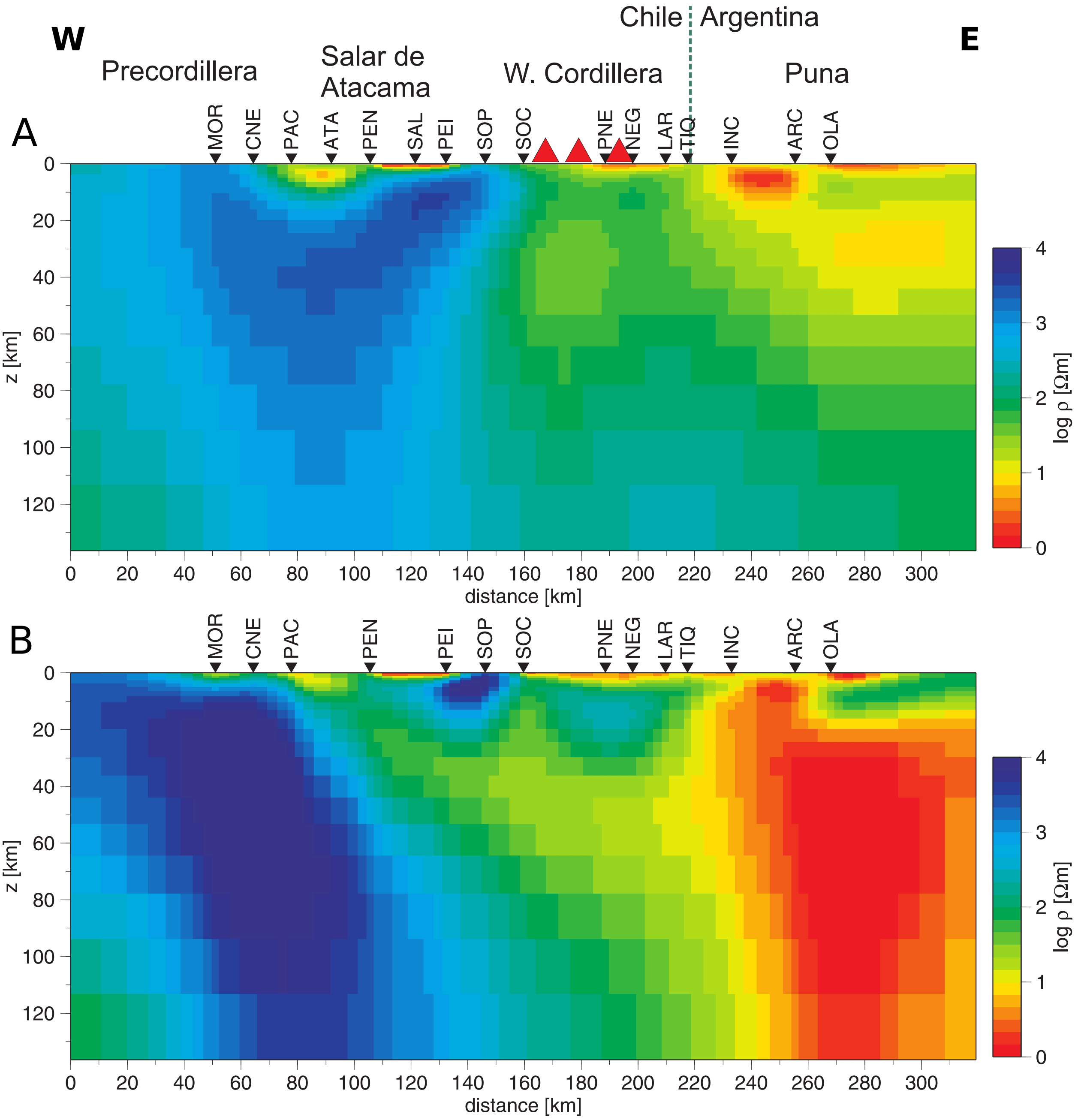

Figure 5.4: 2D inversion of LMT data. (A) 2D inversion of tipper data only, including stations ATA and SAL, RMS: 1.661. (B) 2D inversion of tipper, TE and TM modes, RMS: 1.957. Note that stations ATA and SAL were not considered for the joint inversion shown in the image below, as for these stations no electric fields but only magnetic fields were measured.

The 2D inversion with TE mode, TM mode and tipper (shown in figure5.4 B) has a RMS of 1.957, where the fitting between the measured and calculated values for each station can be seen in figure 5.5.

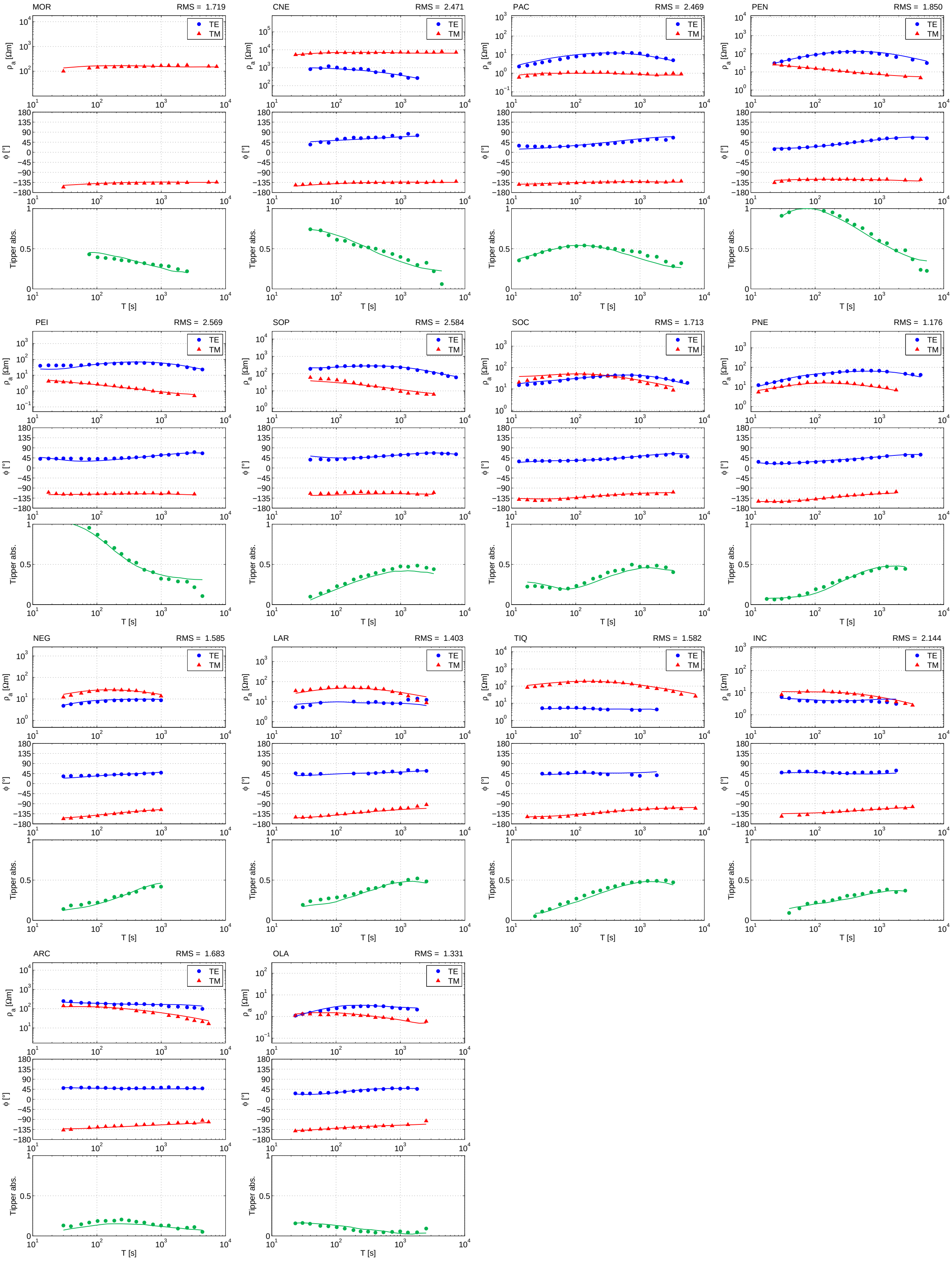

Figure 5.5: Comparison between measured and calculated data from the 2D inversion of TE, TM and tipper shown in figure 5.4 B. Dots are measured data and curves are the data calculated with the 2D inversion program.

Concerning the starting model used for the previously shown 2D inversion, no significant changes were obtained by using this kind of starting model (shown in figure 5.3) instead of an homogeneous half-space of 100 Ωm, as the same features that characterize the previously shown 2D inversion are present in both cases.

Sensitivity tests were carried out in order to estimate the effects of changes in the parameters, and the robustness of the features characterizing these 2D inversions. Only slight changes in the shape of these features were observed, and their relative position and size remained practically unchanged. Several tests were also carried out in order to better resolve the boundaries of these features, especially with regard to depth extent. For the highly conductive zone below the Puna, which in the inversion result is reaching depths of ∼120 km, several test were tried with the 2D forward modeling tool, using the inversion result as starting model. The relative conductive zone which seems to escape from the highly conductive zone beneath the Puna, and which is extending until 40-50 km below the volcanic arc was also tested, in order to discard possible artifacts needed for the 2D inversion process. Setting the resistivity of this zone to a value of 100 Ωm instead of 10-20 Ωm presented in the model shown in figure 5.4 B, the model responses present some slight but perceptible changes as shown in figure 5.6.

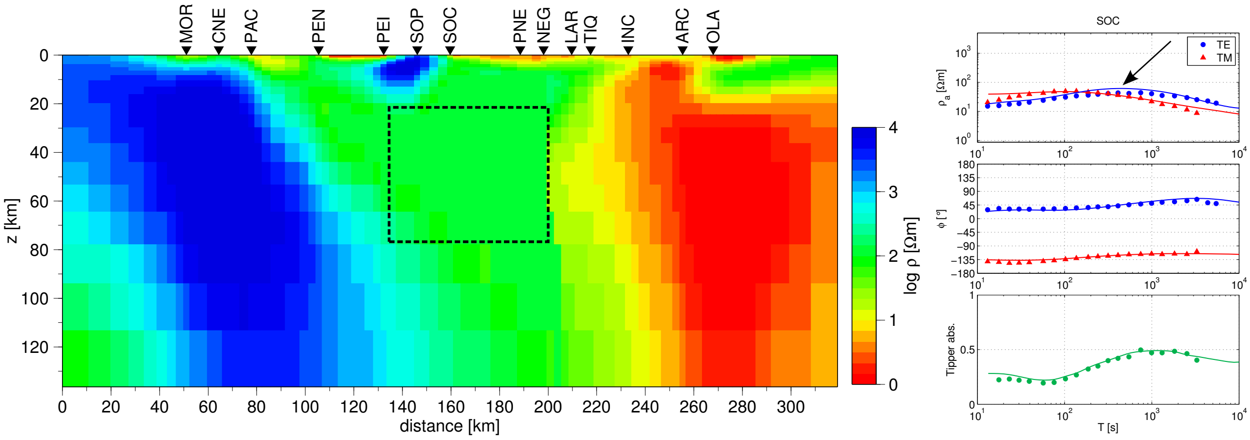

Figure 5.6: Comparison between measured data (dots) and model responses (lines) for station SOC, located in the western border of the volcanic arc for a forward model based on the 2D inversion result shown in figure 5.4 B, without the relatively conductive zone beneath the volcanic arc (enclosed by a segmented line). The black arrow is indicating the slight but perceptible misfit between 100 and 1000 s in the TE curve due to the absence of the relatively conductive zone.

Now, changing the resistivity to a value of 100 Ωm below the highly conductive zone beneath the Puna, and setting its bottom at different depths, the obtained results are shown in figure 5.7.

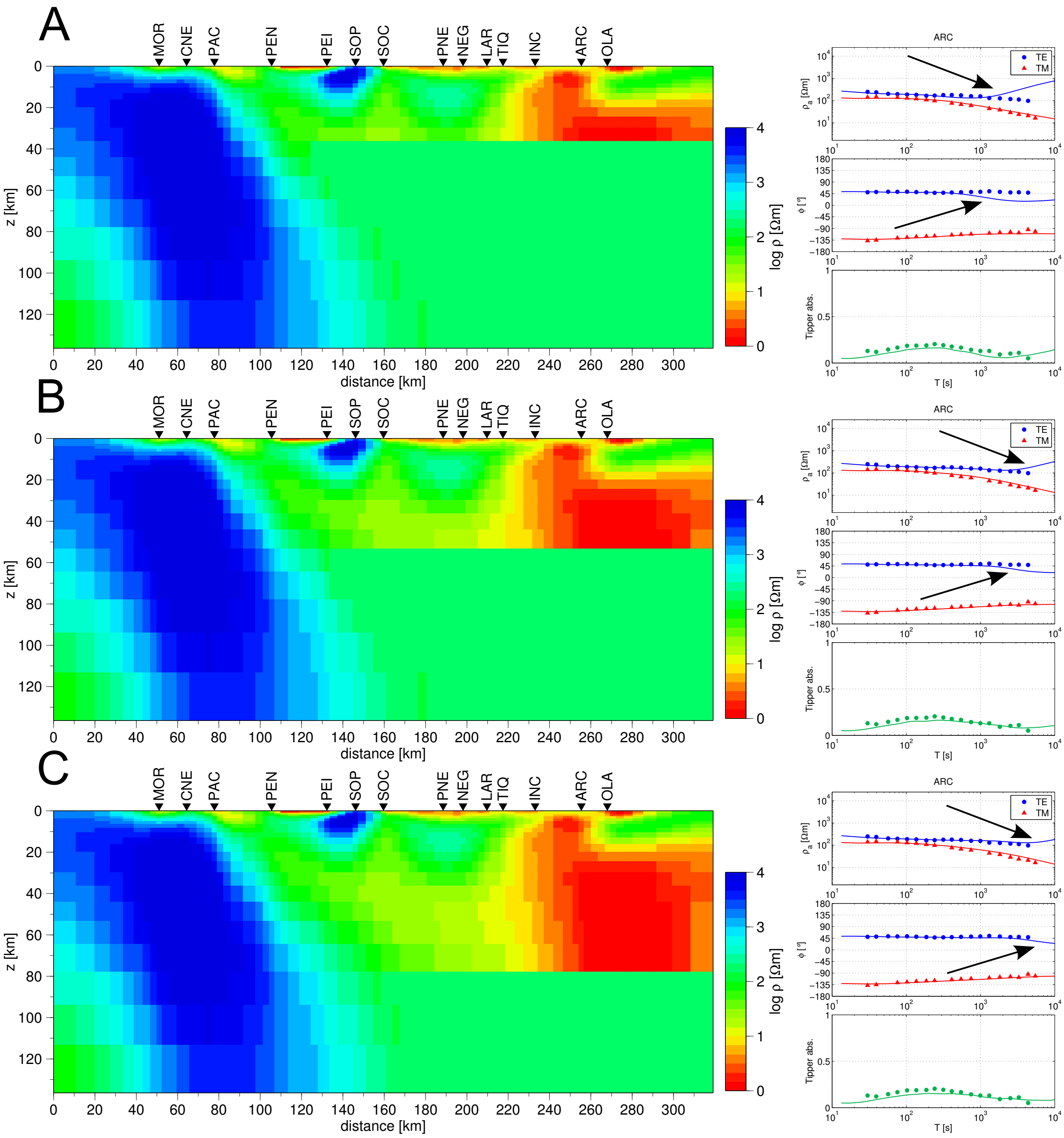

Figure 5.7: Comparison between measured data (dots) and model responses (lines) for station ARC, located in the Argentinian Puna, for a forward model based on the 2D inversion result shown in figure 5.4 B, with the bottom of the highly conductive zone below the Puna set at (A) 35 km , (B) 55 km and (C) 80 km

The result shown in figure 5.7 for station ARC is analogue to those obtained for stations INC and OLA, placed also in the Argentinian Puna. The change of the lower edge of the conductive zone affects especially the TE mode of these stations for the longer periods, as indicate the black arrows in the previous figure. While for a conductive zone reaching only 35 km in depth the fit is clearly poor for the last decade, when this conductive zone reaches 60 km the differences are smaller but still clear. For a conductive zone extending until 85 km or more, the behavior of the TE mode also seems to escape from the trend observed in the measured data, but only for the largest periods. For periods larger than 7000 s, the measured data in the stations above the anomaly have low quality and therefore were not considered for the inversions or this analysis. Hence, the lower boundary of the highly conductive zone beneath the Puna obtained in the 2D inversion should extend at least until 60 km depth, and very likely until more than 80 km. Note, that the original structures appeared again after the inversion was started over again, and that the same results were observed using constrained inversions.

For the resistive block beneath the Precordillera, similar synthetic models were calculated in order to test its extension in depth, but changes in its vertical extension are strongly affecting the responses in apparent resistivity and phase of the westernmost stations (e.g. MOR, CNE and PAC), and therefore this feature seems to extend also through the Moho. Another explanation points to the presence of two resistive zones, one extending in the continental crust, above the other which is extending under the Moho. A comparison between the response of such a model and the measured data can be seen in the figure 5.8.

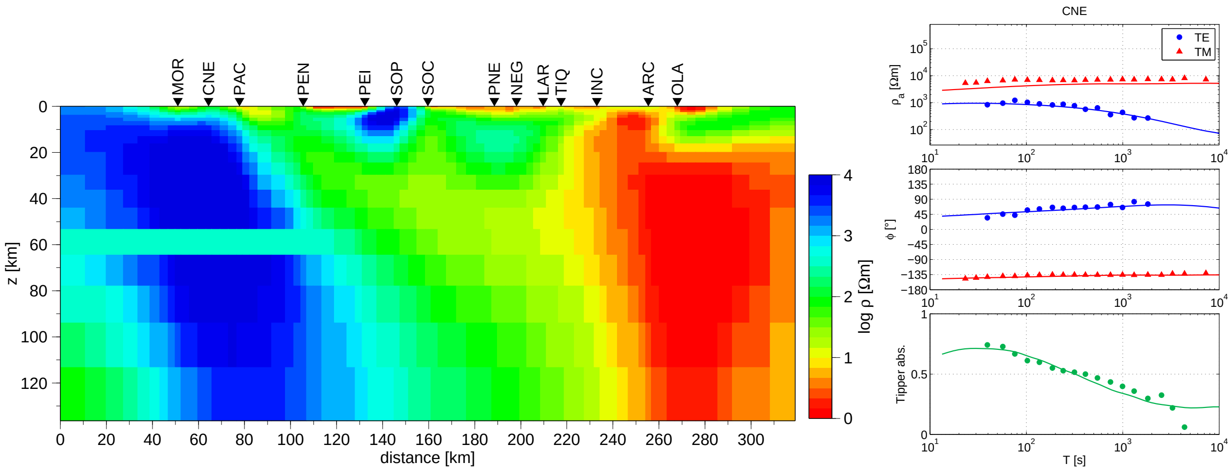

Figure 5.8: Comparison between measured data (dots) and model responses (lines) for station CNE, located in the Domeyko Cordillera, for a forward model based on the 2D inversion result shown in figure 5.4 B, with the highly resistive zone at the western border divided in two parts. Note the larger misfit observed for the TM curve compared with the response of the 2D inversion for the same station, shown in figure 5.5

Even when the apparent resistivity curve for the TM mode in the previous result is shifted with respect to the measured data, the tipper values and particularly the phases present a good fitting with the measured data and therefore, the idea of two different resistive zones producing this large anomaly in this part of the profile will be considered in the interpretation of this model.

The main features present in the 2D inversion are consistent with some of the major geological features in the area. The presence of a resistive zone in the western side of the Salar de Atacama basin and the good conductor representing this basin itself, a relatively conductive zone under the volcanic arc, and a larger and deeper highly conductive zone beneath the Puna is present in the data, and are not artifacts produced by the inversion process. All these features of the 2D inversion result will be analyzed and interpreted in the following chapter.

5.2 3D forward modeling

The 3D forward model calculation implemented in the WinGLink software package (version 2.20.02), uses the MT3FWD code written by Randy Mackie. Developed in 1999, MT3FWD is a program to compute magnetic and electric fields at the surface of a 3D electrical resistivity model illuminated by electromagnetic plane waves. It is a modified version of D3MTFWD2 released by Mackie and Madden in 1997. The MT 3D modeling algorithm uses the integral form of Maxwell's equations to derive a finite difference, second order approximation for the magnetic field. Non-divergence of the magnetic field is enforced by evaluating the magnetic and electric fields on grids that are staggered relative to one another. The resulting linear system is solved by preconditioned conjugate gradient relaxation. Convergence is considerably enhanced by explicit correction of residual failure of the non-divergence condition. The algorithm is discussed in Mackie et al. (1994).

The program assumes that 2D structure parallel to each edge continues uniformly to infinity in the direction normal to the edge. The tangential magnetic fields are assigned using 2D calculations for each edge. The edges parallel to the source magnetic field will have electric currents flowing normal to them and thus TE mode calculations are done. The edges perpendicular to the source magnetic field will have currents flowing parallel to them. In these cases, the tangential magnetic fields are zero. Relaxation is faster if a good estimate of the solution is provided at the start. The program interpolates the vertical boundary fields to form the initial guess in a way that the fields should already be a solution to the interior fields if the model is 2D rather than 3D.

3D forward modeling was performed with the AMT data obtained for the closest sites around the Lascar volcano, trying to find the synthetic model which fits the best with the real data set that has been measured.

The first steps to develop a 3D forward model are related with the definition of the grid in 3D. The parameters that control the size of the grid and each cell of the grid are the following:
- Determination of the area of interest and the horizontal cell size (500m x 500m).

- Determination of the initial rho value (100 Ωm).
- Number of air layers above the ground level (value used: 10).
- Determination of the vertical spacing, which is given by the vertical size of the first cell (100 m) and a vertical factor that controls how the cells are becoming larger with depth (value used: 1.35).
- Determination of the padding value, which indicates how are the cells growing horizontally, in the x and y directions (value used: 1,7).

Considering the previous values of cell size and padding factor the study area is discretized, with a central part of the grid just where a ring of AMT stations was placed around Lascar. From this central part, with approx. 20 x 20 km^2, the cells are becoming larger in the E-W and N-S directions, as can be seen in figure 5.9.

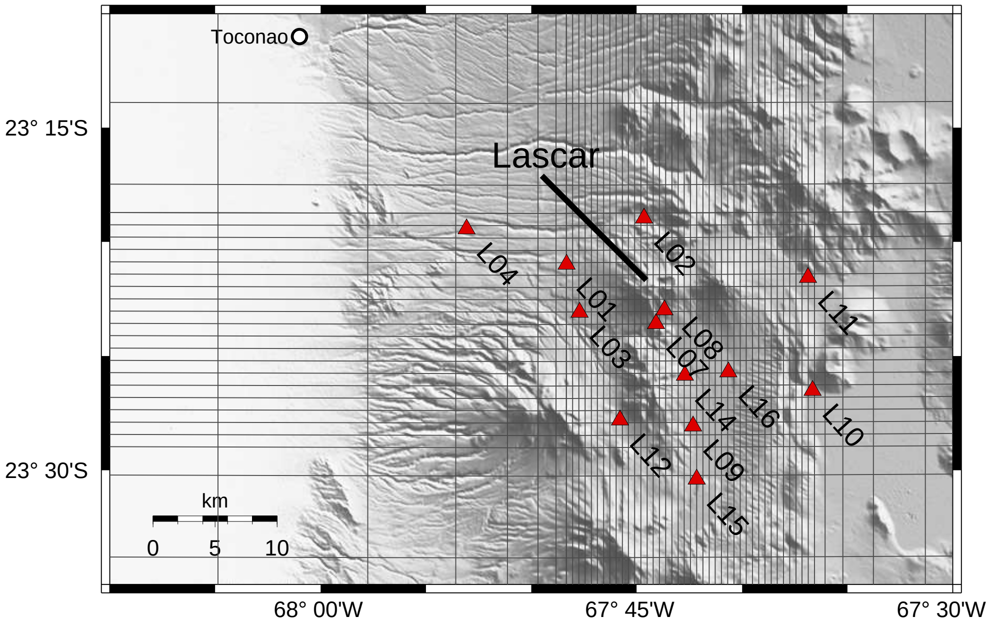

Figure 5.9: Discretization of the study area around Lascar, for the development of a 3D forward model. Central part of the grid (approx. 20 x 20 km^2) with a cell size of 500 m x 500 m in the horizontal directions and 100 m in depth for the first layer.

In the first stages of the 3D modeling, different scenarios were tested, in order to see the effect of the topography in the model responses and the hypothetical presence of a magma chamber.

5.2.1 The effect of different scenarios around a measuring point

The effect of 1D or 2D scenarios in magnetotellurics was shown in the *Data processing and analysis* chapter. The following examples illustrate the behavior of the magnetotelluric response in presence of some simple cases of 3D inhomogeneities, analyzing the behavior of apparent resistivity, phase and induction vectors.

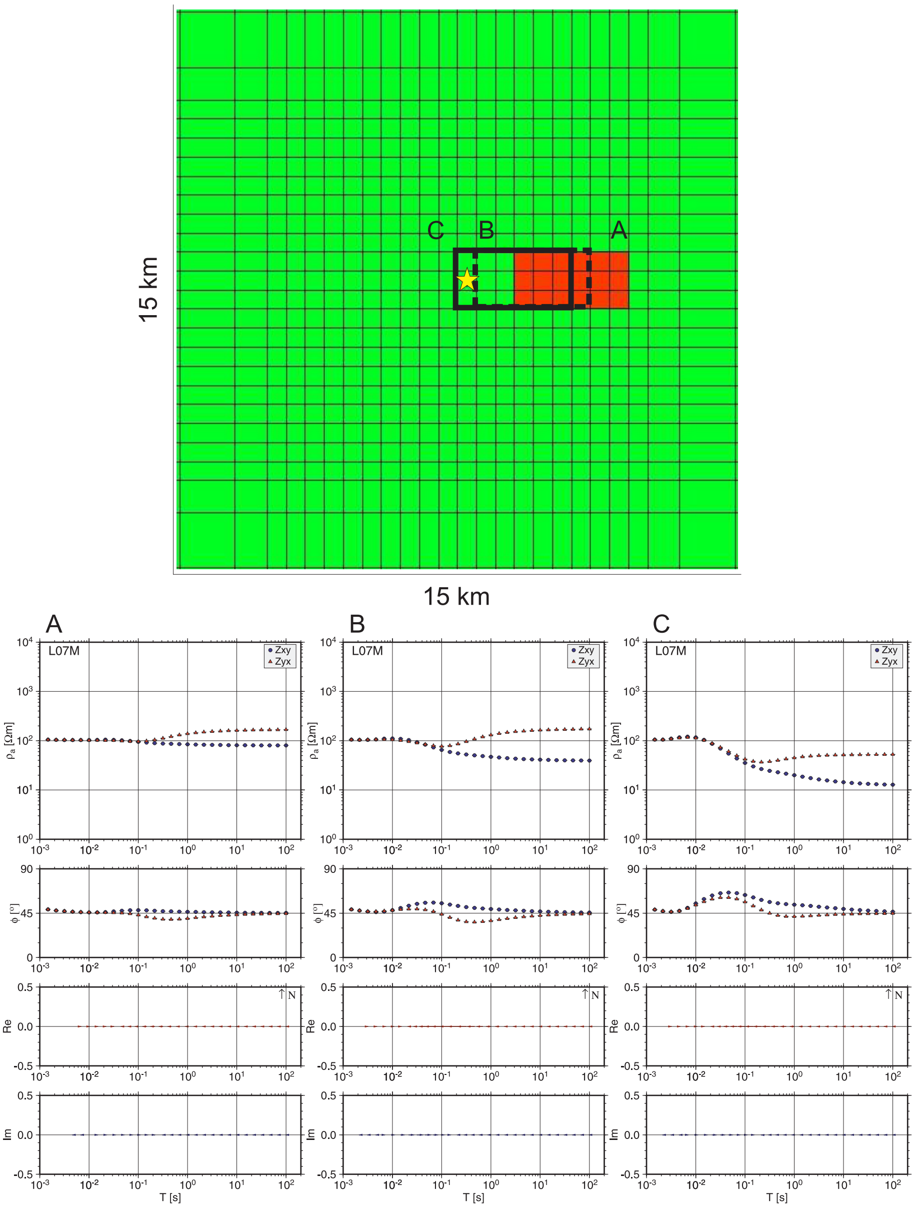

Figure 5.10: Effect of a conductive anomaly with distance. Conductive block of 1.5 km x 3 km x 1 km and resistivity of 1 Ωm, placed between 500 and 1500 m depth. Results according to the positions shown in A, B and C. Yellow star represents the measuring site. Induction vectors are small and point E-W; therefore they are badly visible.

The grid used for these tests has a smallest cell size of 500 m x 500 m in the horizontal directions, and 100 m in the vertical direction in the central part of the grid, and becoming gradually larger outside this central part and with depth. The first test shown here (fig. 5.10) deals with the effect of distance between the measuring point and an anomaly.

The effect of an anomaly closer to the station can be clearly noticed in the previous figure, as the fields induced by the anomaly are stronger as closer to the station they are. The same happens when the same anomaly is placed not between 500 m and 1500 m depth, but between 2000 m and 3000 m, as the presence of such an anomaly at those depths becomes slightly detectable analyzing the same parameters.

Now, the effect of the relative position between station and anomaly will be analyzed.

The results shown in figure 5.11 give a clear example of how important is the relative position between the anomaly and the measuring point. Comparing situations A and B, one may notice exactly the same behavior in the apparent resistivities and phases, but with one very important exception: The xy and yx components are exchanged, which can be explained regarding the rotational symmetry of this situation, analogous to a 90° rotation of the impedance tensor. Therefore, the induction vectors, depending on the horizontal and vertical components of the magnetic field, are showing the same magnitude but in a perpendicular direction.

More interesting remarks can be inferred from situations B and C, as in this case the same conductive block is located to the N and S of the station. Analyzing the apparent resistivities and phases it is not possible to find any difference, because the magnitudes of the different components of the electric and magnetic field observed in the station are the same, but with the opposite directions, and therefore obtaining the same impedance tensor. A clear difference can only be found analyzing the induction vectors, which are showing the same magnitudes but opposite directions, obtained by the opposite signs of the vertical magnetic field components in cases B and C. Situation D is also a special case, because if one only takes into account the apparent resistivities and phases, and due to the symmetry of the modeled block, it seems like the result of a 1D situation, as the curves of apparent resistivities and phases for both polarization modes shown here, are behaving in the same way for every period. Again the induction vectors are giving an important hint, indicating an increase in conductivity to the SE of the station, and therefore discarding the 1D case.

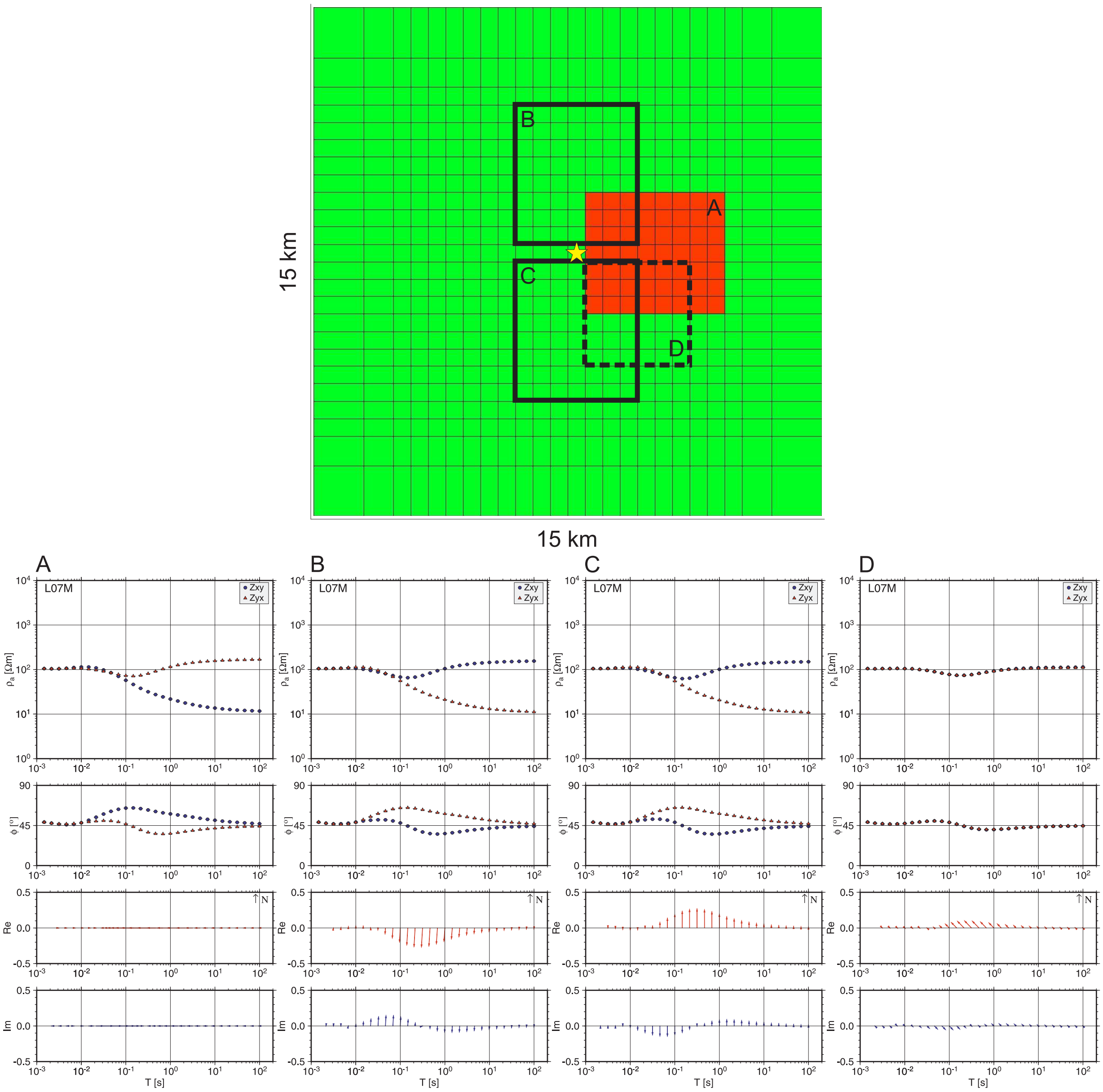

Figure 5.11: Effect of the relative position between anomaly and station. Conductive block of approx. 4 km x 4 km x 1 km and resistivity of 1 Ωm, placed between 500 and 1500 m depth. Results according to the positions shown in A, B, C and D. Yellow star represents the measuring site.

Another test consists of checking the effect of a conductive zone placed to the E of the measuring point and extending until different depths, or presenting different resistivities. In case A of figure 5.12 the curves shown are the response of a conductive zone of 1 Ωm starting at 500 m depth and extending until 1500 m. The effect observed can be compared with the results of case B, in which the conductive zone of 1 Ωm is extending until 10 km depth, becoming clear that this change in the extent of the conductive zone can be much more clearly noticed in one component of the impedance tensor (yx in this case) than in the other (xy in this case). Comparing now cases B and C, in which the conductive zone is the same as in case B, but with a resistivity of 10 Ωm, the other component (xy in this case) is now exposing more clearly the differences of both cases. If such anomalies were placed at larger depths, the comparison would be much more difficult, as the differences of the obtained results would be much slighter, due to the continuous loss of resolution when increasing depth.

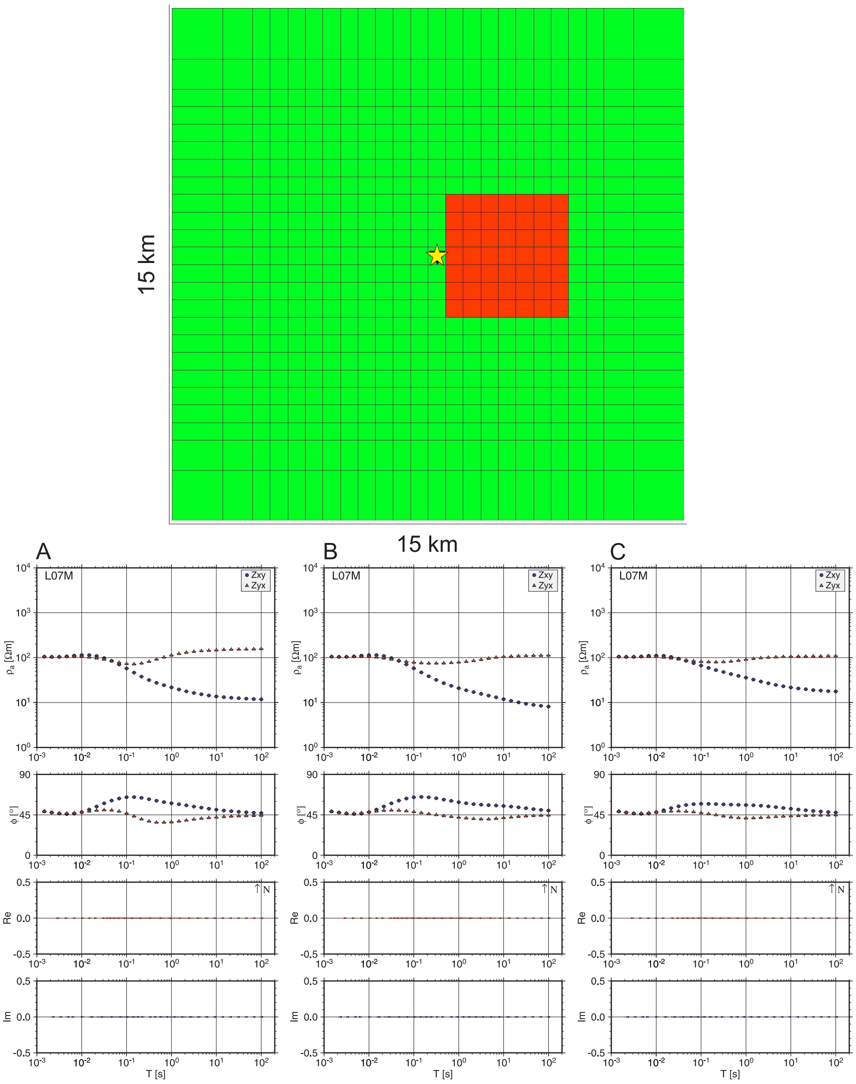

Figure 5.12: Effect of a different depth extension and resistivity contrast. Conductive block of approx. 4 km x 4 km horizontal area. Case (A) resistivity of 1 Ωm, placed between 500 and 1500 m depth, case (B) resistivity of 1 Ωm, placed between 500 and 10000 m depth, and case (C) resistivity of 10 Ωm, placed between 500 and 10000 m depth. Yellow star represents the measuring site.

5.2.2 Topographic effect

For a real consideration of the topographic effect in magnetotelluric measurements in this region, a 3D model was developed considering that everything below the surface has the same resistivity (100 Ωm), so the only parameter which can influence the measurements is the topography. This was done considering the same measurement points in which the real data was measured.

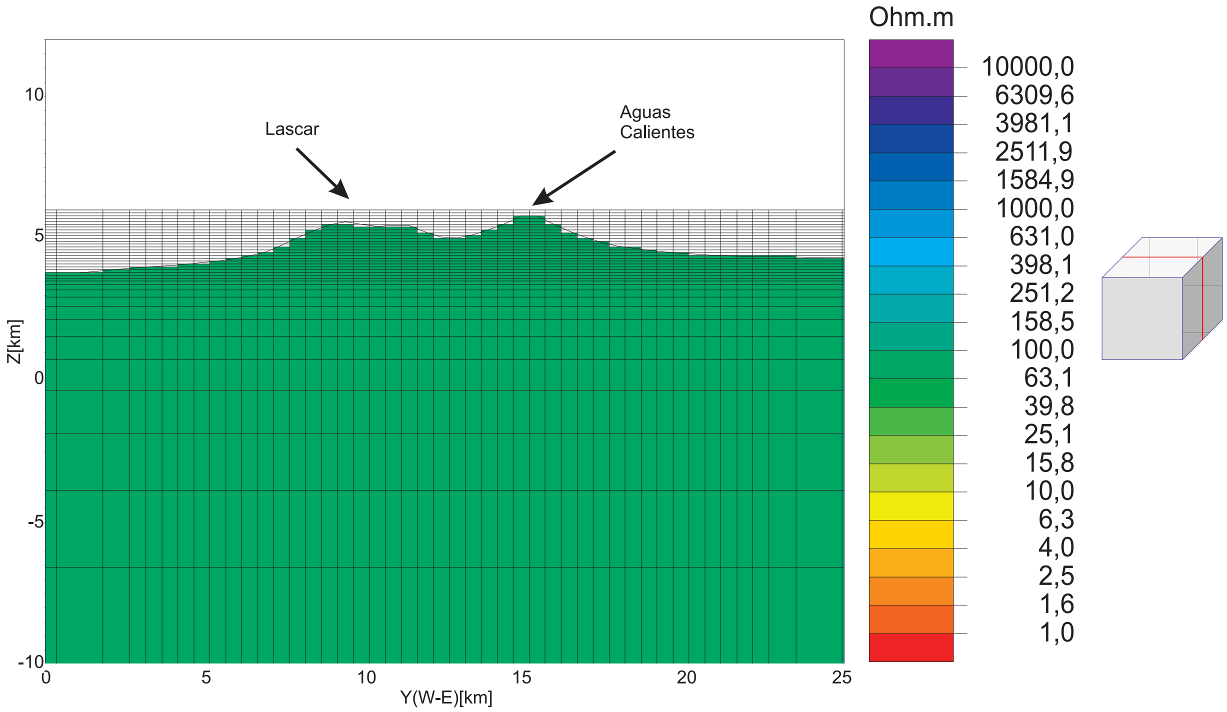

Figure 5.13: 3D model for the topographic effect estimation. View from the south, Lascar and Aguas Calientes volcanoes.

With this model considering a half-space of 100 Ωm, the effect of the topography for some of the sites for apparent resistivity, phase and induction vectors can be compared with the measured data, as shown in figure 5.14.

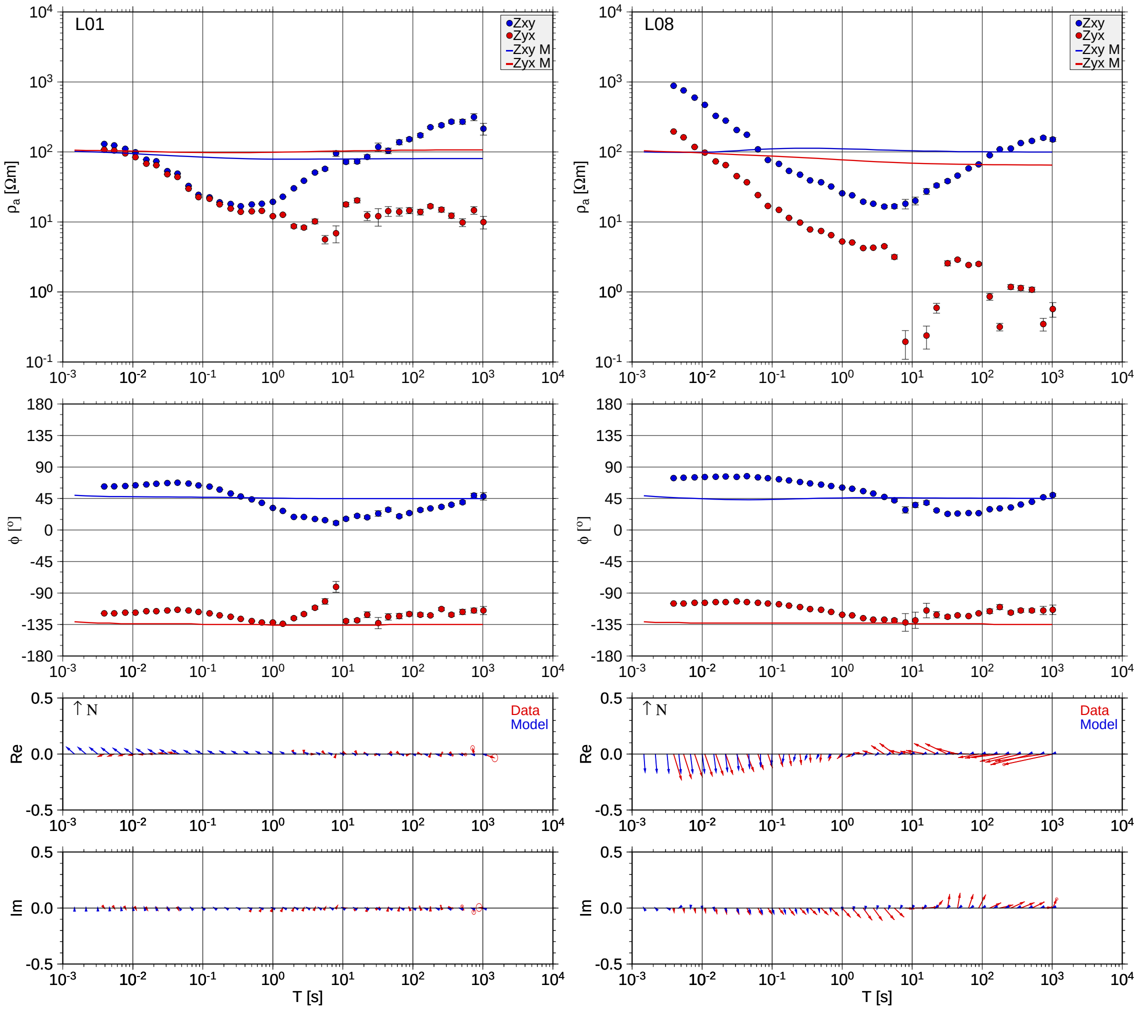

Figure 5.14: Real data and topographic effect shown as apparent resistivity curves, phase curves and induction vectors for sites L01 and L08. For the curves, dotted lines are real data and continuous lines are modeled data. Cell size of the central part of the model is 500 m x 500 m x 100 m.

These two sites where chosen to represent the behavior of the topographic effect in sites placed at different distances from the volcanic edifice, as L08 is located at the south-eastern slope, and L01 is placed at ∼4 km to the west of it. For these sites and also the others, the induction vectors point away from the main topographic highs, as they are conductive bodies compared with the air. This can be shown particularly for site L08, in which the induction vectors obtained from the model are stronger than in the other sites, because of its closer position to Lascar volcano, and are showing the same trend as the measured data for the shorter periods until almost 1 s. It can be seen also an effect in the apparent resistivity curves, which for periods larger than 10^{-1} or 10^{-2} s, start to distance from the real value of 100 Ωm, going up or down some tens of Ωm depending on the position and the proximity to the main highs.

Due to the memory capacity of the computer in which these models were made, the smallest cell size, in the central part of the model, was 500 m in the E-W and N-S directions, and 100 m in depth. A second model was made, reducing the cell size to 100 m x 100 m x 100 m in the central part of the model, but also the size of the central part was reduced, considering only the Lascar volcano area with a small cell size. Smaller cell sizes were not possible to achieve with the memory capacity of a currently normal computer (2 GB). Figure 5.15 presents the results of this model for the same stations shown previously in figure 5.14.

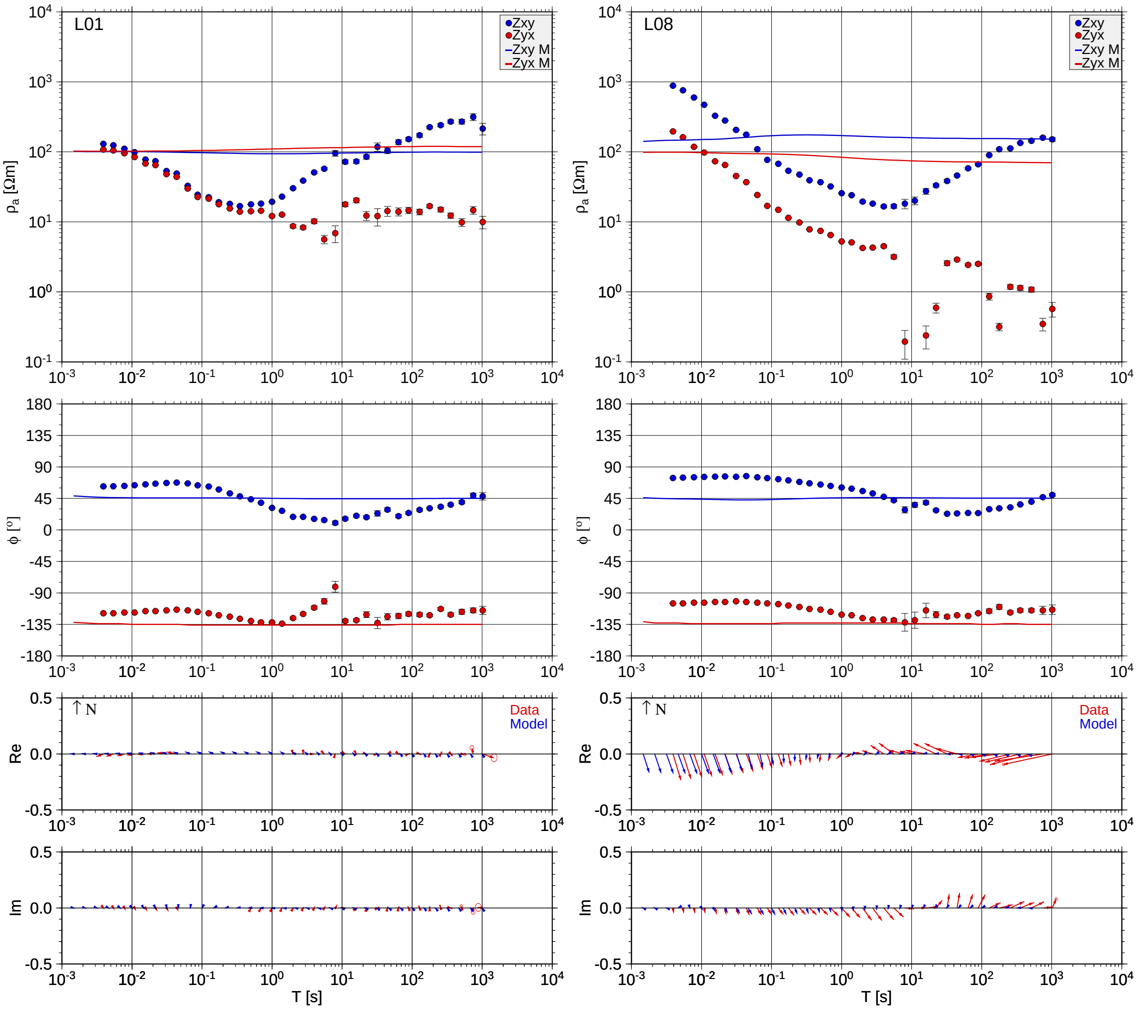

Figure 5.15: Real data and topographic effect shown as apparent resistivity curves, phase curves and induction vectors for sites L01 and L08. For the curves, dotted lines are measured data and continuous lines are modeled data. Cell size of the central part of the model is 100 m x 100 m x 100 m. Note that, as in the previous case, model responses have not much similarity with data, so additional structures are necessary

A finer grid can represent better the topography of this region, and therefore is giving a better estimation of the influence of this topography in the measured data. This can be observed particularly for the induction vectors in site L08, which are showing a slightly better fitting than in the previous results using a larger cell size. Even when a smaller cell size gives slightly better results, the use of this cell size leads to the use of a smaller central part of the grid (due to computer capacity restrictions) giving more influence to Lascar volcano and subtracting it from other topographic highs in the zone, which are closer to other stations.

Hence, it is possible to infer from the previous results that the topographic effect plays a stronger role for the sites very close to the topographic highs, for example site L08, but even in this case its influence is not enough to explain the behavior of the apparent resistivities, phases and induction vectors for periods larger than 1 s.

5.2.3 Modeling the conductivity structure beneath the volcano

From the first analysis of the AMT data measured around Lascar volcano, it becomes clear that some conductive heterogeneities are needed in the model beneath the vicinity of the volcano, in order to fit the measured data. The shape, extension and resistivity of these bodies will be restricted comparing in every case the response of these models, with the measured apparent resistivities, phases and induction vectors.

Some features were added to the starting model, in order to include some important characteristics of the study zone. The Salar de Atacama basin was set as a very conductive zone (1 Ωm) reaching depths of $\sim$1 km. Some kilometers beneath the Salar de Atacama, a resistive block was placed (1000 Ωm), extending between 10 and 60 km beneath the surface, emulating the presence of the Atacama Block (Schurr and Rietbrock, 2004). However, these features prove to be not really essential after some tests, as they are located relatively far from the volcano and most of the stations, and therefore not included in the last tests.

No difference in conductivity between crust and mantle was assumed in these models, as no clear difference have been seen in the LMT inversions. The first attempts were focused on determining the presence of a conductive zone beneath the volcanic edifice. One of these first attempts is presented in figure 5.16.

Checking the fit of the first forward modeling attempts (as in figure 5.17) in which just one conductive block was placed directly under the volcano, it seems clear that such a feature can not explain the observed data, at least not by itself, but this could be because of the particular shape, extension or resistivity present in these models. Therefore, several models including conductive zones beneath the volcano at different depths, with different sizes, shapes and resistivities were tested (e.g. figure 5.18), obtaining in all the cases a very poor fit.

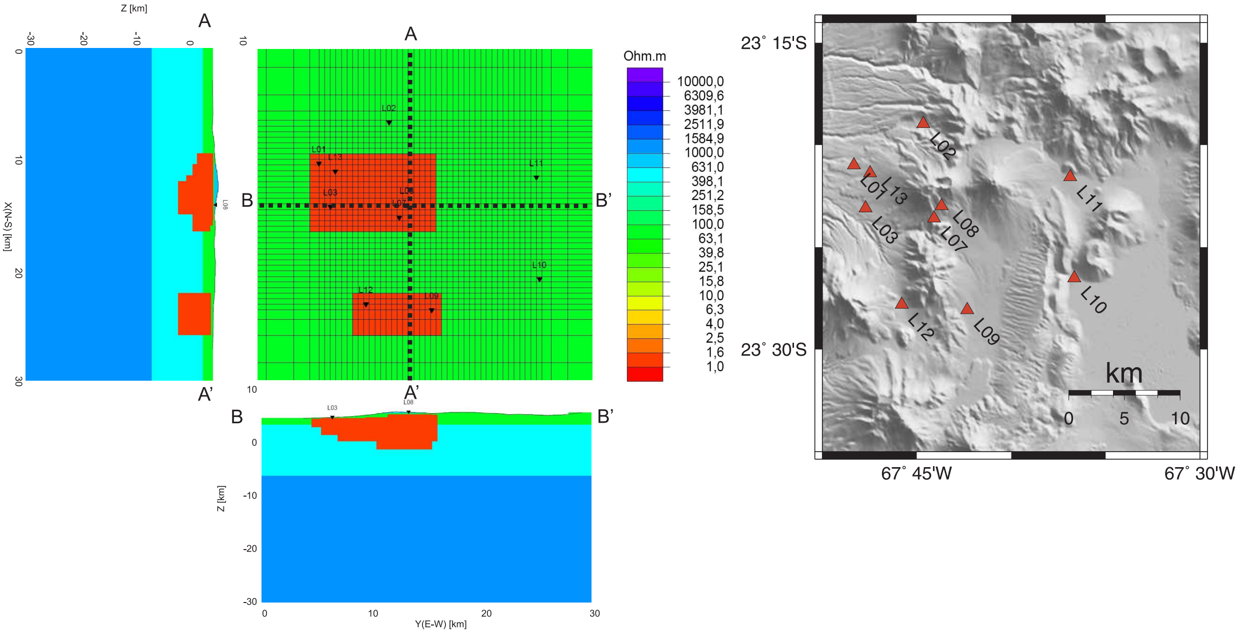

Figure 5.16: 3D model including a main conductive zone below Lascar volcano.

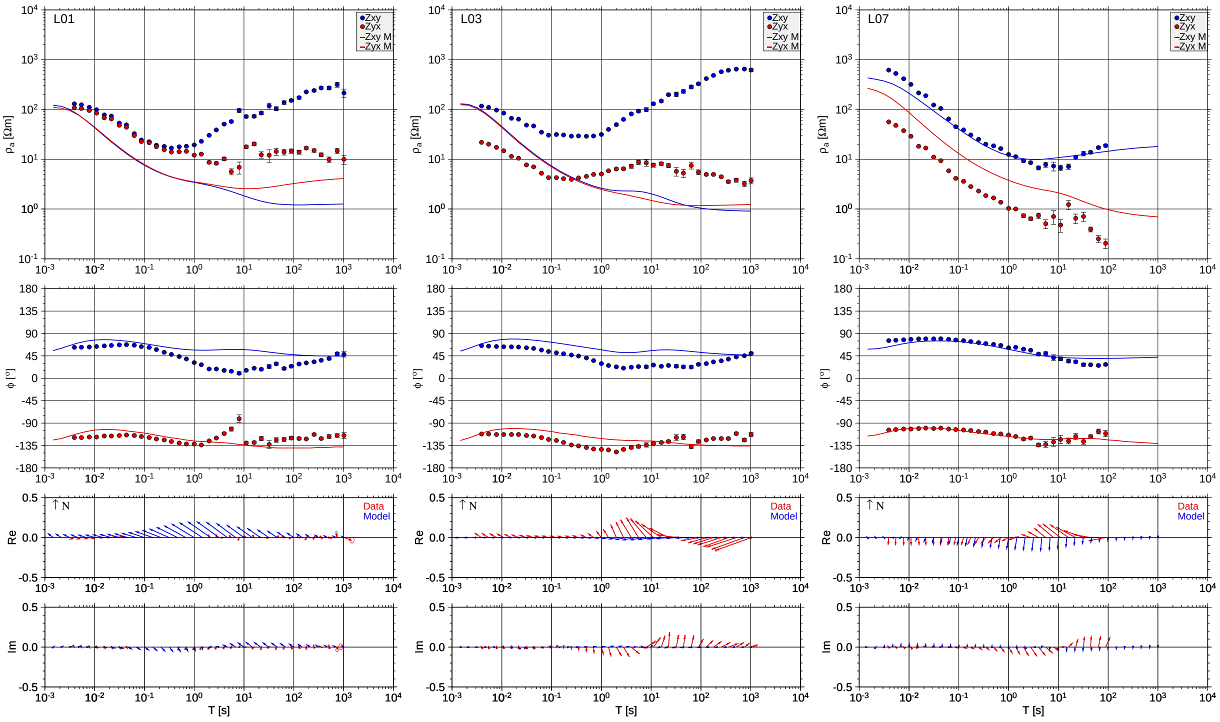

Figure 5.17: Comparison between measured data and model response for 3 sites around Lascar for the model shown in figure 5.16. Continuous lines and blue arrows represent the modeled data.

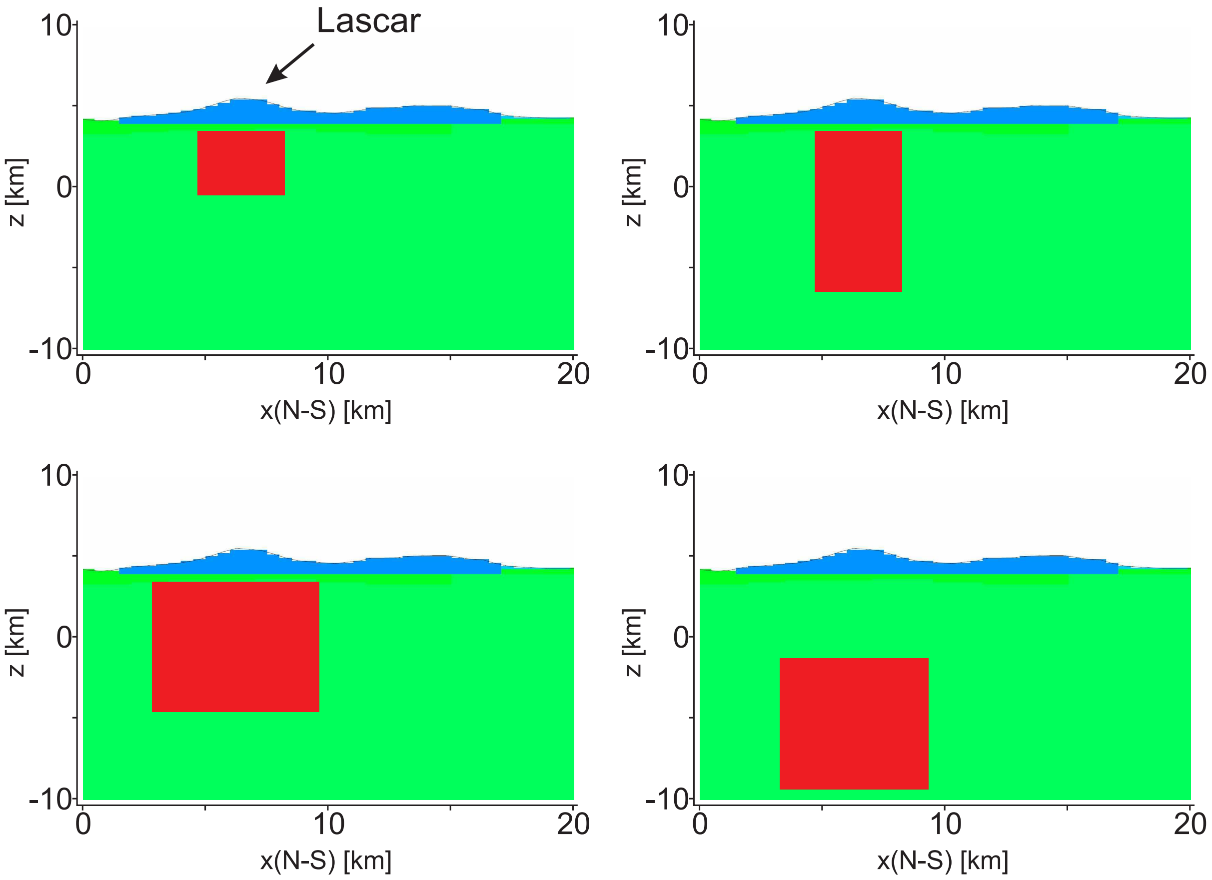

Figure 5.18: Examples of different modeling attempts with a unique conductive zone beneath the volcano. In these examples the red zones are representing a resistivity of 1 Ωm, green of 100 Ωm and blue of 800 Ωm.

A more complicated scenario is needed in order to fit the measured data all around the volcano. More than one highly conductive body in the proximity of the volcano is necessary, and now the question is related with the location, geometry and how conductive are these bodies in the subsurface. In order to find a solution to this problem, the phase tensor analysis could give some good hints, by analyzing the phase tensor ellipses calculated for the measured data, shown in the previous chapter.

One very interesting feature regarding the phase tensor ellipses, was shown in figure 4.14. For periods between 1 s and 5 s, only the sites to the S-SE of the volcano show a high value of Φ_2, indicating an increase of conductivity with depth, which is not the case for the stations to the N or the W of the volcano. The value of Φ_2 continues decreasing with period, and for 8 s, only station 9 has a high value of Φ_2, and for 10 s all the stations show low values. For the same period range, the induction vectors are also indicating the presence of a conductive zone in the same place, as shown in figure 4.3.

Following this result, conductive zones not just under the volcano, but also to the S and/or SE were added to the 3D models to improve the fit. Another feature added to the 3D model, placed in the NW flank of the volcano, was a relatively conductive layer (10 Ωm) which extends between 300 and 600 meters below the surface. Several models were tested including these features, trying to define the shape and the depths of each zone, and how these changes influenced each station. In figure 5.19 it is shown one of these models, the fitting for 9 stations is shown in figure 5.21.

In figure 5.19 a good conductor was placed to the S of the volcano, reaching depths of $\sim$ 25 km. Several models were tested in order to determine the shape, extension and depth of this conductive zone, and how this changes affect the fitting between the modeled and real data. Models with one single conductive zone to the south of the volcano were tested, but the results for the southern stations (L07, L08, L09 and L12) were improved by the inclusion of 2 conductive zones, a smaller one directly to the south of the volcano beneath stations L07 and L08, and a second and larger one, which is located $\sim$5 km to the S of the first one. These two conductive zones may be connected at shallow depths, and the depth range for each of this conductive zones will be discussed later.

Another feature which was added during the modeling process was a resistive zone located to the W of site L04. This resistive zone, extending in depth until 6-7 km, can be related with a similar feature present in the 2D inversion for the LMT profile, and geologically can be explained by intrusive bodies seen in that zone in the Cuyuguas and Allana hills, related with the southern Cas and Peine formations (Breitkreuz and Zeil, 1994).

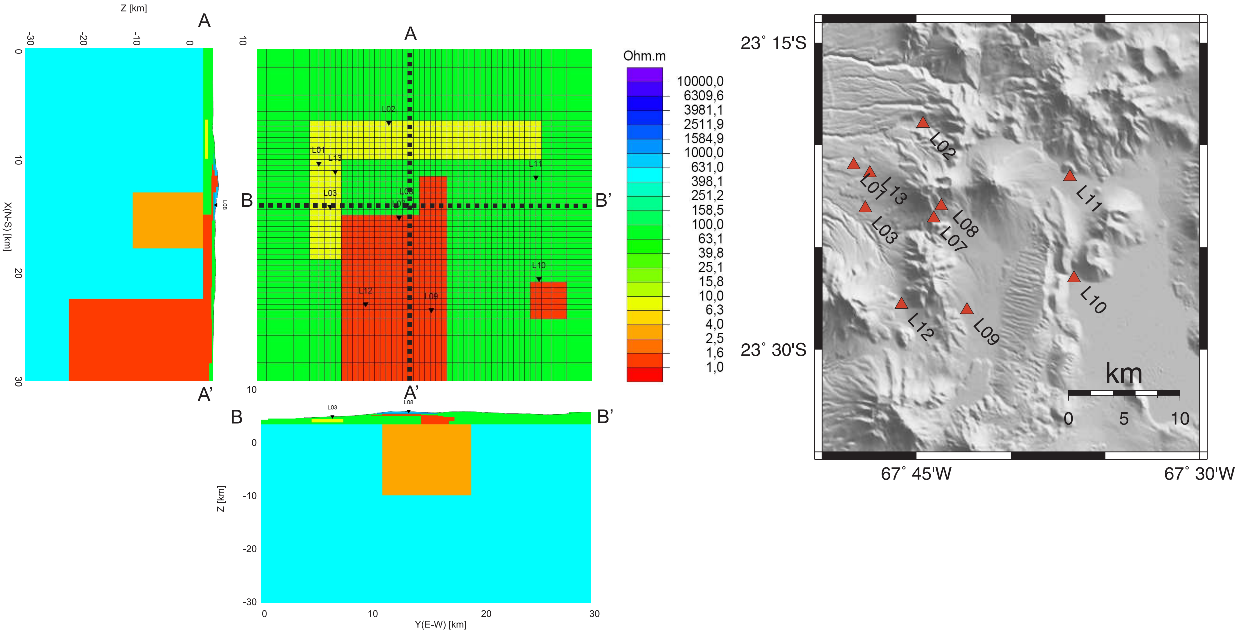

Figure 5.19: 3D model including a conductive zone extending to the S of Lascar. This model includes the Atacama Block and the Salar de Atacama, which are relatively far from the central part of the grid.

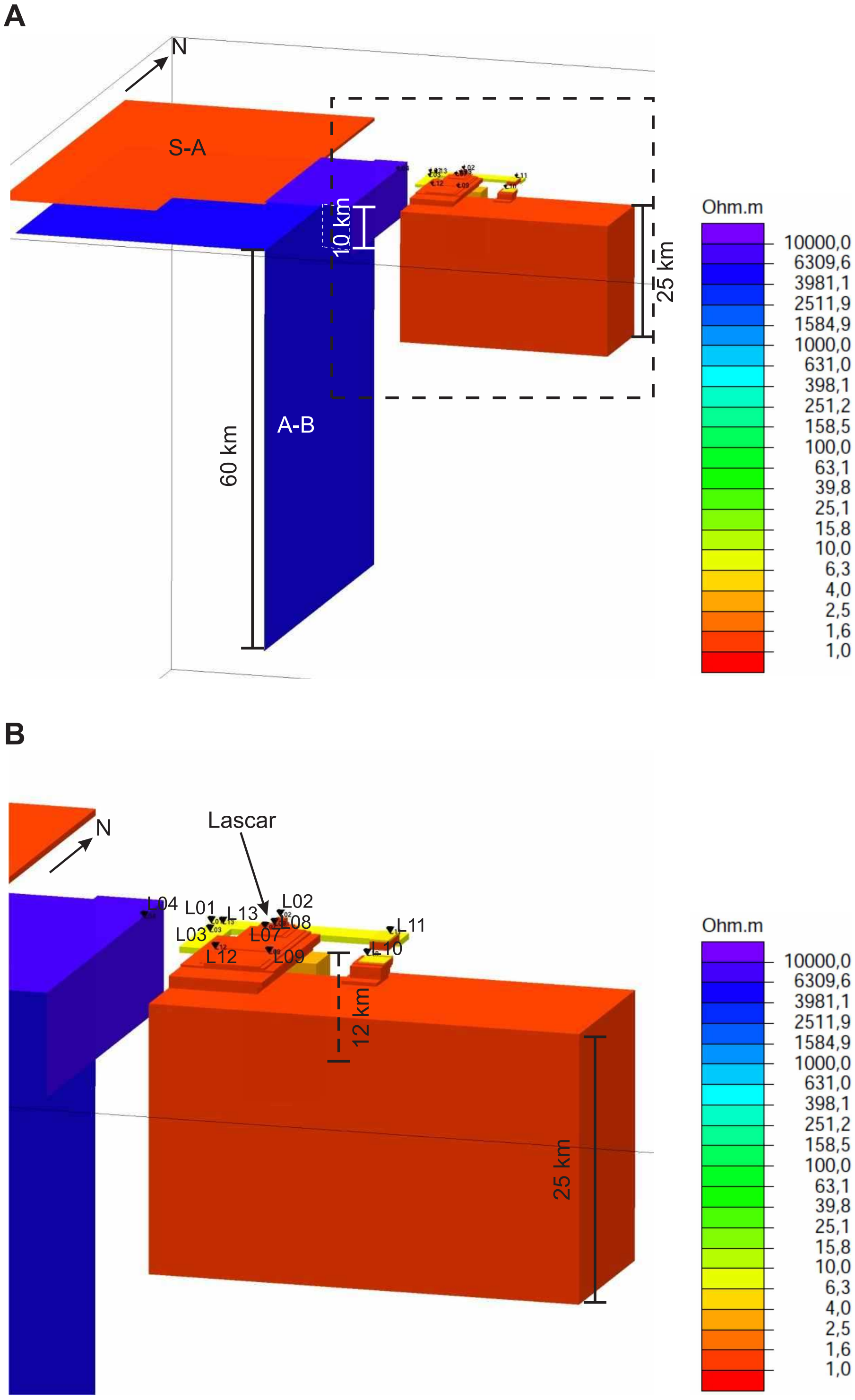

Figure 5.20: 3D view from the southeast of the model shown in figure 5.19. The segmented line in image A is marking the zone shown in image B. In this figure only the conductive zones (<30 Ωm) and resistive zones (> 1000 Ωm) are shown. A conductive zone of 1-5 Ωm to the southeast of the volcano is extending 12 km in depth close to it and 25 km in depth further to the south. S-A is the Salar de Atacama, modeled as a thin conductive zone of ∼1 Ωm. A-B is the Atacama block, modeled as a resistive zone starting at 5 km beneath the Salar de Atacama and extending 60 km in depth. No vertical exaggeration.

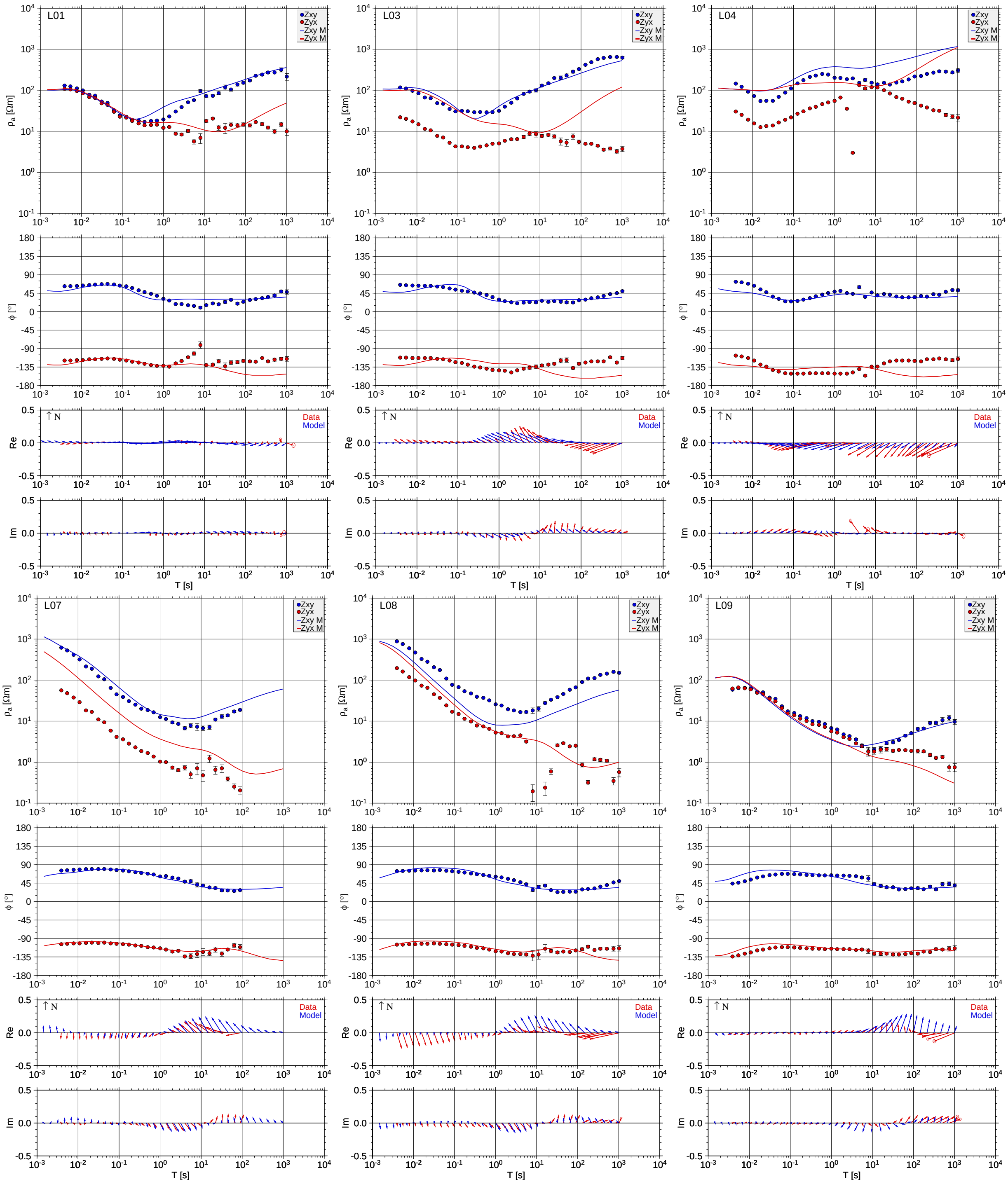
L01
L03
L04
L07
L08
L09
Zxy
Zyx
Zxy M
Zyx M
ρa [Ωm]
φ [°]
Re
Im
↑N
Data
Model
T [s]

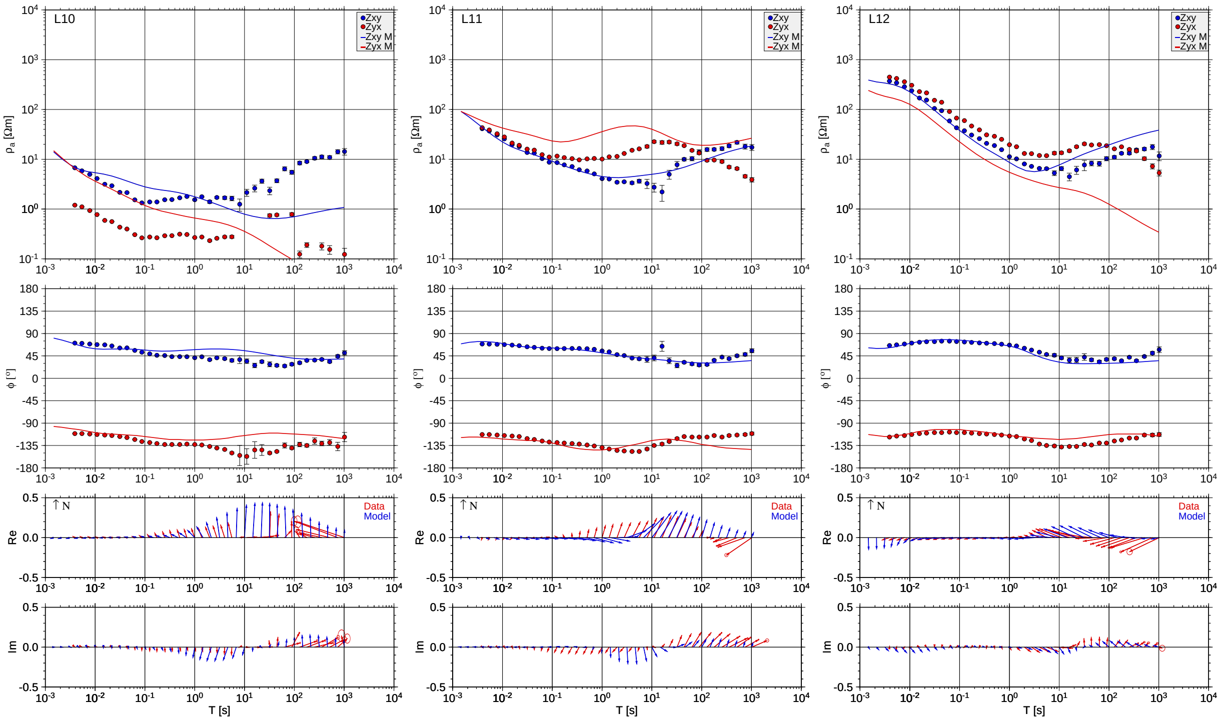

Figure 5.21: Comparison between measured data and the response of the model shown in figure 5.19 and for 9 sites around Lascar volcano. Main diagonal elements are not considered here as they are rather noisy and difficult to fit (comes from p. 78).

The first models included the Atacama Block, proposed by Schurr and Rietbrock (2004), but as it was already mentioned, its presence was not essential for the data fit, and therefore not included in the following tests.

In early 2010, 3 new AMT sites were measured around Lascar volcano (stations L14, L15 and L16), specifically in the southeastern side, achieving a better coverage in the area where a conductive zone was inferred by the forward models computed with the previously measured data. New models were calculated including these 3 new constraining points, obtaining models as the one depicted in figures 5.22, 5.23 and 5.24.

In this model the resistive block at the eastern border of the Salar de Atacama was also considered. The new data is also in good agreement with the models including a conductive zone extending to the southeast of the volcano, even when some small features were added to the model in order to improve the fit in the new stations. The new data available, particularly from site L15 is giving new hints indicating the presence of a conductive zone close to this station, as the induction vectors are much weaker in this station than in the other stations in the surroundings.

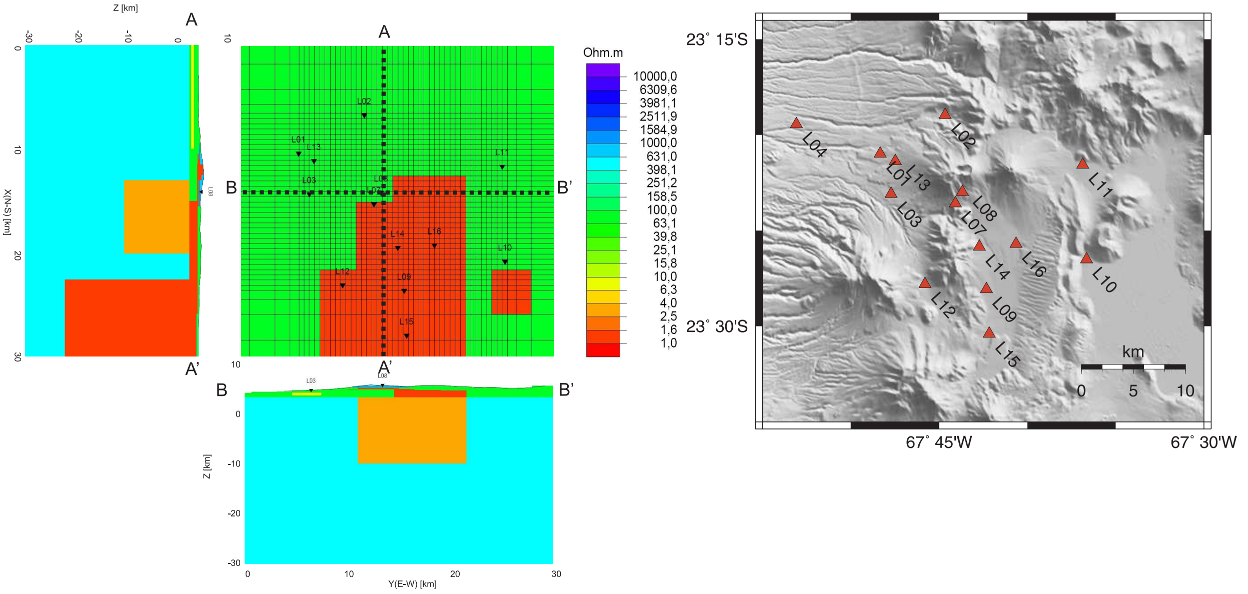

Figure 5.22: 3D model including a conductive zone extending to the S of Lascar. This model includes the data from 3 new stations measured in early 2010.

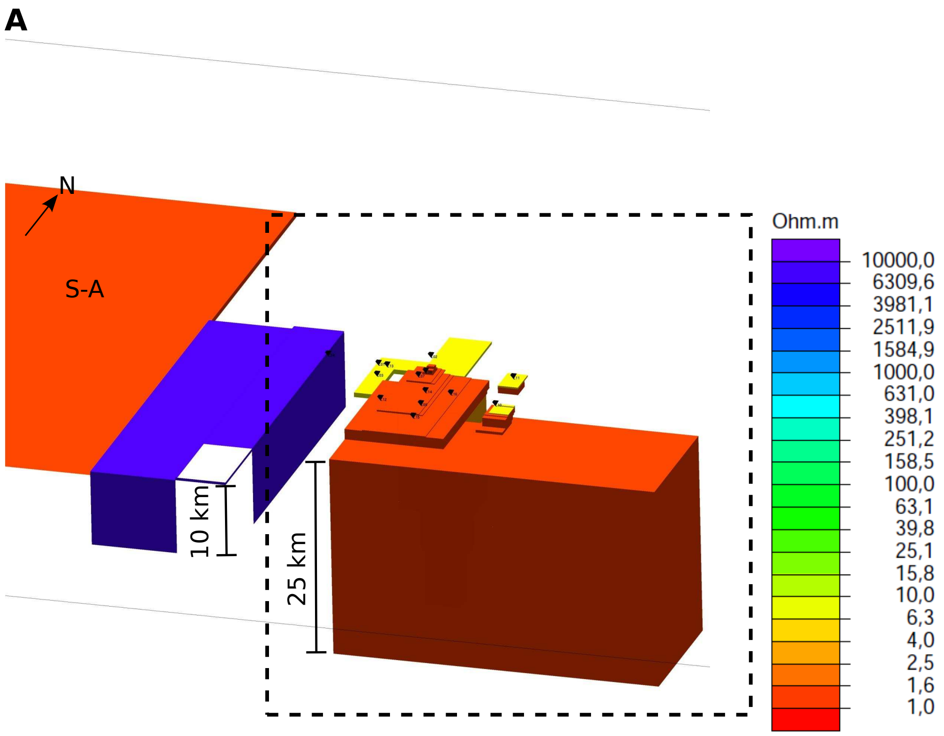

Figure 5.23: 3D view of the model shown in figure 5.22. The segmented line in this image is marking the zone shown in figure 5.24. In this figure only the conductive zones (<30 Ωm) and resistive zones (> 1000 Ωm) are shown. Note the presence of the resistive block at the eastern border of the Salar de Atacama reaching 10 km depth. The conductive zone of 1-5 Ωm to the southeast of the volcano is shown in detail in figure 5.24

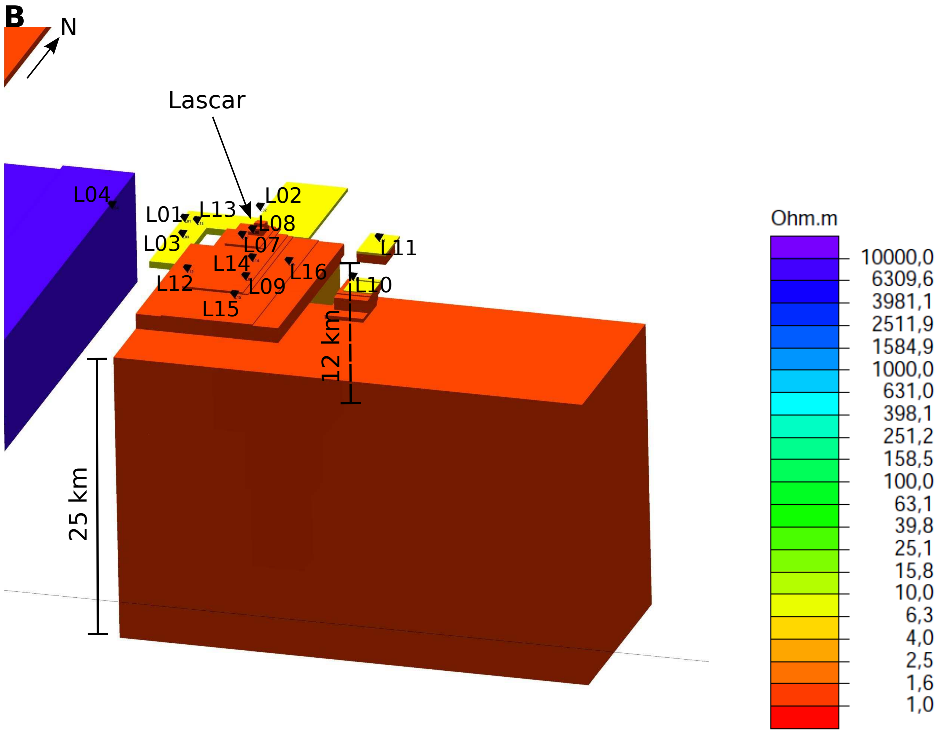

Figure 5.24: Detailed view of the model shown in figure 5.23. In this figure only the conductive zones (<30 Ωm) and resistive zones (> 1000 Ωm) are shown. A conductive zone of 1-5 Ωm to the southeast of the volcano is extending 12 km in depth close to it and 25 km further to the south. No vertical exaggeration.

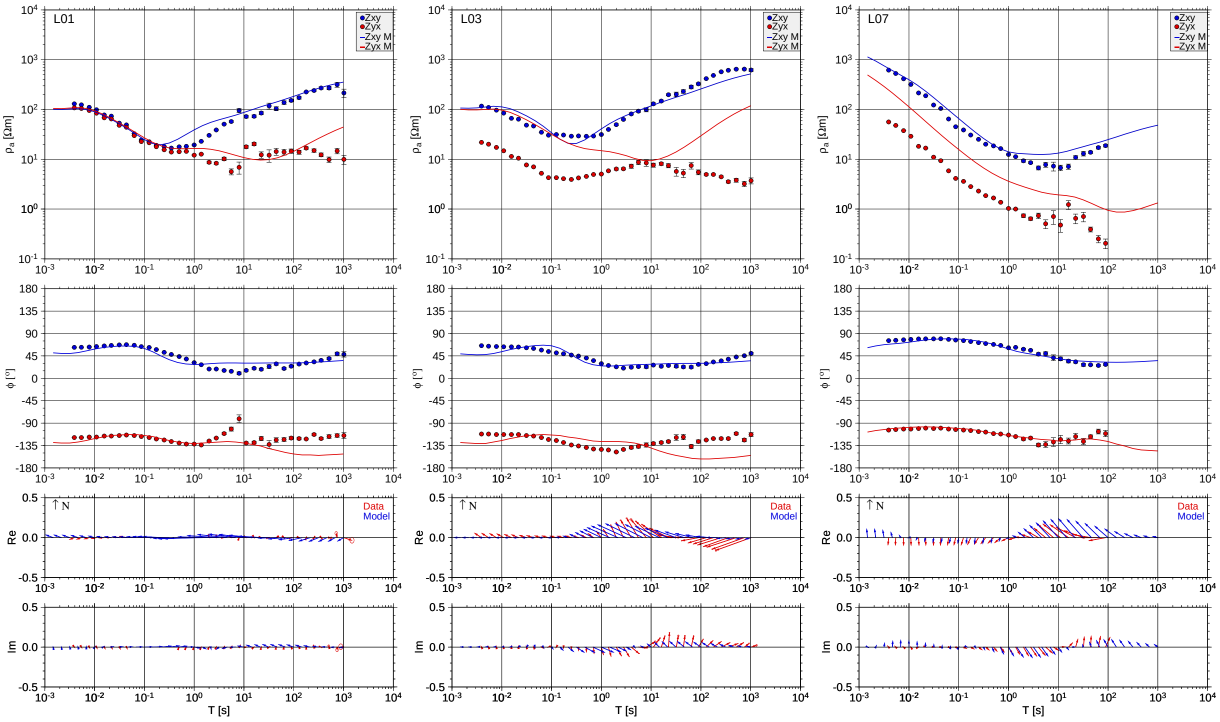

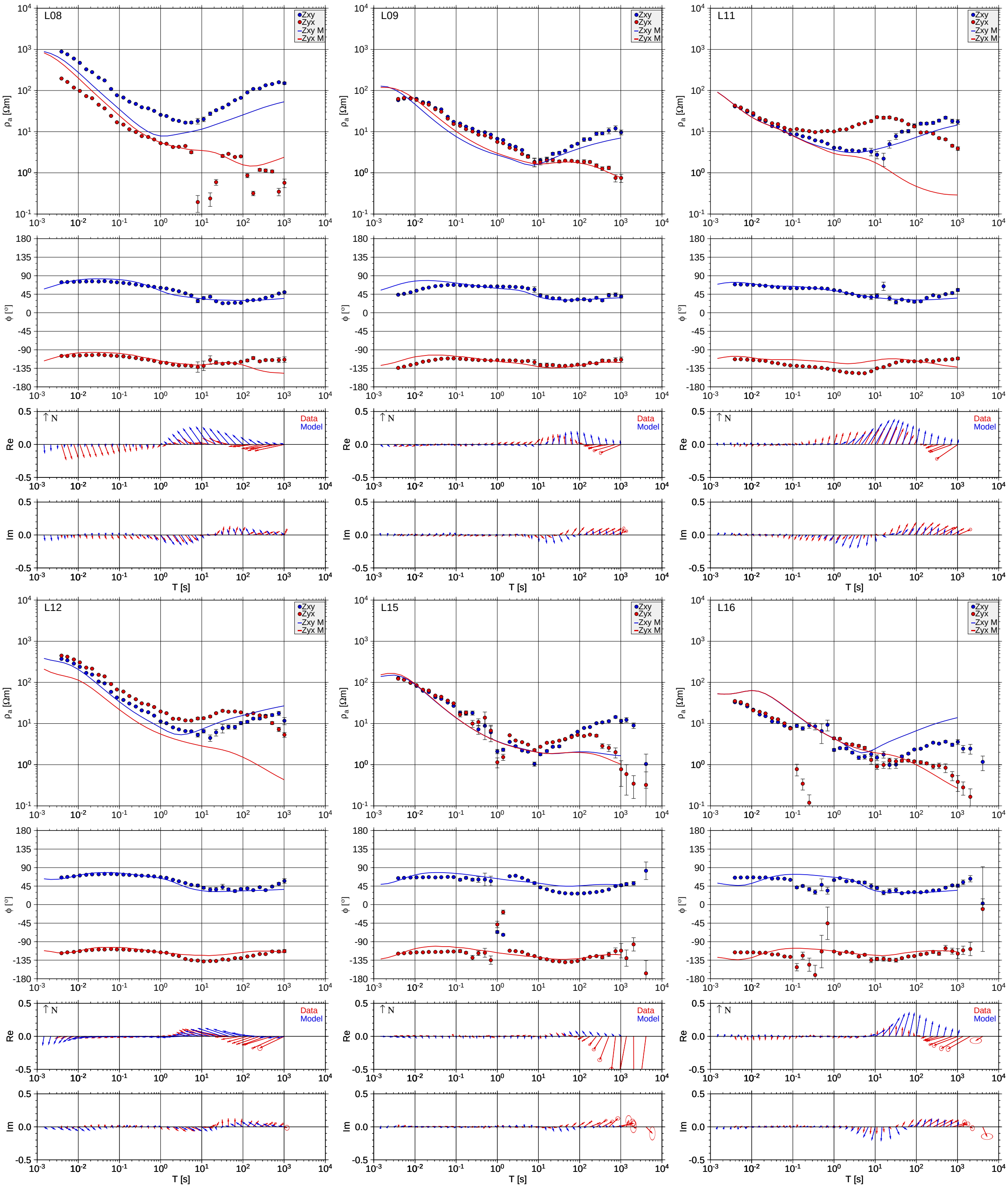

Figure 5.25: Comparison between measured data and the response of the model shown in figure 5.22 and 5.24 for 9 sites around Lascar volcano (comes from p. 81).

Another important feature included at this stage in the 3D forward models was related to the behavior of the induction vectors for periods between 100 - 1000 s, requiring the presence of a highly conductive zone to the E-NE and between 10 and 70 km depth, which can be seen in the model shown in figure 5.27. The horizontal extension of this highly conductive zone could not be completely defined, because of the relatively small size of the grid used for these 3D forward models, which is concentrated in the volcanic edifice and its surroundings. This feature should be related with the highly conductive zone obtained beneath the Puna in the 2D inversion results.

Several attempts were carried out in order to constrain the conductive zone to the S-SE of the volcano, and defining the minimum depth extension needed to fit the measured data. Models including a conductive zone reaching ∼6 km beneath the surface seem to be enough.

By the end of this work, more than 250 models were constructed in order to test different conductive or resistive features present in this area, being the model represented in figures 5.26 and 5.27 the best fitted (regarding all the stations around the volcano, and particularly induction vectors), and therefore considered as the resulting model of the 3D forward modeling with AMT data around Lascar volcano.

These results will be analyzed and compared with other geophysical and geological data obtained for this zone in chapter 6, in order to check the possible sources that could be producing conductive structures as the ones obtained for the best fitted models.

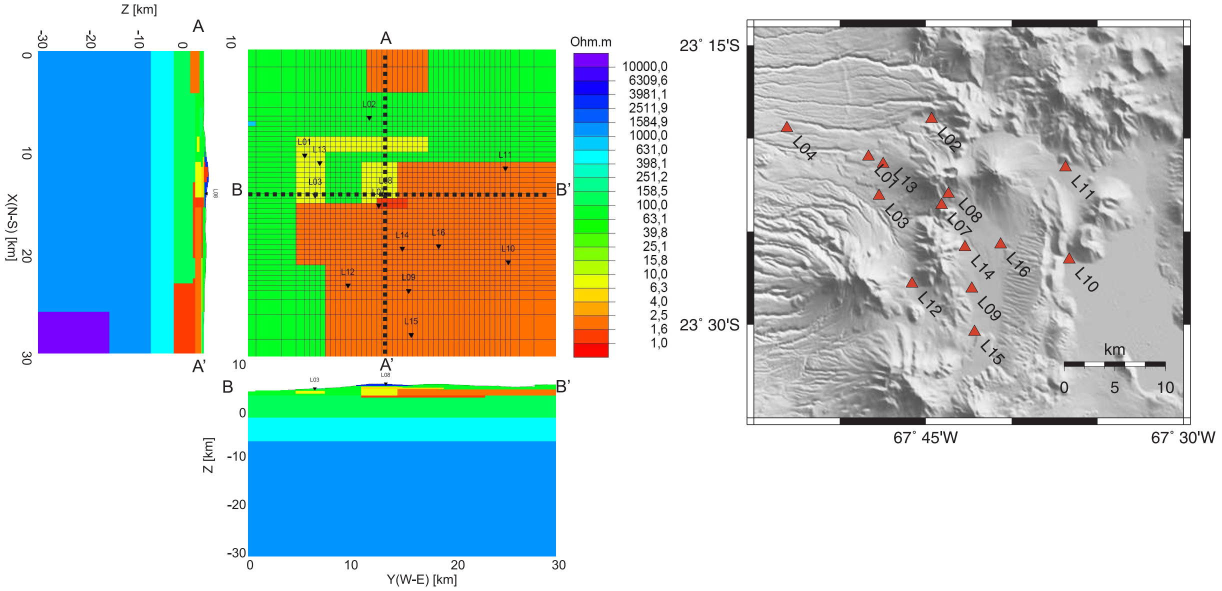

Figure 5.26: 3D model including a conductive zone extending to the S of Lascar, plain view at 2 km depth. Depth extension of the conductive structure reaching 6 km beneath the surface.

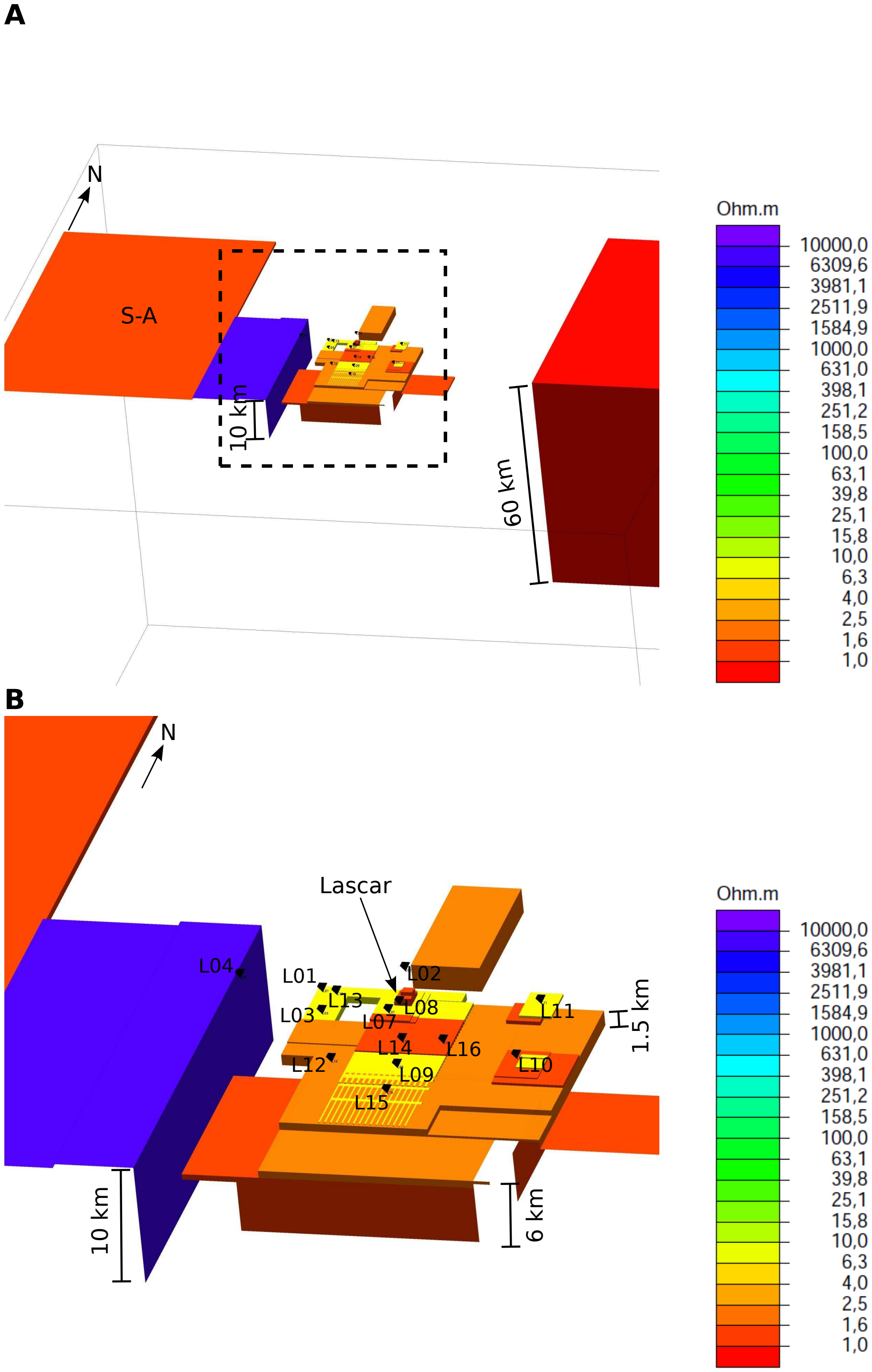

Figure 5.27: 3D view from the southeast of the model shown in figure 5.26. The segmented line in image A is marking the zone shown in image B. In this figure only the conductive zones (<30 Ωm) and resistive zones (> 1000 Ωm) are shown. A conductive zone of 1-5 Ωm to the southeast of the volcano is extending 1.5 km in depth close to it and 6 km further to the south. Another conductive zone of 1 Ωm to the east of the volcano is extending between 10 and 70 km depth. No vertical exaggeration.

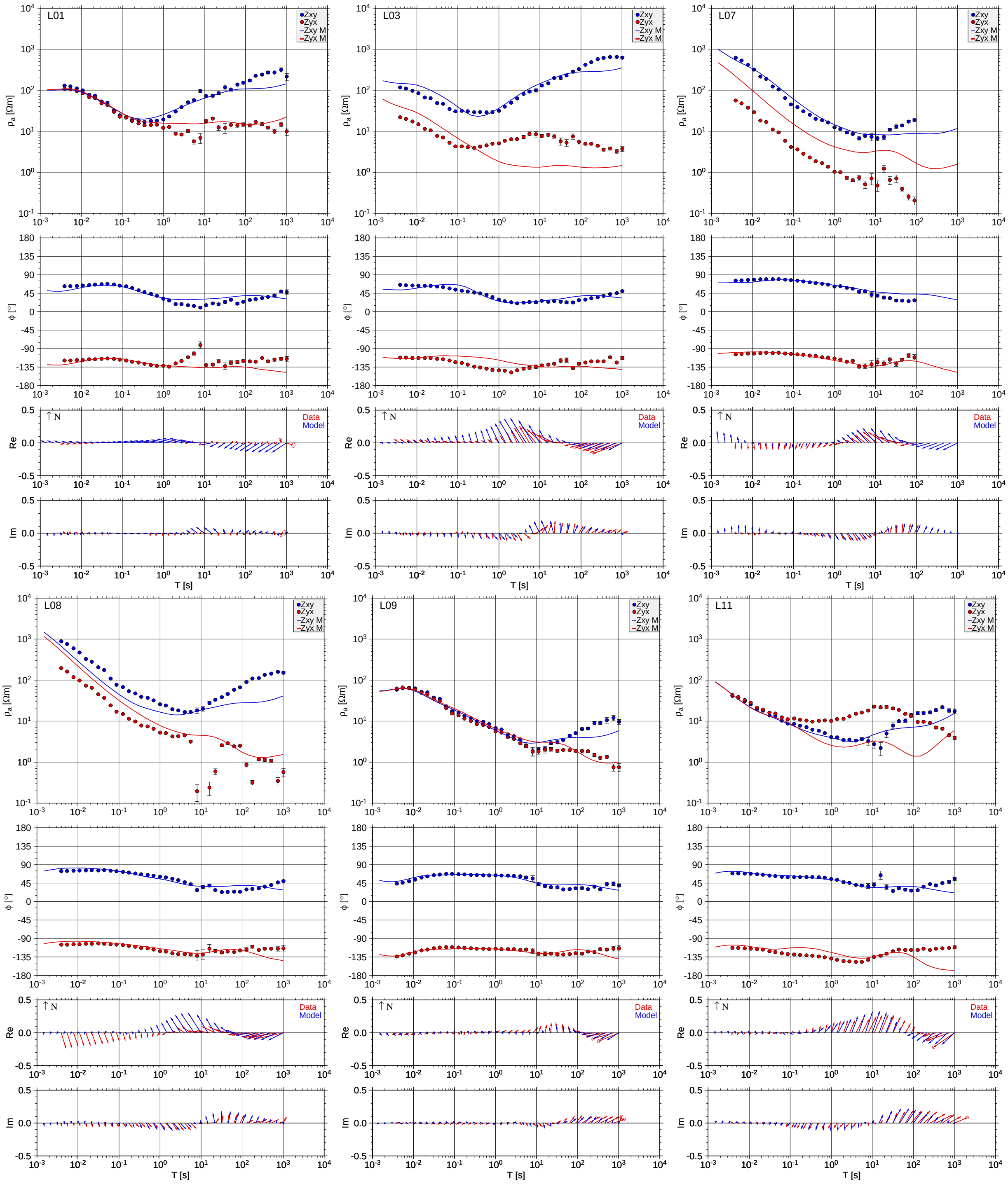
L01
L03
L07
L08
L09
L11
Zxy
Zyx
Zxy M
Zyx M
ρa [Ωm]
φ [°]
Re
Im
↑N
Data
Model
T [s]
10^{-1}
10^{0}
10^{1}
10^{2}
10^{3}
10^{4}
10^{-3}
10^{-2}
180
135
90
45
0
-45
-90
-135
-180
0.5
0.0
-0.5

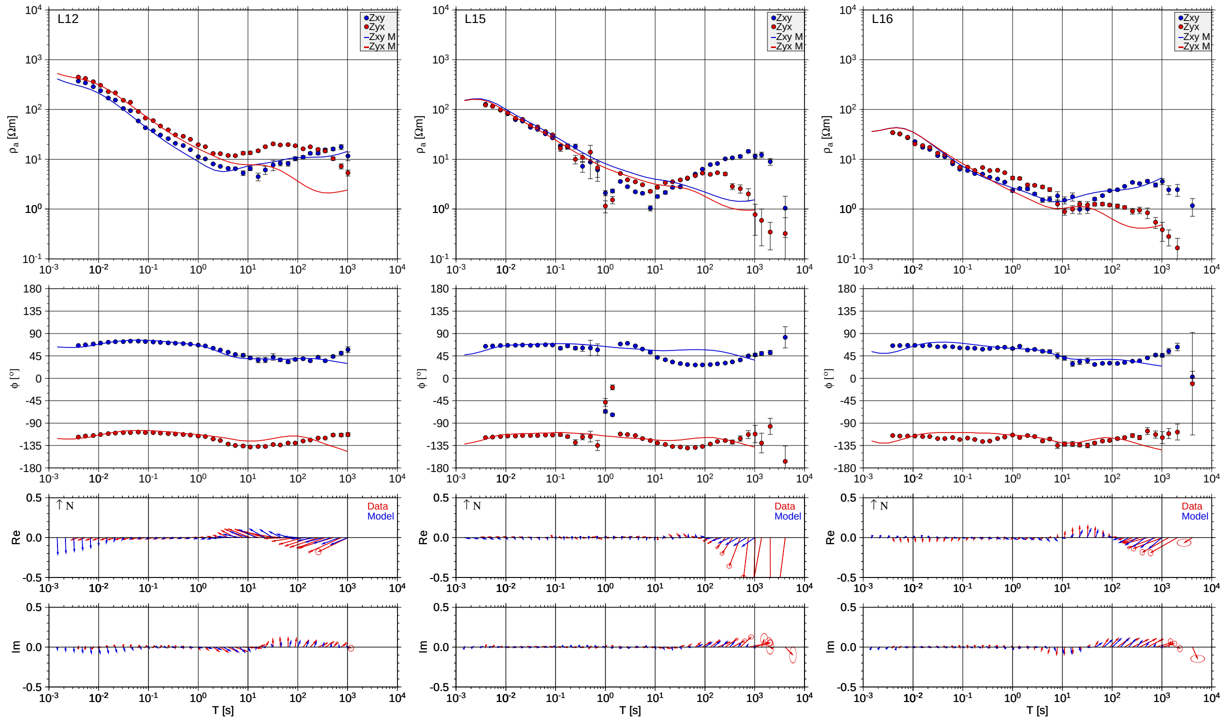

Figure 5.28: Comparison between measured data and the response of the model shown in figure 5.26 and 5.27 for 9 sites around Lascar volcano (comes from p. 85).

5.3 3D inversion of AMT data

Another tool available in the search for a model which can fit the measured data, is the 3D inversion program implemented by W. Siripunvaraporn. WSINV3DMT (Siripunvaraporn et al., 2005) is a 3D inversion program extended and implemented from the 2D data space Occam's inversion (Siripunvaraporn and Egbert, 2000), seeking the minimum structure model subject to an appropriate fit to the data. The difficulties associated with the use of Occam's approach to 3D MT inversion, due to the size of the model parameter M, can be overcome with a data-space approach, where matrix dimensions depend on the size of the data set N, rather than M. As in general N << M for MT data, as discussed in Siripunvaraporn and Egbert (2000), the transformation of the inverse problem to the data-space can significantly improve the computational efficiency, making the 3D inversion practical for normal PC's. In Occam's inversion, the "smoothest " model, subject to an appropriate fit to the data is achieved by finding stationary points of an unconstrained functional $U(m, \lambda)$:

$$U(m, \lambda) \quad = \quad (m - m_0)^T {C_m}^{-1}(m - m_0) + \lambda^{-1}\left\{(d - F[m])^T {C_d}^{-1}(d - F[m]) - {X_*}^2\right\} \tag{5.6}$$

where m is the resistivity model, m_0 the prior model, C_m the model covariance matrix, d the observed data, $F[m]$ the model response, C_d the data covariance matrix, X_* the desired level of misfit, and λ^{-1} a Lagrange multiplier. To find the stationary points of 5.6, the penalty function $W_\lambda(m)$ should be differentiated with respect to m. Where the penalty function is given by:

$$W_\lambda(m) = (m - m_0)^T {C_m}^{-1}(m - m_0) + \lambda^{-1}\left\{(d - F[m])^T {C_d}^{-1}(d - F[m])\right\} \tag{5.7}$$

When λ is fixed , both U and W_λ have the same stationary points. By minimizing W_λ with a series of λ, the stationary points of U can be obtained.

Because of the non-linearity of the MT inverse problem, an iterative approach is required, based on linearizing $F[m]$,

$$F[m_{k+1}] = F[m_k + \Delta m] = F[m_k] + J_k(m_{k+1} - m_k) \tag{5.8}$$

Here, the subscript k denotes the iteration number, and $J_k = (\partial F/\partial m)_k$ is the NxM sensitivity matrix calculated at m_k. Substituting equation 5.8 in $W_\lambda(m)$, and finding the stationary points, we obtain a series of iterative approximate solutions:

$$m_{k+1}(\lambda) = \lambda[{C_m}^{-1} + {\Gamma_k}^m]^{-1} {J_k}^T {C_d}^{-1} X_k + m_0 \tag{5.9}$$

where, $X_k = d - F[m_k] + J_k(m_k - m_0)$, and the "model-space cross product" matrix ${\Gamma_k}^m = {J_k}^T {C_d}^{-1} J_k$ is a MxM positive semi-definite symmetric matrix. In order to find the stationary points of equation 5.6, in each iteration equation 5.9 is computed with a series of trial values of λ. The goal of iterations in the early stages is to bring the misfit down to the target level ${X_*}^2$, and once the misfit reaches the desired level, the model of smallest norm which keep that misfit is sought using different values of λ.

As shown in Siripunvaraporn et al. (2005), the solution for iteration k can be expressed as a linear combination of rows of the smoothed sensitivity matrix $C_m J^T$:

$$m_{k+1} - m_0 = C_m {J_k}^T \beta_{k+1} \tag{5.10}$$

Where β_{k+1} is an unknown expansion coefficient vector of the basis functions $[C_m {J_k}^T]_j$; $j = 1...N$. Substituting equation 5.10 into a linearized form of equation 5.7, and solving for its stationary points, it is possible to obtain a series of iterative solutions:

$$\beta_{k+1} = [\lambda C_d + {\Gamma_k}^n]^{-1} X_k \tag{5.11}$$

with ${\Gamma_k}^n = J_k C_m {J_k}^T$ the NxN "data-space cross product". As well as with the standard model-space Occam's inversion, it is possible to solve β_{k+1} using equations 5.11, update the model and then compute the misfit, all of these calculations with various values of λ. The main difference of solving the problem with the “model-space cross product” or the “data-space cross product” is that the dimension of the system of equations to be solved can be significantly reduced using the second one.

In order to efficiently use the WSINV3DMT inversion program, and following the recommendations given by its authors, a subset of the data was chosen, excluding sites with poor data quality and selecting only 3 periods per decade, reducing the size of the data (N) and therefore the CPU time of the inversion. The size of the model (M) was given by the discretization of the area of interest around the Lascar volcano, with a cell size of 1000 m x 1000 m x 250 m in the x, y and z directions respectively. This grid is rougher as the one used for the 3D forward modeling, but with finer grids the program was unable to run on a 2 GB RAM computer. This discretization does not include topography, because the inversion of a model with topography was not implemented in the current version of the program used.

Several inversions with different parameters were calculated, leading to fix the parameters controlling the inversion at the following values:
- Error floor of the data: 10 %
- Initial model (m_0 in equation 5.6) was considered as an homogeneous halfspace of 100 Ωm.
- Target RMS (${X_*}^2$ in equation 5.6): 1
- Model lenght scale, which controls the model covariance (C_m in equation 5.6): Time step (τ) = 10, δ = 0.1 in the three directions.
- Lagrange information (λ in equation 5.6): Starting λ = 1, step size (in log_{10} scale) = 0.5

The 3D inversion program used, tries to fit the measured data by comparing it with the complete impedance tensor of the models produced. However, no inversion for geomagnetic transfer functions is implemented in this inversion program. In order to properly compare the results obtained from the 3D inversion program and the ones obtained from the forward modeling, the calculation and comparison of modeled and measured induction vectors is needed. Both, this problem and the lack of topography were solved using WinGlink. The half-space model was imported, placing above it a discretized topography and making a forward modeling, obtaining the necessary files for the calculation and comparison of impedance tensor and tipper.

The result of this 3D inversion, shown in figure 5.29, is showing as in the previously developed forward modeling, a highly conductive zone placed just under Lascar volcano, but only for shallow depths (less than 2 km under the surface). For larger depths (2 - 8 km), there is a conductive zone placed to the S-E of the volcano and elongated to the S. The comparison of apparent resistivity and phase of the off-diagonal elements of the impedance tensor, together with the induction vectors for measured and modeled data is shown in figure 5.30. Around Lascar volcano, the apparent resistivities and phases are showing a good fit, as can be seen for sites L01, L03 or L08, even when these last two are showing some shift in the apparent resistivity curves.

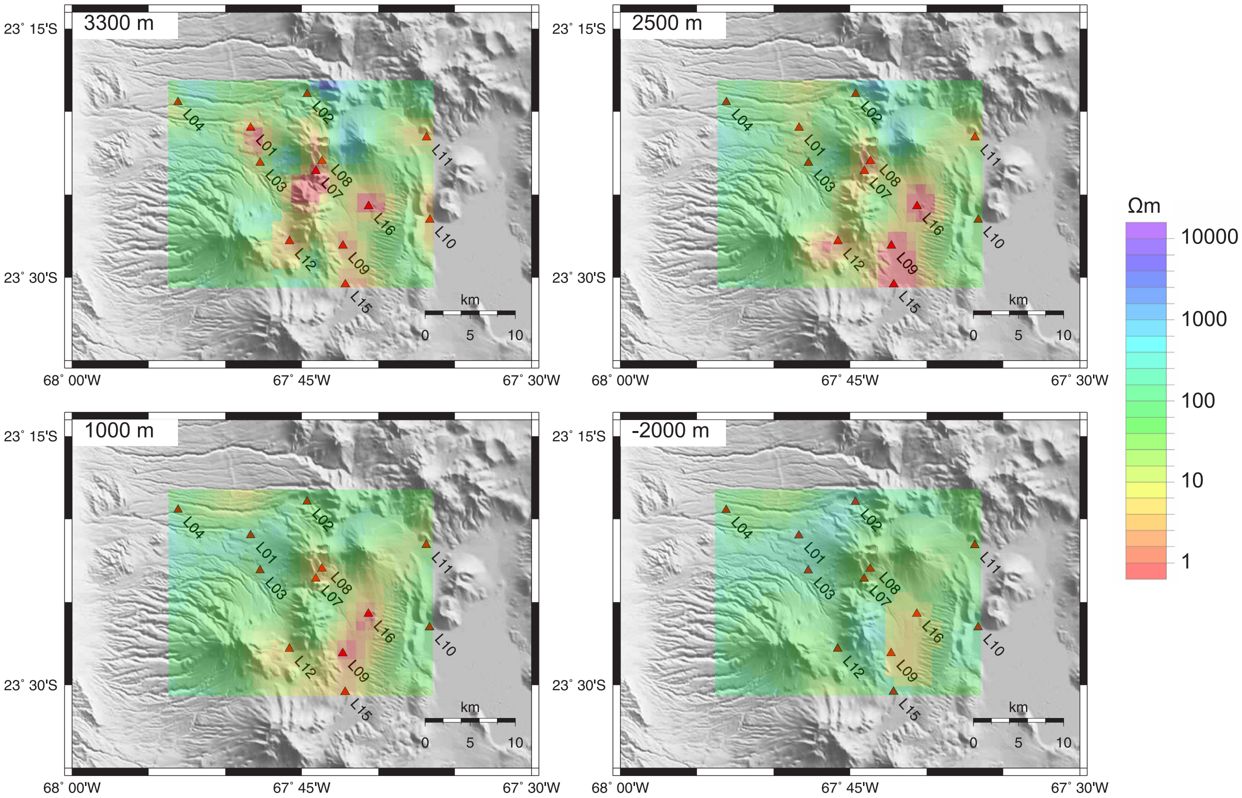

Figure 5.29: Result of a 3D inversion with AMT data around Lascar volcano. Red indicates conductive zones (∼1 Ωm), green, intermediate zones (∼100 Ωm) and blue, resistive zones (∼1000 Ωm). The altitude of these plan sections is indicated in the top left corner of each image (consider that the surface is at ∼4000 m).

The same is observed for the sites placed at larger distances from the volcano, as L09 and L12, for which the fitting between the obtained curves and the curves from the measured data is quite good. However, by comparing the induction vectors obtained from the 3D inversion and the measured ones, they coincide only for some sites, as L12, and for the sites close to the volcanic edifice, as L08, the modeled induction vectors are representing a different scenario as the measured ones. This result was expected as the 3D inversion routine used for this work is not trying to fit the tipper data, but only the impedance tensor of the measured data. Some stations (e.g. L03) were affected by static shift, produced by the presence of conductive anomalies close to the surface or due to the effect of the topography. The inclusion of topography in inversion routines could help to better estimate the static shift effect expected at each station, and try to define whether this effect comes from the topography or from heterogeneities in the shallow subsurface.

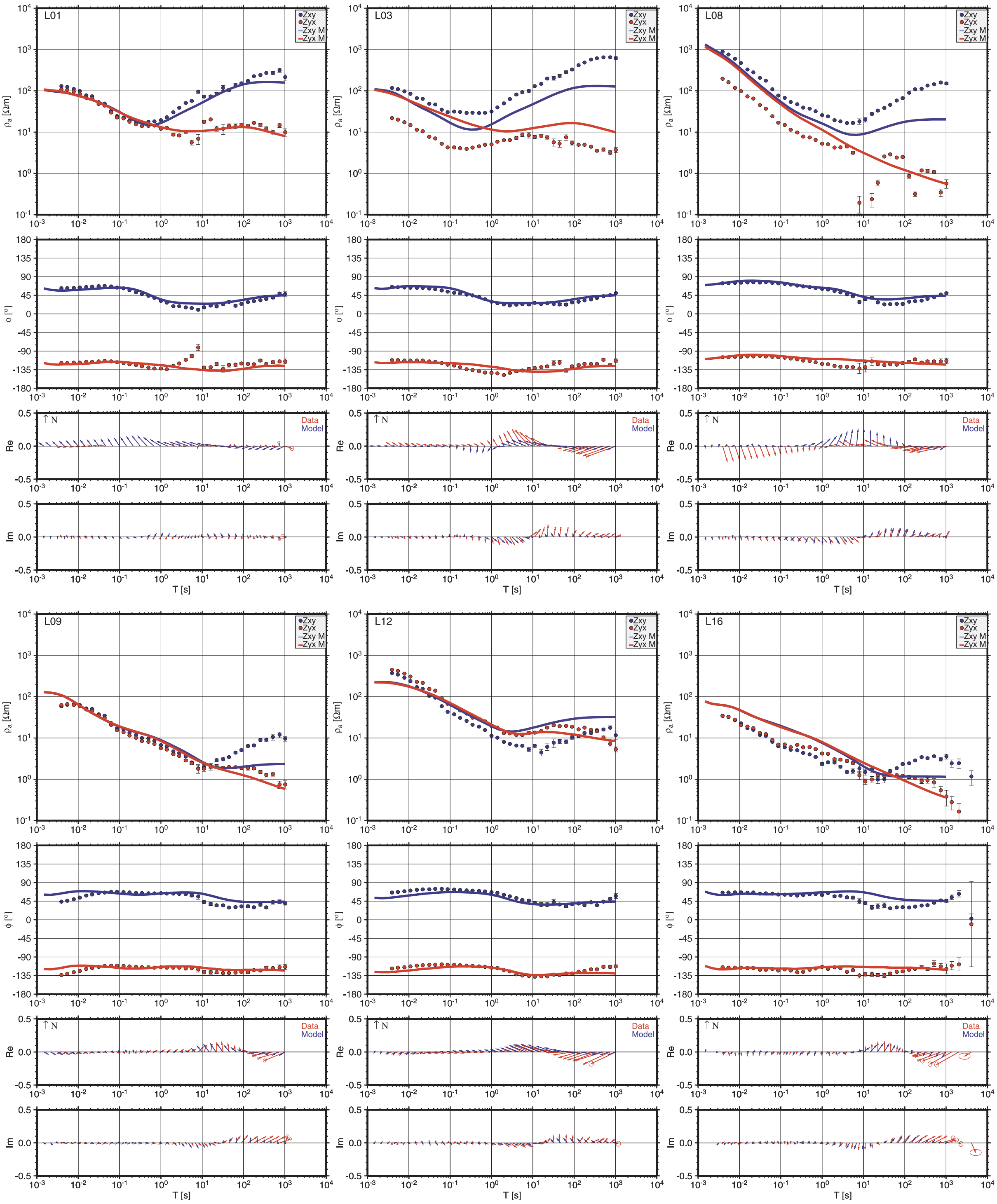

Figure 5.30: Apparent resistivity and phase of the off-diagonal elements of the impedance tensor, together with the induction vectors for measured and modeled data for six different sites around Lascar.

Nevertheless, the obtained 3D model gives some hints about the conductivity structure around the volcano, even though it does not fit the complete data set. The conductive structures present in this inversion are placed in very similar places as the structures modeled with the forward modeling tool, also to the southeast of the volcano, and extending in almost the same depth range, even when the shape of this structures is different. Again, no large conductive zones extending until 5 or 10 km in depth were obtained directly beneath the volcanic edifice.

Chapter 6

Interpretation of the measured data

In order to have a more complete interpretation of the data, the next step in this study will be to join the models and results obtained from the magnetotelluric data and its implications with the geological and geophysical background for the study area, exposed in the previous chapters.

6.1 3D modeling results around Lascar volcano

During the modeling and inversion of the magnetotelluric data collected around Lascar volcano, some features were obtained, being necessary for the achievement of a good data fit. These features are the following:

- Resistive block to the W of the volcanic arc, close to station L04.
- Shallow conductors beneath the volcano and its surroundings, Especially close to stations L01 and L03 (around 10 Ωm).
- Deep conductive structure extending from the volcano to the SE, and deeper in the southern extreme of this zone.

The occurrence of a resistive body to the west of station L04 is supported by the induction vectors calculated for the AMT stations. For periods between 0.0625 s and 11 s, stations L04 and L05 show very strong induction vectors in opposite directions (see figure 6.1), clearly away from the trend of all the other stations, which show much weaker induction vectors.

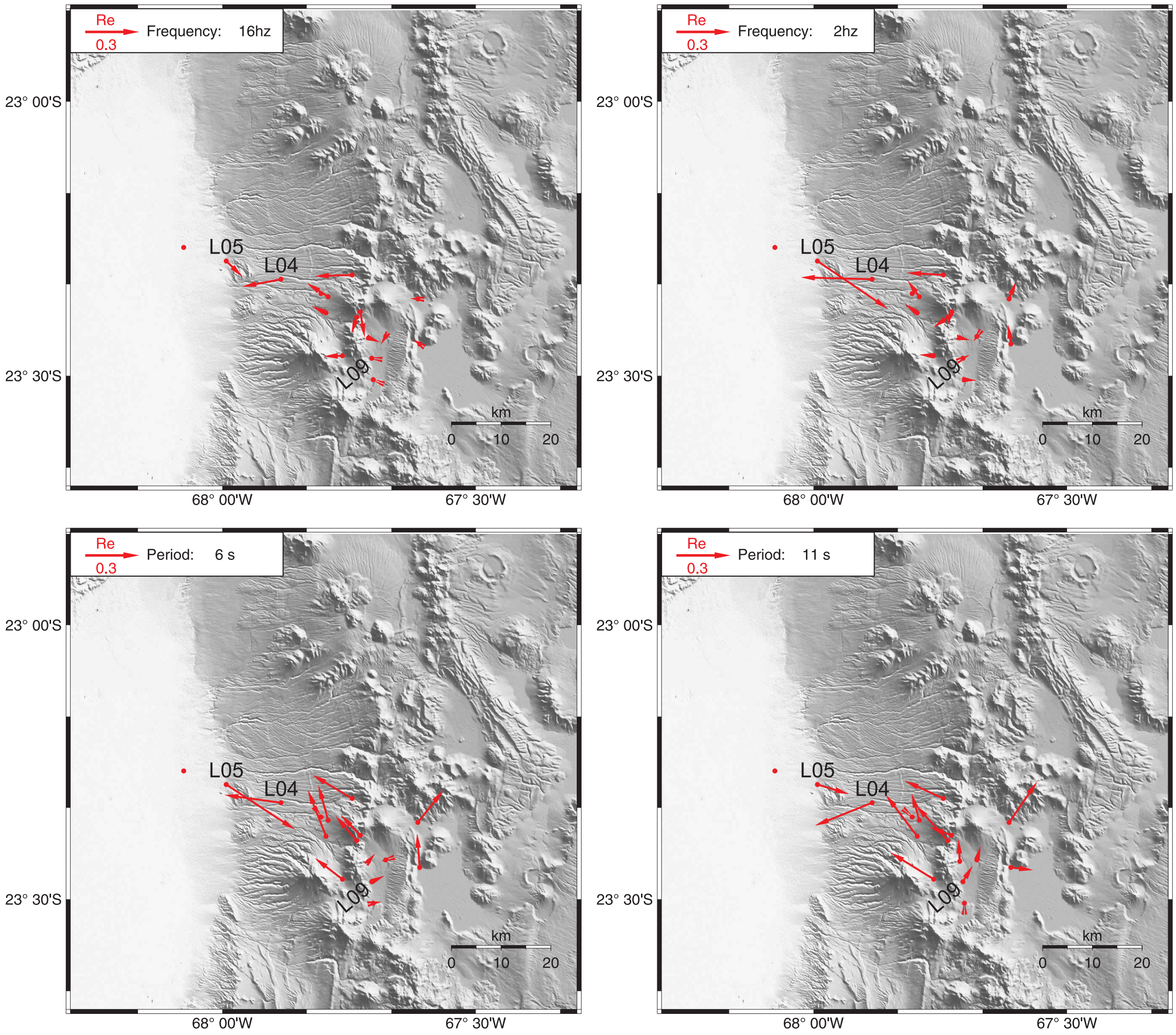

Figure 6.1: Induction vectors at four different periods between 0.0625 s (16 Hz) and 11 s.

The presence of a resistive block in this part of the profile could be related to the intrusive bodies of Cenozoic age in the zone, between the Cuyugas and Allana hills, as shown in figure 6.2. These intrusive outcrops, covered by volcano-sedimentary sequences of Permo-Triassic age can be just the upper part of an intrusive system that extends for some kilometers into the crust.

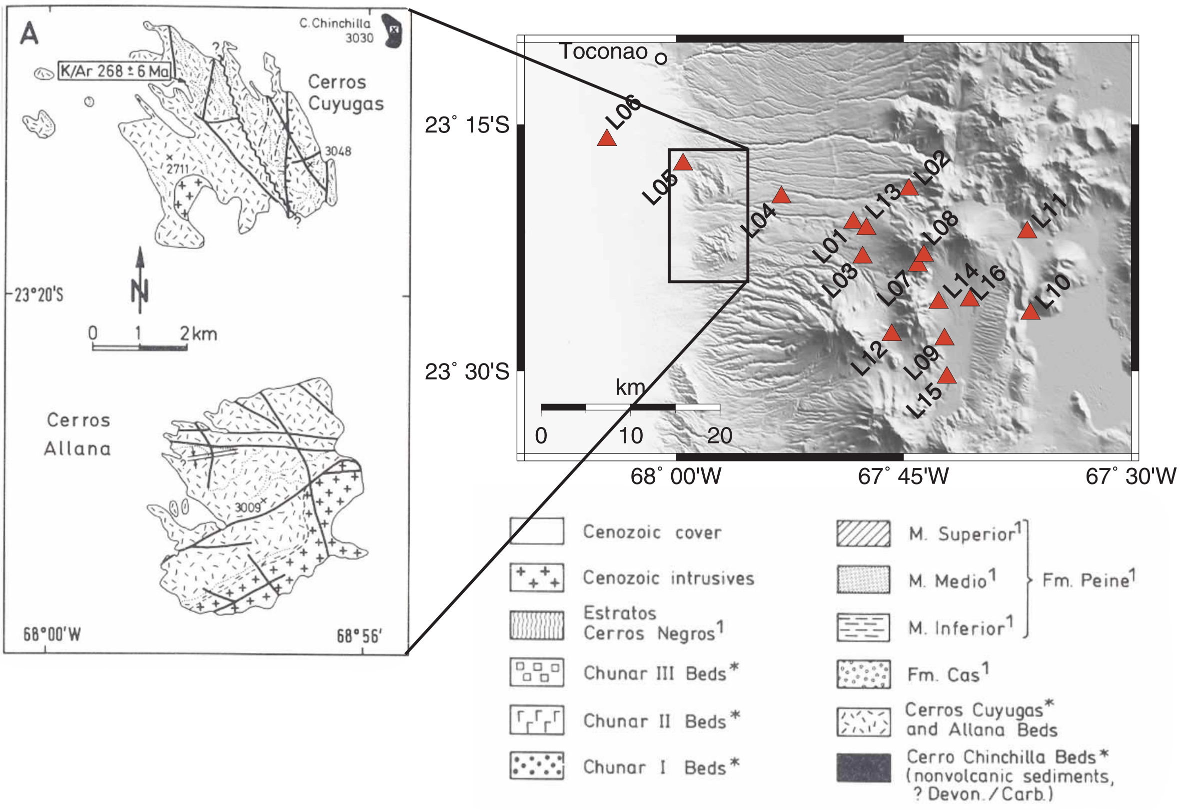

Figure 6.2: Geology of Cuyugas and Allana hills, and its position relative to the AMT sites. Geology extracted from Breitkreuz and Zeil (1994).

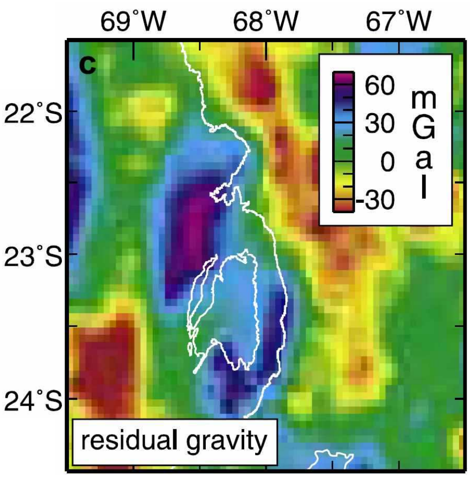

Figure 6.3: Isostatic residual gravity from Götze et al. (1994), showing a gravity high to the north-west, east and south of the Salar de Atacama basin. Salar de Atacama as well as the 3500 m elevation contour line is drawn here for orientation. Edited image extracted from Schurr and Rietbrock (2004).

This resistive block at the eastern side of the Salar de Atacama basin, together with the resistive zone observed in the LMT profile between stations PEI and SOP (shown in figure 5.30), south-east of the same basin, are related to a local high in the gravity field observed around the Salar de Atacama, shown in figure 6.3. Götze et al. (1994) speculate that large amounts of mafic intrusives from an Ordovician subduction zone might be responsible for the gravity anomaly, while Schurr and Rietbrock (2004) relate this anomaly with the high-pressure, low-temperature Permian metamorphic rocks that crop out in the Sierra de Limon Verde, close to Calama, where the high gravity zone continues to the northwest.

In order to analyze the conductive properties of the shallower layers, it is important to refer to the surface geology which characterizes the zone around this profile. Lascar volcano stands principally on magmatic and volcano sedimentary rocks of Paleozoic age and sedimentary rocks of Tertiary age (Ramírez and Gardeweg, 1982). Miocene to Pliocene volcanism has produced lavas and domes (andesitic, dacitic and rhyolitic) and some important ignimbrites (Pliocene) that have covered the Paleozoic and Tertiary deposits referred above. Concentrating in the zone around Lascar volcano, it is characterized by volcanic units deposited since the Pliocene (units Q3l, Q3t, P3l, P3t in figure 6.4), with the presence of Miocene domes to the east (unit Ms3l in figure 6.4) associated with La Pacana Caldera. To the west and south west of the volcano, sedimentary and volcano sedimentary units of Paleozoic (Carboniferous-Permian) age can be identified (unit CP2 in figure 6.4), and also a magmatic and volcanic unit of Permian-Triasic age (unit Ptrg in figure 6.4).

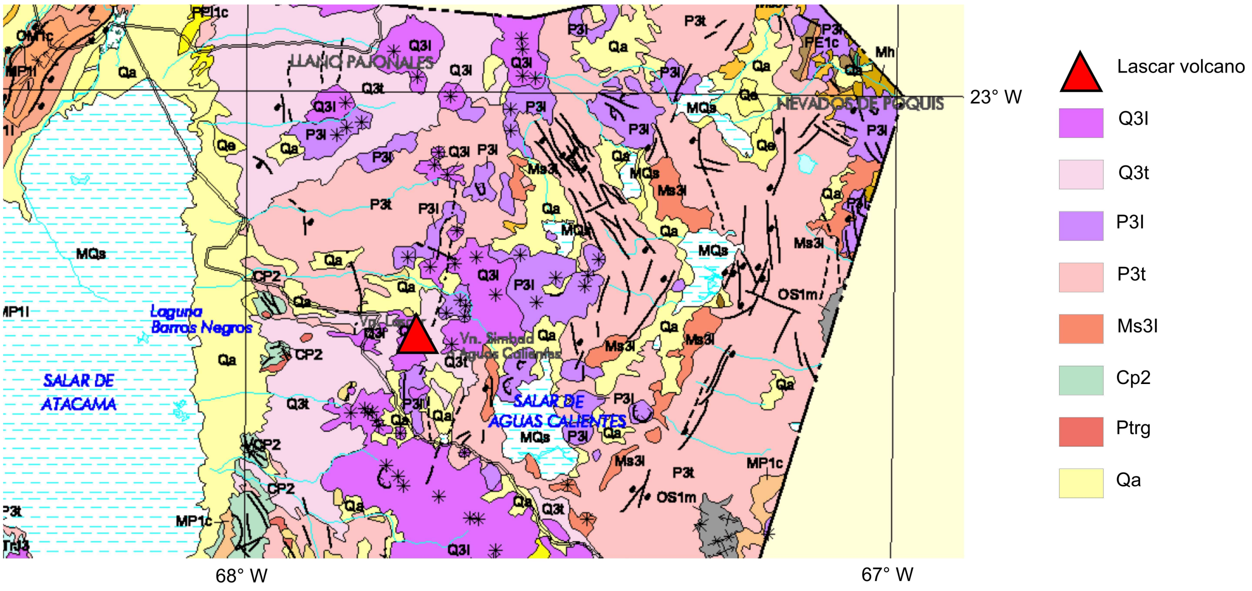

Figure 6.4: Extract from the Geological Map of Chile 1:1.000.000 (SERNAGEOMIN, 2002). Units P3l, P3t, Q3l and Q3t are ignimbrites and volcanic units from Pliocene and Quaternary ages; Ms3l are domes of Miocene age and CP2 and Ptrg are Paleozoic volcanic and volcano sedimentary units.

Most of the volcano sedimentary units near the surface were modeled with resistivity values between 100 and 500 Ωm, with higher values in the volcanic edifice, reaching 800 Ωm. In places where sedimentary basins are present, as the Salar de Aguas Calientes (close to station L10 and L11) the surface resistivity obtained from the models is much smaller, reaching 1-10 Ωm in the first hundred meters. The situation in the north-western side of the volcano is different, because the relatively conductive zones present in this part of the models are not extending from the surface, but between 300 and 800 m in depth, with resistivities of 10 Ωm, which could be related with the presence of an hydrothermal system in this area and hot water springs to the north of the volcano.

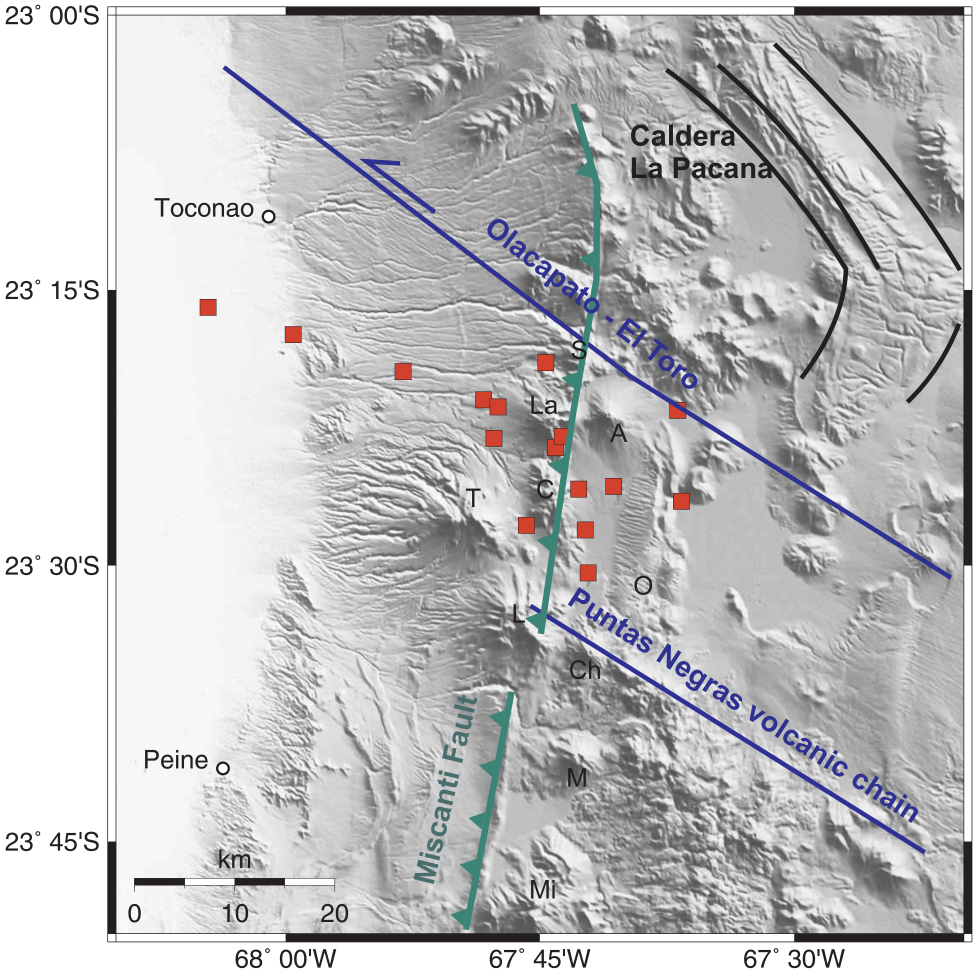

Figure 6.5: Some of the main faults present around Lascar volcano. In blue, the Olacapato - El Toro fault system inferred from Matteini et al. (2002a), and the Puntas Negras volcanic chain related to it (Matteini et al., 2002a,b). In green, the Miscanti Fault system and its northward prolongation (Aron et al. (2008); González et al. (2009) and F. Aguilera, pers. comm.). The main volcanic centers are named as follows. S: Saltar, La: Lascar, A: Aguas Calientes, C: Corona, T: Tumisa, O: Overo, L: Lejía, Ch: Chiliques, M: Miscanti, Mi: Miñiques. Red squares represent the AMT stations.

An explanation for these shallow conductive zones is related with the presence of the Olacapato - El Toro fault system (OTF, also known as Calama - Olacapato - El Toro (Matteini et al., 2002a; Petrinovic et al., 2005)). The OTF, one of the most extensive lineaments in the Central Andes, is a left-lateral transcurrent fault system running approximately 700 km from the Pacific coast of Chile to the Eastern Cordillera in NW Argentina (Salfity, 1985; Marret et al., 1994). This lineament, as others present in this part of the Andes (e.g. Archibarca-Galán, Culampaja-Farallón Negro) coincide with southeastward-trending volcanic breakouts from the main arc, suggesting a structural control on Miocene magmatism. Such is the case of the Puntas Negras volcanic center, and the Aguas Calientes and Negra Muerta calderas, further to the SE in the Argentinian Puna and also related to the Olacapato-El Toro fault zone (Petrinovic et al., 2005; Riller et al., 2001). The spatial coincidence of transverse volcanic ranges with these fault zones points to a genetic relationship between faulting and caldera formation. However, clear structural field evidence for a kinematic link between prominent faults and volcano-tectonic structures is sparse as most of the calderas' substrates, which would potentially host such structures, are obscured by erupted material (Riller et al., 2001).

The presence of this fault system around Lascar volcano, obscured in this zone by volcanic or other superficial deposits, could play an important role in the enhancement of conductivity at shallow levels, in the emplacement of magma beneath this currently active volcanic center, or even in the ascent of magma through the volcano.

Another fault system which is playing an important role in the emplacements or ascent of magmas is the Miscanti fault system, which represents the easternmost expression of the fold and thrust belt system (Aron et al., 2008). The emplacement of relatively old volcanic centers, as the cerros Corona and Saltar, seem to have been controlled by this fault system (Donoso et al., 2005), as well as young volcanic centers (Lejia, Lascar) which are located very close to the fault or in N-S lineaments parallel to this fault (e.g Miñiques, Miscanti, Chiliques and Overo). The coincidence between the Miscanti fault and the western border of the conductive zone obtained from the 3D forward modeling is interesting considering the possible interpretation of this conductive zone as a magmatic reservoir, trapped at shallow crustal levels by N-S and NW-SE fault systems in a compressive environment, and reaching the surface as volcanoes or parasitic structures guided by the same faults.

Several test were carried out in order to constrain the depths between which the high conductivity zone to the S-SE of the volcano should be placed in order to fit our data. As it was shown in the previous chapter, the electromagnetic response measured at a station depends not only on the size of the anomalous body, but also on its resistivity, shape and relative position. Analyzing the results of one of the best fitted models obtained (fig. 5.26), the depth extension of the highly conductive anomaly to the S-SE of the volcano is reaching $\sim$6 km in its deeper part, beneath stations L09, L12 and L15, corresponding to one of the models with the smallest depth extension for the conductive zone. The association of a conductive zone at this depth with the presence of magma in this area as a reservoir for Lascar volcano, is supported by the results of geochemical and petrological studies.

This conductive structure is located along a N-S trend, between Lascar and Chiliques volcanoes. As it was shown in the introduction of this work, Lascar volcano presented a strong activity during the 1990's, including the large explosive eruption of April 1993. However, no evidence of a magma deposit could be obtained from different measurements carried out in this area, particularly in seismic studies, e.g. Hellweg (1999a,b, 2000). According to these measurements and analysis, the harmonic tremors measured in this volcano should be produced by the movement of water or gases, not magma, and they should be generated near the surface (close to atmospheric pressure), probably in the active crater. But even when these results are not pointing directly to the presence of a magmat deposit, the phenomena producing the measured effects, hydrothermal systems and high pressure gases, need a heat source.

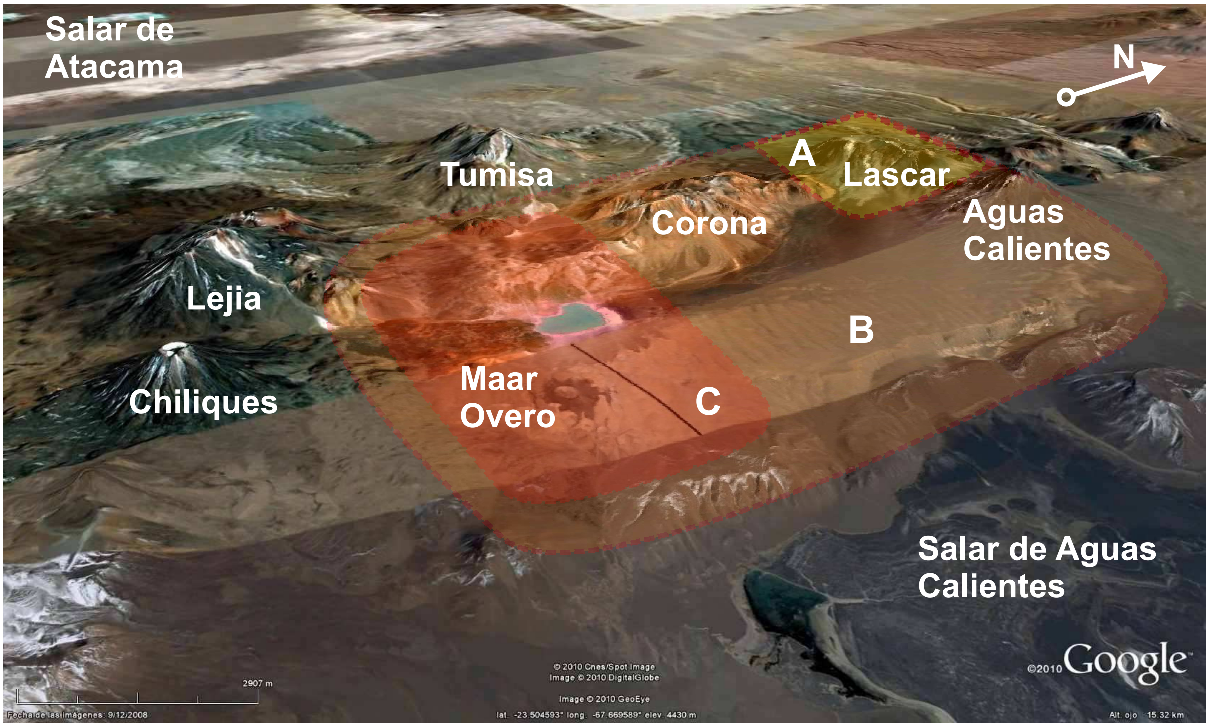

Figure 6.6: View from the SE of the volcanic centers in this area. From the 3D forward modeling, 3 main conductive zones can be identified: zone A, extending from the base of Lascar volcano some hundreds of meters in depth; zone B, covering a wide area and extending to the SE of Lascar, between 1 and 3 km beneath the surface; and zone C, which is at the southern extreme of zone B, but reaching larger depths and resistivities of $\sim$1 Ωm.

Other volcanic centers in this area, as Chiliques volcano, present several youthful lava flows, some of which are considered to be of Holocene age. This volcano had previously been considered to be dormant, however, in 2002 a NASA nighttime thermal infrared satellite image from the Advanced Spaceborne Thermal Emission and Reflection Radiometer (ASTER) showed low-level hot spots in the summit crater and upper flanks, while the examination of an earlier nighttime thermal infrared image (May, 2000), showed no such hot spots. The most recent activity in the vicinity of Chiliques volcano may have been the eruption that formed the Overo hill, a young maar of 600 m in diameter, erupted along a regional fault, which produced the least silicic youthful volcanic rocks found in this part of the Central Andes (de Silva and Francis, 1991).

Following the results obtained from the 3D modeling, the conductive zone to the SE of Lascar volcano can be divided in two zones, one extending immediately to the S-SE of the volcano, and to the south for 10 km, with a depth extension between 1 and 2–3 km below the surface and a resistivity of $\sim$5 Ωm. This conductive zone, marked as B in figure 6.6 is shallower and less conductive than its southern continuation, the zone A in figure 6.6, with a resistivity around 1 Ωm and reaching depths of 7–10 km.

Petrological and geochemical experiments were performed in the Institut of Mineralogy of the Leibniz Universität Hannover and in the Geochemistry Department of the Geowissenschaftliches Zentrum Göttingen, with rock probes from different eruptive episodes of Lascar volcano. Based on the measured composition of two main minerals, clinopyroxene and orthopyroxene using an electron microprobe and applying the results to the model of Putirka (2008), the formation conditions for the volcanic rocks of different eruptive episodes of Lascar were inferred (figure 6.7). Laboratory experiments trying to recover the mineral assemblage observed in rock probes from Lascar volcano were also carried out, together with comparisons between residual melt in the experiments with the natural bulk rock composition observed in the probes, in order to check the formation conditions of the erupted material. These experiments yield to a possible magmatic chamber present between 10–15 km depth, and a deeper one at 40 km depth (André Stechern, pers. comm.).

If a magmatic chamber were present at 10–15 km depth, according to the magnetotelluric data it should be located to the S-SE of the volcano, in zone C shown in figure 6.6, which could extend until 10 km depth and still fit the data, conforming a possible heat source for the different processes observed in the surrounding area and in the volcanic centers of this zone. An alternative explanation could be given by a deeper magmatic chamber (e.g. 15 km), presenting a resistivity not very different to its surroundings (e.g. 20–30 Ωm), and therefore, obscured by the shallower and more conductive zones inferred in this work and needed for a good data fit. The magma in this case should ascend by dyke-like structures, narrow enough not to be detectable with magnetotelluric measurements. 3D forward models including such a magma chamber extending between -15 and -20 km beneath the volcano together with all the other resistive and conductive features needed by the data, yield very similar results as models without it, making its presence possible, but not necessary for a representative 3D model.

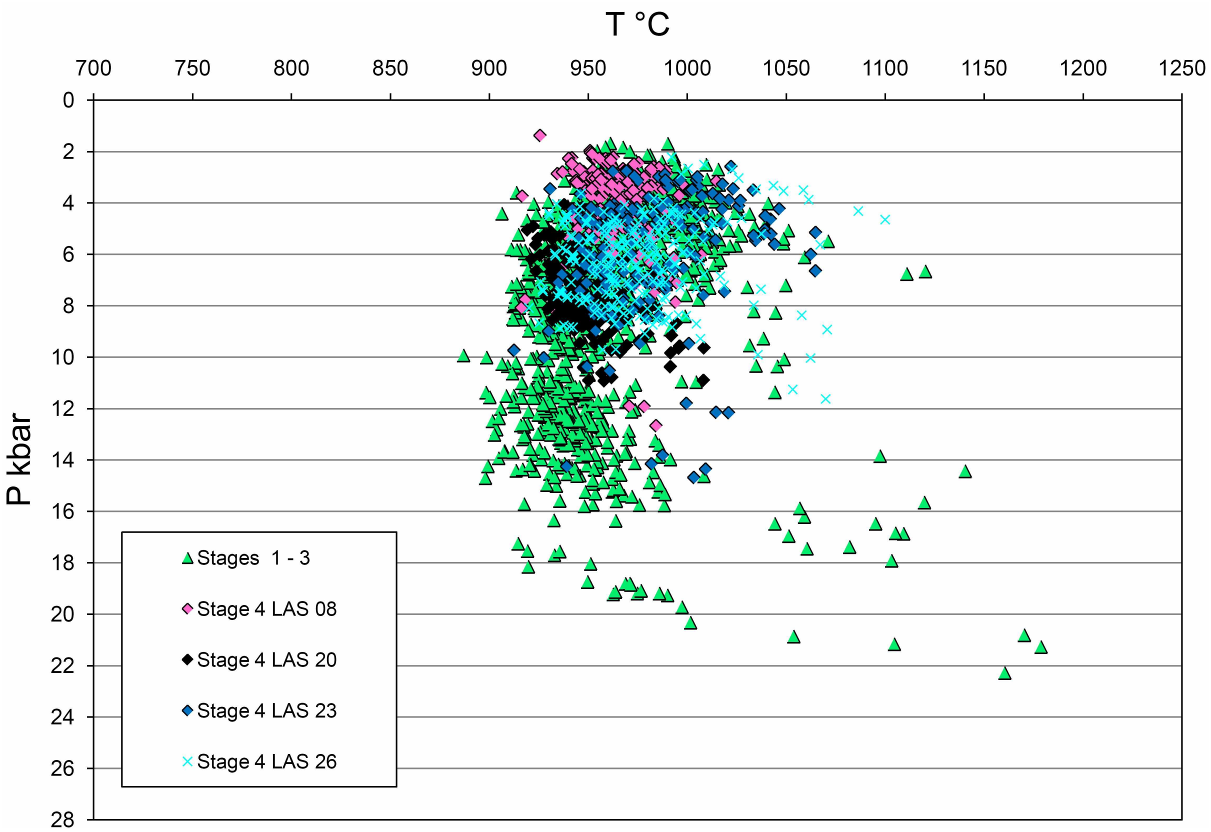

Figure 6.7: Pressure-Temperature plot for Clinopyroxene and Orthopyroxene present in rock samples of the different evolutionary stages of Lascar volcano (André Stechern, pers. comm.).

6.2 LMT data and 2D inversion

The tipper data for the first periods show clearly the influence of the Salar de Atacama basin between stations PEI and PAC, as a very conductive zone with resistivities of $\sim$ 1 Ωm. The extremely high conductivity in the Salar de Atacama is not a surprise, since in-situ measurements in different small water springs inside the Salar showed values around 13 S/m at temperatures of $\sim$ 25°C, very conductive considering that sea water has an average conductivity of 3-4 S/m. The depth of this conductive zone seems to be different along its extension, as the eastern part extends from the surface until 1 or 2 km, and the western part seems to reach larger depths, until $\sim$ 5 km. This can be seen more clearly in the tipper inversion shown in figure 5.4 A, reaching its deeper part below the station ATA, and present in the joint inversion of the three modes (TE, TM and tipper), between stations PEN and PAC (zone marked as B in figure 6.9). About the depth of the Salar de Atacama, studies including seismic lines indicate a considerable lateral variation in the v_p depth distribution in the uppermost crust. A relatively high v_p > 6.3 km s^{-1} was found at shallower depths under the Cordon de Lila, surrounded to the east and west by a relatively low velocity zone (Reutter et al., 2006). This high velocity zone can be considered here as the basement of the Salar de Atacama, constituted by Carboniferous and/or Permian to early Triassic volcanic and sedimentary successions partly penetrated by late Cretaceous plutons in the western, southern and southeastern borders of the Salar (Reutter et al., 2006). Above this basement, the basin fill is mainly of Cretaceous to Holocene age and consists of an up to 7500 m thick section of mainly siliciclastic rocks, including the Cretaceous-Eocene Purilactis group, overlain by 1000-1600 m of evaporites (Muñoz et al., 2002).

In figure 6.8, a density model calculated from a gravimetric profile at 23°32'S, 5 km to the north of our LMT profile, shows a density distribution in which a northward extension of the Cordon de Lila formation, with relatively high density is placed beneath the center of the Salar de Atacama. To the west of this feature, a layered but fractured zone with lower densities extends some kilometers in depth.

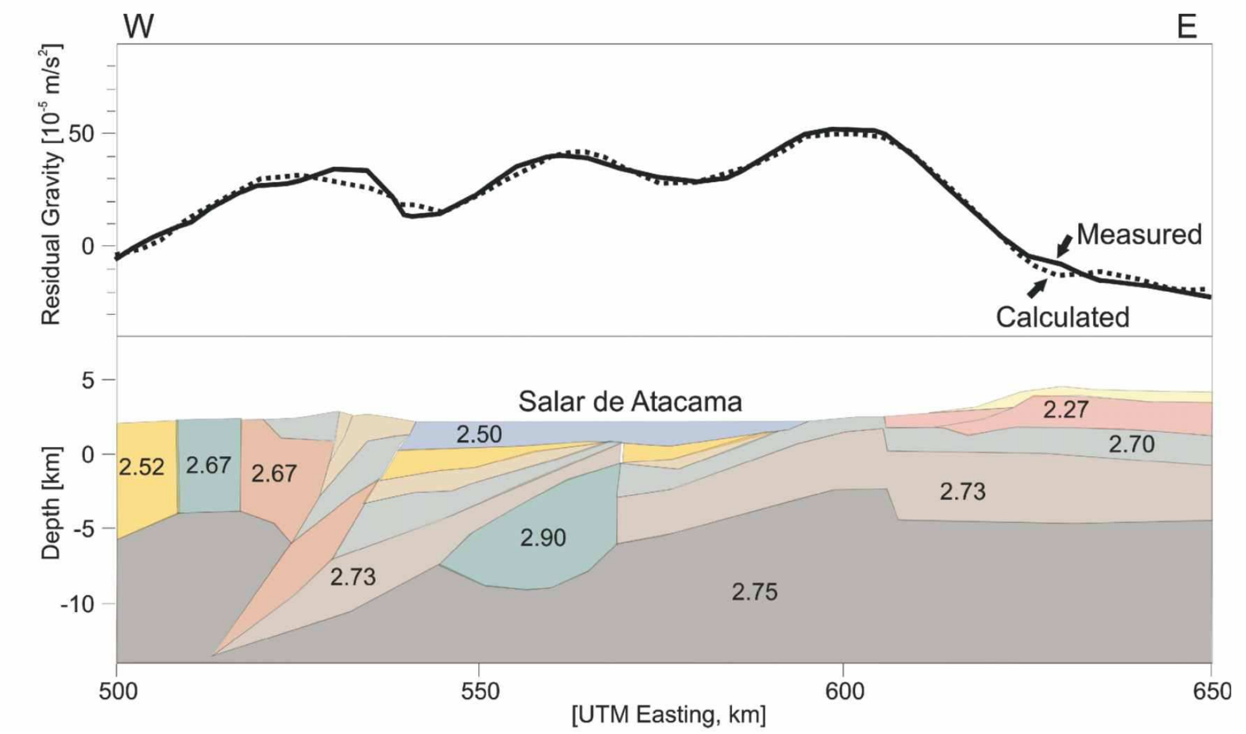

Figure 6.8: Gravity profile and density model along a section through the Salar de Atacama at 23°32'S (Reutter et al., 2006).

Between the Cordon de Lila and the El Bordo escarpment (western border of the Salar de Atacama), several faults have been inferred based on geological data, gravity studies and seismic experiments. These structures, originally normal and then reversed as a result of the strong shortening experimented in this region during the Eocene and mid-Miocene, could be playing an important role in the infiltration of fluids to deeper levels in the southwestern zone of the Salar de Atacama. Another hypothesis for the deeper extension of the conductive zone to the west of the Cordon de Lila, suggests that this tectonically depressed zone was a graben supported by the original normal faults, and this basin concentrated old lakes and evaporitic deposits which could explain a greater thickness of this kind of sediments, including perhaps horizons with fluids in this zone (G. Chong, pers. comm.).

Concentrating now on the results at greater depths, the inversion of the tipper data (shown in figure 5.4 A) indicates the presence of a highly resistive body directly below the Salar de Atacama basin at depths between 10 and 60 km. However, this result seems to be induced by two different resistivity zones that are below the western and eastern borders of this basin as can be seen in the joint inversion of tipper, TE and TM modes shown in figure 6.9. The westernmost resistive zone extends below the Domeyko Cordillera, formed by Late Carboniferous to Early Permian rhyolitic ignimbrites and domes, associated with volumetrically minor basaltic to andesitic lavas and intruded by granitoid plutons which yield K/Ar, Rb/Sr and U/Pb (zircon) ages ranging between 300 and 200 Ma (Mpodozis et al., 2005, 1993; Breitkreuz and van Schmus, 1996).

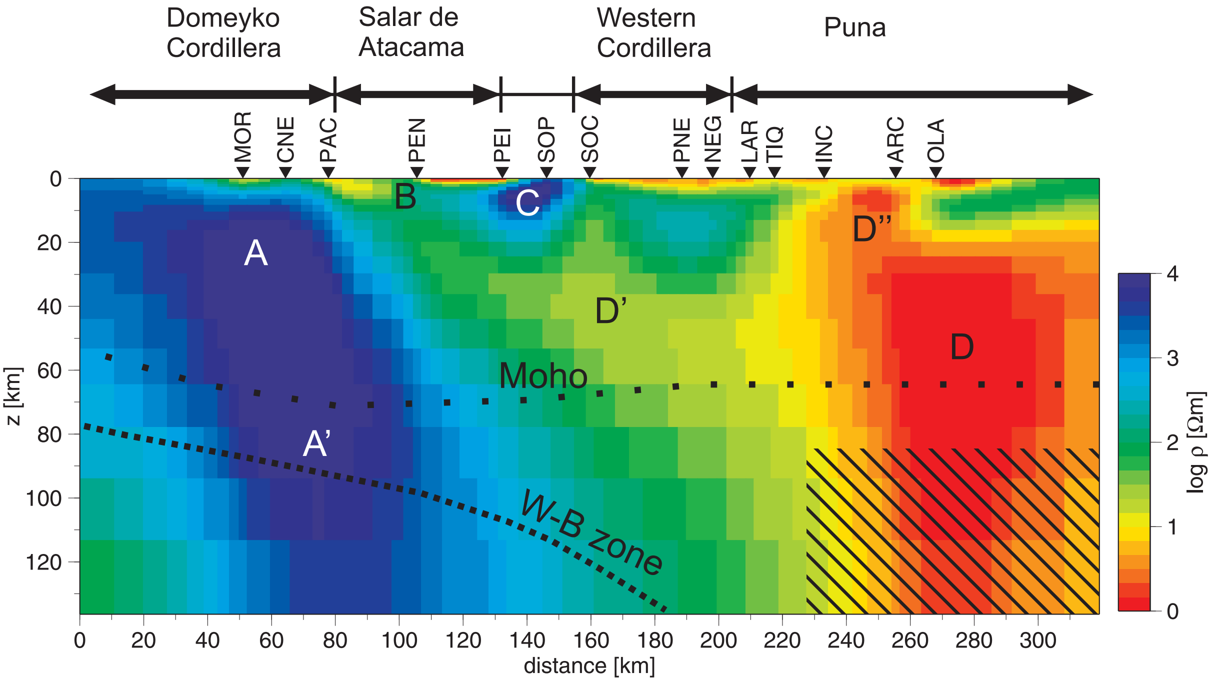

Figure 6.9: 2D inversion of tipper, TE and TM modes of LMT data, including a roughly approximated Moho from Yuan et al. (2000) and the Wadati-Benioff zone (W-B zone) approximated from Cahill and Isacks (1992). The dashed area beneath the Puna is not resolved.

The depth of this resistive zone is not well resolved, however it could be the case that the resistive crust under the Domeyko Cordillera, extending until ∼50 km (zone marked as A in figure 6.9), is followed in depth by a resistive downgoing slab (marked as A' in figure 6.9), giving the impression of a unique resistive block.

Another resistive block is extending from the surface until 10 km depth between stations PEI and SOC (marked as C in figure 6.9). This relatively shallow resistive zone underlies the Cas and Peine formations which are partly penetrated by late Cretaceous plutons, as is also observed to the S (below Cordon de Lila) and SW of the Salar de Atacama (Reutter et al., 2006). The presence of plutonism in this area, in the form of 3D resistive heterogeneities, can explain the high skew values observed in this part of the profile, as was shown in the previous chapters (figure 4.4).

A large and highly conductive zone is located 100 km to the east of the volcanic arc. This zone, marked as D in figure 6.9, extends from 30 until 100 km depth, and seems to be related with a shallow conductive zone beneath station ARC (D" in figure 6.9) and also with a less conductive zone (∼10 Ωm) which departs from structure D to the west and upwards, resulting in a relatively conductive zone below the volcanic arc at 40 km depth (D' in figure 6.9). The structures D, D' and D", were subject to several sensitivity tests, showing clearly that the presence of all these structures improved the convergence of the model.

The shallowest part of the conductive zone beneath the Puna, labeled as D" in figure 6.9, coincides with the place where the Olacapato - El Toro fault system crosses the LMT profile. The Olacapato - El Toro fault zone conforms a structural boundary in this plateau as all the historical seismicity and micro seismicity in the Puna is located from this fault zone to the south, and concentrated in the first 10 km depth, indicating a high geothermal gradient and a shallow brittle-ductile transition (Asch et al., 2006). This fault zone could be also providing paths for the infiltration of fluids from the surface, enhancing the conductivity at shallow depths and therefore explaining the presence of the conductive zone D".

Analogous cases of conductive zones under the Altiplano can be found in previous magnetotelluric studies (Brasse et al., 2002; Brasse and Eydam, 2008) as well as more to the south under the Puna, in the backarc of the northwestern Argentinean Andes (Lezaeta et al., 2000; Lezaeta and Brasse, 2001), which are in good agreement with seismic studies showing a detailed image of seismic attenuation in the crust and uppermost mantle in the Central Andes (Yuan et al., 2000; Schurr et al., 2003; Asch et al., 2006).

The anomalies in both cross-sections of figure 6.10 (Schurr et al., 2003) are showing some differences in shape, depth extent and Q value, indicating a rather fast change with latitude, considering that both images are only 100 km away from each other in the N-S direction. Nevertheless, the easternmost attenuation anomalies for both cross-sections in figure 6.10 coincide particularly well with the shape and depth extent of the conductive anomaly D obtained from the 2D inversion of magnetotelluric data. The westernmost attenuation anomaly, placed close to the volcanic arc in both cross-sections, can be related to the relatively conductive zone D' shown in figure 6.9, which starts at 40 km depth and extends upwards and to the west until 10 km beneath the active volcanic arc, suggesting a path for ascending fluids which enhance the conductivity in this part of the profile, and providing a possible source for partial melts in the crust and hydrothermal processes associated with the volcanic arc.

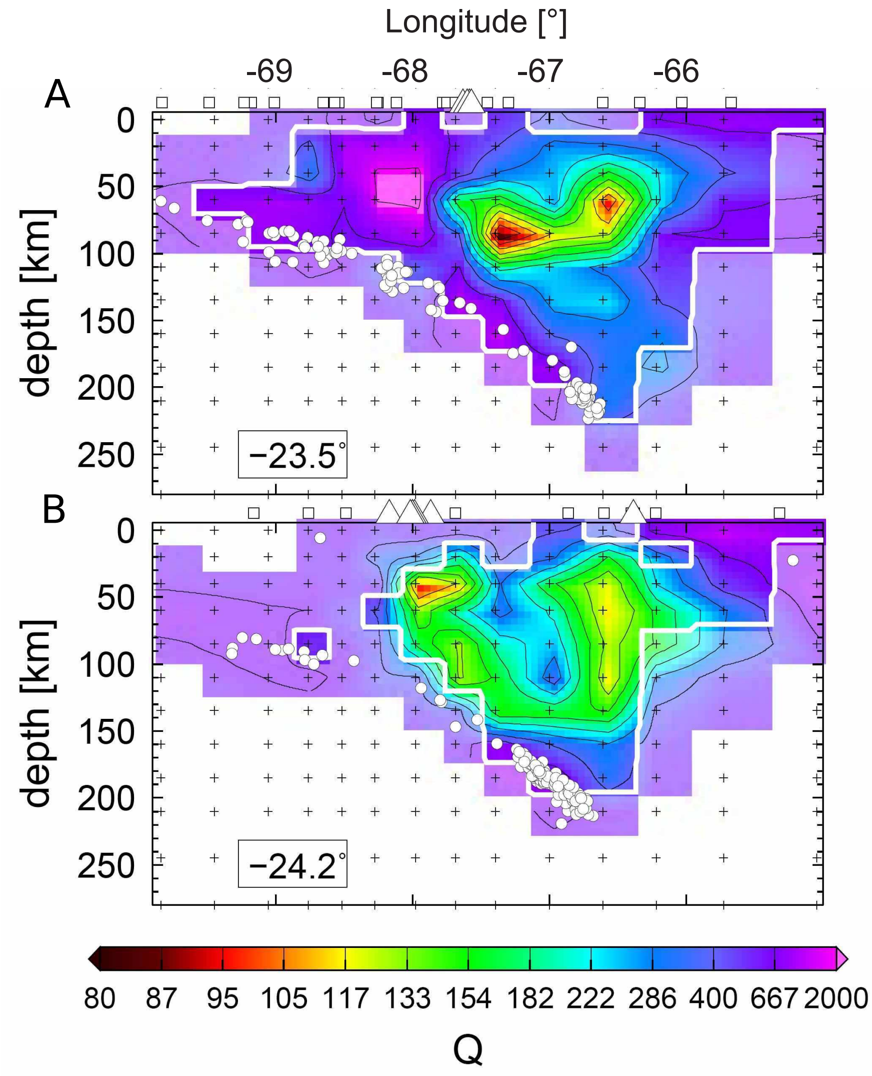

Figure 6.10: Cross sections from a 3D tomography showing seismic attenuation (Schurr et al. (2003); B. Schurr, pers. comm.). The LMT profile is located between these two cross sections, (A) at -23.5°S and (B) at -24.2°S

This interpretation is supported by the presence of extensive fields of Neogene ignimbrites in the plateau region of the Central Andes, especially in the Altiplano-Puna Volcanic Complex (APVC), many of which have been shown to be derived from crustal melting (De Silva, 1989). Detailed petrologic and geochemical studies of ignimbrites from the APVC have established the following resemblances among the units which suggests similar sources and magma evolution:

- Extremely large eruptive volumes, exceeding 1000 km^3 for individual units.

- A compositional monotony dominated by high-K, calcalkaline dacite and only about 5% rhyolites. Most large units lack any major compositional variation.
- High crystallinity (30-50%) of pumice. Major phenocryst phases are plagioclase, quartz, hornblende and orthopyroxene (Schilling et al., 2006).

As the extension in depth of this highly conductive zone beneath the Puna could reach depths larger than 80 km, it implies that the processes originating this anomaly could have their source in the asthenospheric wedge (see later discussion).

In order to feed a volcanic arc, significant melting must occur in the wedge, which implies a minimum temperature of $\sim$1300° (Schmidt and Poli, 1998). For a basaltic to tholeiitic melt composition at 1300°C, one may assume a melt conductivity of σ_m = 5.5-6.5 S/m, resulting in a melt fraction estimate of 21-25 vol.%, following Brasse and Eydam (2008), who obtained bulk conductivities inside the wedge core on the order of 1 S/m. However, this value is for dry magmas, which are not very frequent in subduction zones, where a strong influence of water is expected.

A large amount of water is carried by the subducting slab in form of hydrated sediments, basalt or mantle lithosphere, and even when is widely accepted that arc volcanism is initiated through partial melting of a mantle wedge, which is strongly influenced by dehydration of subducted crust, the study of the processes through which this water is transported from the slab is a difficult and not completely resolved task (van Keken, 2003).

According to Grove et al. (2006) serpentinized mantle lithosphere underlying the top-most sediment and basalt layers of subducted lithosphere can be an important reservoir that fuels vapor-saturated flux melting, while chlorite-bearing hydrated mantle above the slab may also carry H_2O into the melt generation zone. If the subducted basalt or sediment is heated sufficiently, melting will occur, resulting in a siliceous and H_2O rich melt which would encounter solid mantle as it ascends into the overlying wedge. The influence of H_2O on melting is characterized by a large temperature lowering effect that enlarges the temperature interval over which melting occurs.

In order to estimate the water and melt rates in the wedge several models have been proposed (e.g. Grove et al. (2006); Iwamori (1998)), with temperature distributions which depend on the age and speed of the subducting slab as well as on the subduction geometry. For Grove et al. (2006), water content may even increase to 30 wt% for first magmas near the slab, while the maximum amount of melting (10-15 wt %) occurs in the hot core of the mantle wedge, increasing above 18% according to Iwamori (1998), where the wedge attains its maximum temperature.

The water supply enhances the melt conductivity considerably, according to studies in dry and hydrous silicic melts (Gaillard, 2004), which is interpreted as the effect of water on sodium mobility. Additionally higher temperatures or saline brines may further increase conductivity and thus reduce melt rate. For instance, a hotter wedge (1400°C) implies a σ_m of 11.5 S/m for tholeiitic melt, yielding a value of 12.5 vol.% (Brasse and Eydam, 2008).

Thus, the main cause of the high conductivity anomaly beneath the Puna should be the presence of partial melts caused by the ascending fluids, but why is this anomaly placed beneath the backarc instead of below the main volcanic arc?

At 24°S, ∼40 km south of the LMT profile, above the westernmost high attenuation zone shown in the southern cross-section of figure 6.10 stands the Quaternary strato-volcano Cerro Tuzgle. In its vicinity, shoshonites as well as ocean-island-type basalts and ignimbrites occur. Coira and Kay (1993) concluded that both Cerro Tuzgle and the shoshonites were derived from mantle magmas and that the Tuzgle magmas were also contaminated by mixing with crustal melts in the lower crust. According to Schurr et al. (2006) this volcanism is the result of a recent detachment of lithosphere, the remains of which are now lying on top of the Nazca plate, while fluids may ascend from the earthquake cluster at 200 km depth, beneath the highly conductive zone (as shown in figure 6.11), through the mantle, and triggering mantle melting responsible for the observed andesitic magmatism.

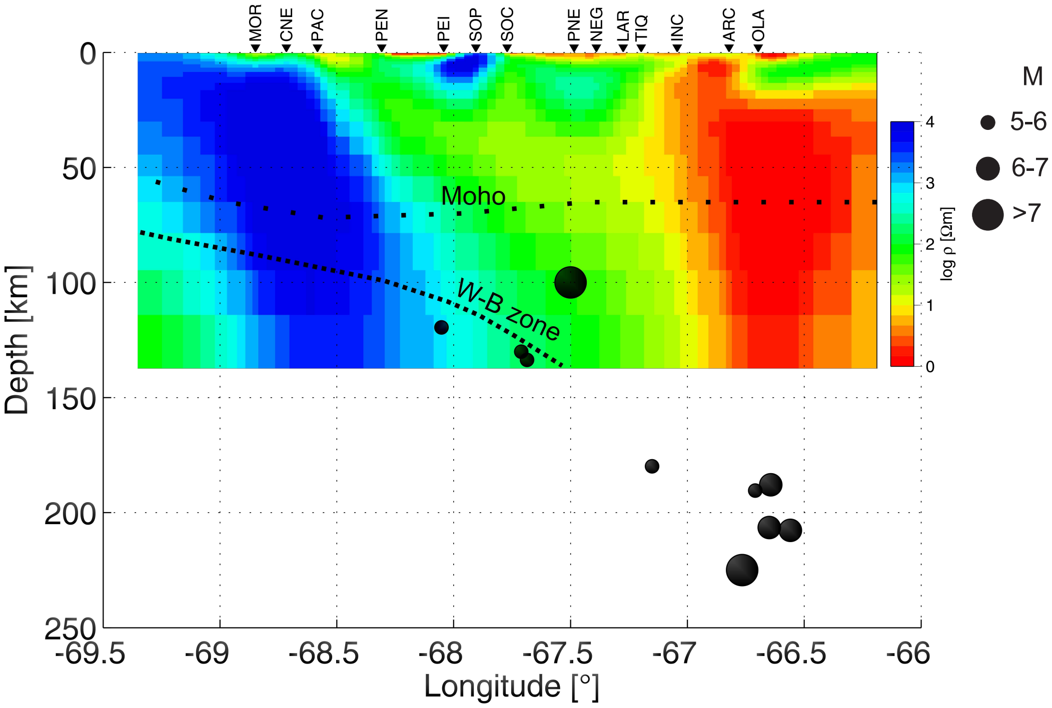

Figure 6.11: 2D inversion result of the LMT profile, and earthquakes locations between 23.5°S and 24°S, from Engdahl and Villaseñor (2002). Resistivity structures beneath 140 km are not resolved and thus not shown in this section.

The idea of a common source for forearc and backarc magmas does not agree with geochemical differences between the frontal arc and backarc volcanoes at this latitude (Schurr et al., 2003), but the presence of a high attenuation zone beneath the present volcanic arc, together with a relatively conductive zone in the same area (D’ in figure 6.9) could indicate a second magma generation zone, fed by fluids from the slab, and from the deeper easternmost magma generation zone associated with the largest earthquake cluster. This could explain why we are observing the volcanic arc in its actual position, and not above the anomalies observed in the backarc. One can also speculate, as the attenuation and conductive anomalies, together with the seismological data for this area are clearly pointing to the presence of fluids and a magma generation zone beneath the Puna, that this is a snapshot of a new eastward migration of the volcanic arc, as has already occurred several times since the Jurassic.

Chapter 7

Conclusions and comments

After a dimensionality analysis performed for both datasets in the study area, a clear geoelectrical strike together with phase tensor, tipper and skew values in agreement with a 2D supposition were obtained for the LMT profile's data, while no clear two-dimensionality indicators were obtained for the broadband magnetotelluric data measured in the vicinity of Lascar volcano. These results yield to the validity of a 2D inversion obtained with the LMT data, and the necessity of a 3D model to explain the data in the surroundings of the volcano.

Several 3D models were obtained for the area around Lascar volcano, modeling also the topography around each measuring station, and performing forward modeling with different conductivity scenarios. Some features needed by the magnetotelluric data were a resistive and relatively shallow block at the eastern border of the Salar de Atacama, associated with intrusives present in the Cuyuguas and Allana hills, and some other shallow conductivities, associated with the Aguas Calientes salar, to the east of Lascar volcano, and conductive zones close to the volcano itself, possibly associated with hydrothermal fluids.

Conductive zones with different shapes and sizes were set at various depths beneath the volcanic edifice, in order to check the presence of a magma chamber beneath it, but no single conductive zone beneath the volcano could explain the magnetotelluric responses of the stations around it. However, models including a conductive zone extending to the south-southeast of the volcano improved strongly the fit with the measured data, particularly for the tipper, but also for apparent resistivities and phases at most of the stations. This conductive zone is located in the middle of several volcanic centers, limited to the north by Lascar and Aguas Calientes volcanoes, and to the south by the Puntas Negras volcanic chain and Chiliques volcano, the location of which is particularly interesting considering its proximity and indicators of recent activity during the last years.

2D inversions of the long-period transect were obtained using a non-linear conjugate gradients algorithm, which agreed with the main geotectonical features expected for this area. The subducting slab together with a crustal block coinciding with the Domeyko Cordillera were modeled as highly resistive zones, while the Salar de Atacama, extending a few kilometers in depth, was resolved as a very conductive area, which agrees with in-situ conductivity measurements. A large highly conductive anomaly ($\sim$ 1 Ωm) was obtained beneath the Puna, starting at 10 - 20 km depth, and probably extending through the Moho. The presence of such an anomaly fits well with previous conductivity models obtained beneath the Altiplano (Brasse et al., 2002; Brasse and Eydam, 2008). A relatively conductive anomaly (20 - 30 Ωm) was also obtained below the active volcanic arc at depths between 10 - 30 km. These conductive anomalies, both associated with seismicity clustered beneath them, are possibly related to dehydration processes of the subducting slab which enhances the formation of magmas in the ascending paths of fluids through the mantle wedge. The presence of these anomalies beneath the arc and the backarc agrees also with seismic tomography results in this area. The larger and more conductive anomaly located beneath the plateau is possibly related to the processes originating the young monogenetic volcanic centers associated with mafic lavas in the Puna, such as Tuzgle volcano and shoshonitic lavas. They are derived from the ascent of the mantle material, contaminated by mixing with crustal melts in the lower crust, according to Coira and Kay (1993), coinciding with the depth extent and location of the larger anomaly. Speculatively, the observation of a larger and more conductive anomaly located beneath the backarc instead of beneath the main volcanic arc in the Western Cordillera, could be a snapshot of the eastward migration of the arc, as it has occurred already several times since the Jurassic.

The presence of a highly conductive zone beneath the Puna, as well as in the northern part of the plateau, beneath the Altiplano, suggest that this feature is common to almost the entire plateau, but showing some remarkable differences beneath the Altiplano and the Puna. Beneath the Altiplano, this highly conductive zone is starting at larger depths and is also extending until $\sim$120 km, while beneath the Puna this feature is starting and probably finishing at shallower depths. The different depth extensions of the highly conductive zones beneath the two segments of the plateau can be associated with a thinner lithosphere beneath the Puna, which is approximately 50 km thicker beneath the Altiplano (Whitman et al., 1992), and therefore with the morphological differences observed between the higher and narrower Puna and the lower, wider and thick-crusted Altiplano.

References

Allmendinger, R. W., Jordan, T. E., Kay, S. M., and Isacks, B. L. (1997). The evolution of the Altiplano-Puna plateau of the Central Andes. *Annu. Rev. Earth Planet. Sci.*, 25:139–174.

Aron, F., González, G., Veloso, E., and Cembrano, J. (2008). Architecture and style of compressive Neogene deformation in the eastern-southeastern border of the Salar de Atacama Basin (22°30’-24°15’s): A structural setting for the active volcanic arc of the Central Andes. *7th International Symposium on Andean Geodynamics (ISAG 2008, Nice)*, Extended Abstracts:52–55.

Arriagada, C., Cobbold, P. R., Mpodozis, C., and Roperch, P. (2002). Cretaceous to Paleogene compressional tectonics during the deposition of the Purilactis group, Salar de Atacama. *Proc. V IRD-ISAG, Tolouse*, pages 41–44.

Asch, G., Schurr, B., Bohm, M., Yuan, X., Haberland, C., Heit, B., Kind, R., Woelbern, I., Bataille, K., Comte, D., Pardo, M., Viramonte, J., Rietbrock, A., and Giese, P. (2006). Seismological Studies of the Central and Southern Andes. *The Andes: Active Subduction Orogeny*, pages 443–457. Oncken et al. (editors), Frontiers in Earth Sciences, Springer-Verlag, Berlin.

Asters, R. C., Borchers, B., and Thurber, C. H. (2005). Parameter Estimation and Inverse Problems. *Int. Geophys. Ser.*, 90. Elsevier Academic Press.

Bahlburg, H. and Breitkreuz, C. (1991). Paleozoic evolution of active margin basins in the southern Central Andes (northwestern Argentina and northern Chile). *J. South Amer. Earth Sci.*, 4:171–188.

Bahr, K. (1988). Interpretation of the magnetotelluric impedance tensor: regional induction and local telluric distortion. *J. Geophys.*, 62:119–127.

Bahr, K. (1991). Geological noise in magnetotelluric data: a classification of distortion types. *Phys. Earth Planet. Inter.*, 66:24–38.

Beck, M. (1988). Analysis of late Jurassic-Recent paleomagnetic data from active plate margins of South America. *J. South Amer. Earth Sci.*, 1:39–52.

Brasse, H. and Eydam, D. (2008). Electrical conductivity beneath the Bolivian Orocline and its relation to subduction processes at the South American continental margin. *J. Geophys. Res.*, 113. B07109, doi: 10.1029/2007JB005142.

Brasse, H., Kapinos, G., Li, Y., Mütschard, L., Soyer, W., and Eydam, D. (2009). Structural electrical anisotropy in the crust at the South-Central Chilean continental margin as inferred from geomagnetic transfer functions. *Phys. Earth Planet. Inter.*, 173:7–16.

Brasse, H., Lezaeta, P., Rath, V., Schwalenberg, K., Soyer, W., and Haak, V. (2002). The Bolivian Altiplano conductivity anomaly. *J. Geophys. Res.*, 107. B5, doi: 10.1029/2001JB000391.

Breitkreuz, C. and van Schmus, W. R. (1996). U−−Pb geochronology and significance of Late Permian ignimbrites in Northern Chile. *Journal of South American Earth Sciences*, 9:281–293.

Breitkreuz, C. and Zeil, W. (1994). The Late Carboniferous to Triassic Volcanic Belt in Northern Chile. *Tectonics of the Southern Central Andes*, pages 277–292. Reutter, K.-J., Scheuber, E. and Wigger, P.J., editors. Springer-Verlag, Berlin.

Cagniard, L. (1953). Basic theory of the magneto-telluric method of geophysical prospecting. *Geophysics*, 18:605–635.

Cahill, T. and Isacks, B. (1992). Seismicity and Shape of the Subducted Nazca Plate. *J. Geophys. Res.*, 97:17503–17529. B12, doi: 10.1029/92JB00493.

Caldwell, T. G., Bibby, H. M., and Brown, C. (2004). The magnetotelluric phase tensor. *Geophys.J.Int.*, 158:457–469.

Chave, A. D. and Smith, J. T. (1994). On electric and magnetic galvanic distortion tensor decompositions. *J. Geophys. Res.*, 99(B3):4669–4682.

Coira, B. and Kay, S. (1993). Implications of Quaternary volcanism at Cerro Tuzgle for crustal and mantle evolution of the Puna Plateau, Central Andes, Argentina. *Contrib. Mineral. Petrol.*, 113:40–58.

David, C., Martinod, J., Comte, D., Herail, G., and Haessler, H. (2002). Intracontinental seismicity and Neogene deformation of the Andean forearc in the region of Arica (18.58°s-19.58°s). *5th International Symposium of Andean Geodynamics, (ISAG 2002, Toulouse)*, pages 171–174.

De Silva, S. L. (1989). Altiplano-Puna volcanic complex of the Central Andes. *Geology*, 17:1102–1106.

de Silva, S. L. and Francis, P. W. (1991). Volcanoes of the central andes. Springer-Verlag.

DeMets, C., Gordon, R. G., Argus, D. F., and Stein, S. (1990). Current plate motions. *Geophys. J. Int.*, 101:425–478.

DeMets, C., Gordon, R. G., Argus, F., and Stein, S. (1994). Effect of recent revisions of the geomagnetic timescale on estimates of current plate motions. *Geophys. Res. Lett.*, 21:2191–2194.

Donoso, C. L., Aguilera, F. A., and Medina, E. (2005). Geology and petrology of the Corona and cerros de Saltar domes near the Lascar volcano system, Northern Chile. *6th International Symposium on Andean Geodynamics (ISAG 2005, Barcelona),* Extended Abstracts:230–233.

Echternacht, F., Tauber, S., Eisel, M., Brasse, H., Schwarz, G., and Haak, V. (1997). Electromagnetic study of the active continental margin in northern Chile. *Phys. Earth Planet. Inter.*, 102:69–87.

Egbert, G. D. and Booker, J. R. (1986). Robust estimation of geomagnetic transfer functions. *Geophys. J. R. astr. Soc.*, 87:173–194.

Engdahl, E. R. and Villaseñor, A. (2002). Global seismicity: 1900–1999. *Int. Handbook of Earthquake and Engineering Seismology*, 81A:665–690.

Farías, M., Charrier, R., Comte, D., Martinod, J., and Hérail, G. (2005). Late Cenozoic deformation and uplift of the western flank of the Altiplano: Evidence from the depositional, tectonic, and geomorphologic evolution and shallow seismic activity (northern Chile at 19°30’s). *Tectonics*, 24. TC4001, doi: 10.1029/2004TC001667.

Farias, M., Charrier, R., Comte, D., Martinod, J., Pinto, L., and Hérail, G. (2002). Active Late Cenozoic flexures in the Precordillera in northern Chile: Correlations with the shallow seismic activity, and implications for the uplift of the Altiplano. *Eos Trans.* AGU, 83(47), Fall Meet. Suppl. Abstract T51A-1136.

Flint, S., Turner, P., Jolley, E., and Hartley, A. (1993). Extensional tectonics in convergent margin basins: an example from the Salar de Atacama, Chilean Andes. *Geol. Soc. Amer. Bull.*, 105:603–617.

Gaillard, F. (2004). Laboratory measurements of electrical conductivity of hydrous and dry silicic melts under pressure. *Earth Planet. Sci. Lett.*, 218:215–228.

Gamble, T. D., Goubau, W. M., and Clarke, J. (1979). Magnetotelluric with a remote magnetic reference. *Geophysics*, 44:53–68.

Gangui, A. H. (1998). A combined structural interpretation based on seismic data and 3-D gravity modelling in the northern Puna/Eastern Cordillera, Argentina. *Ph.D. thesis*. Freie Universität Berlin, Berlin.

García, M., Hérail, G., Charrier, R., Mascle, G., Fornari, M., and Perez de Arce, C. (2002). Oligocene-Neogene tectonic evolution of the Altiplano of northern Chile (18-19°s). *5th International Symposium of Andean Geodynamics, (ISAG 2002, Toulouse)*, pages 235–238.

Gardeweg, M., Pino, H., Ramírez, C. F., and Davidson, J. (1994). Mapa Geológico del área de Imilac y Sierra de Almeida, Región de Antofagasta. Servicio Nacional de Geología y Minería, Documentos de Trabajo No. 7, escala 1:100.000. Santiago, Chile.

Gardeweg, M. and Ramírez, C. F. (1987). La Pacana caldera and the Atana Ignimbrite - A major ash-flow and resurgent caldera complex in the Andes of northern Chile. *Bull. Volcanol.*, 49:547–566.

Gardeweg, M., Sparks, S., and Matthews, S. (1998). Evolution of lascar volcano, northern chile. *Jour. Geol. Soc. London*, 155:89–104.

González, G., Cembrano, J., Aron, F., Veloso, E. E., and Shyu, J. B. H. (2009). Coeval compressional deformation and volcanism in the central Andes, case studies from northern Chile (23°sŰ24°s). *Tectonics*, 28. TC6003, doi:10.1029/2009TC002538.

Graeber, F. and Asch, G. (1999). Three dimensional models of P wave velocity and P to S velocity ratio in the southern Central Andes by simultaneous inversion of local earthquake data. *J. Geophys. Res.*, 104:20237–20256.

Groom, R. W. and Bahr, K. (1992). Corrections for near surface effects: Decomposition of the magnetotelluric impedance tensor and scaling corrections for regional resistivities: a tutorial. *Surv. Geophys.*, 13:341–379.

Groom, R. W. and Bailey, R. C. (1989). Decomposition of magnetotelluric impedance tensor in the presence of local three-dimensional galvanic distortion. *J. Geophys. Res.*, 94:1913–1925.

Grove, T. L., Chatterjee, N., Parman, S. W., and Médard, E. (2006). The influence of h_2o on mantle wedge melting. *Earth Planet. Sci. Lett.*, 249:74–89.

Götze, H. J., Lahmeyer, B., Schmidt, S., and Strunk, S. (1994). The lithospheric structure of the Central Andes (20-26°S) as inferred from interpretation of regional gravity. *Tectonics of the Southern Central Andes*, pages 7–21. Reutter, K.-J., Scheuber, E. and Wigger, P.J., editors. Springer-Verlag, Berlin.

Gutscher, M. A., Malavieille, J., Lallemand, S., and Collot, J. Y. (1999). Tectonic segmentation of the North Andean margin: impact of the Carnegie ridge collision. *Earth Planet. Sci. Lett.*, 168:255–270.

Gutscher, M. A., Spakman, W., Bijwaard, H., and Engdahl, E. R. (2000). Geodynamics of flat subduction: Seismicity and tomographic constraints from the Andean margin. *Tectonics*, 19:814–833.

Heise, W., Caldwell, T. G., Bibby, H. M., and Bannister, S. C. (2008). Three-dimensional modelling of magnetotelluric data from Rotokawa geothermal field, Taupo Volcanic Zone, New Zealand. *Geophys. J. Int.* 10.1111/j.1365-246X.2008.03737.x.

Hellweg, M. (1999a). Listening carefully: unique observations of harmonic tremor at Lascar volcano, Chile. *Annali di Geofisica*, 42:451–464.

Hellweg, M. (1999b). Seismic signals from Lascar Volcano. *Journal of South American Earth Sciences*, 12:123–133.

Hellweg, M. (2000). Physical models for the source of Lascar's harmonic tremor. *Journal of Volcanology and Geothermal Research*, 101:183–198.

Hill, G., Caldwell, T. G., Heise, W., Chertkoff, D. G., Bibby, H. M., Burgess, M. K., Cull, J. P., and Cas, R. A. F. (2009). Distribution of melt beneath mount st helens and mount adams inferred from magnetotelluric data. *Nature Geosciences*. doi: 10.1038/NGEO661.

Huber, P. J. (1981). Robust statistics. Wiley, New York, NY.

Ingham, M. R., Bibby, H. M., Heise, W., Jones, K. A., Cairns, P., Dravitzki, S., Bennie, S. L., Caldwell, T. G., and Ogawa, Y. (2009). A Magnetotelluric study of Mount Ruapehu volcano, New Zealand. *Geophys. J. Int.*, 179:887–904.

Isacks, B. L. (1988). Uplift of the central Andean plateau and bending of the Bolivian Orocline. *J. Geophys. Res.*, 93:3211–3231.

Iwamori, H. (1998). Transportation of h_2o and melting in subduction zones. *Earth Planet. Sci. Lett.*, 160:65–80.

Jiracek, G. R. (1990). Near-surface and topographic distortions in electromagnetic induction. *Surv. Geophys.*, 11:163–203.

Kendrick, E., Bevis, M., Smalley, R., Brooks, B., Barriga-Vargas, R., Lauria, E., and Souto-Fortes, L. P. (2003). The Nazca-South America Euler vector and its rate of change. *Journal of South American Earth Sciences*, 16:125–131.

Kuhn, D. (2002). Fold and thrust belt structures and strike-slip faulting at the SE margin of the Salar de Atacama basin, Chilean Andes. *Tectonics*. 21(4), 1026, doi:10.1029/2001TC901042.

Lamb, S., Hoke, L., Kennan, I., and Dewey, J. (1997). Cenozoic evolution of the central Andes in Bolivia and northern Chile. *Orogeny Through Time*, 121:237–264. edited by J-P. Burg and M. Ford, Geol. Soc. Spec. Publ.

Lezaeta, P. (2001). Distortion analysis and 3-D modeling of magnetotelluric data in the southern Central Andes. *Ph.D. thesis*. Fachber. Geowiss., Freie Univ. Berlin, Berlin.

Lezaeta, P. and Brasse, H. (2001). Electrical conductivity beneath the volcanoes of the NW Argentinian Puna. *Geophys. Res. Lett.*, 28:4651–4654.

Lezaeta, P., Muñoz, M., and Brasse, H. (2000). Magnetotelluric image of the crust and upper mantle in the backarc of the northwestern Argentinean Andes. *Geophys. J. Int.*, 142:841–854.

Lindsay, J. M., Schmitt, A. K., Trumbull, R. B., De Silva, S. L., Siebel, W., and Emmermann, R. (2001). Magmatic evolution of the La Pacana Caldera system, Central Andes, Chile: compositional cariation of two cogenetic, large-volume felsic ignimbrites. *Journal of Petrology*, 42:459–486.

MacFadden, B. J., Anaya, F., and Swisher III, C. (1995). Neogene paleomagnetism and oroclinal bending of the central Andes of Bolivia. *J. Geophys. Res.*, 100:8153–8167.

Mackie, R. L., Smith, J. T., and Madden, T. R. (1994). Three-dimensional electromagnetic modeling using finite difference equations: The magnetotelluric example. *Radio Science*, 29:923–935.

Marret, R. A., Allmendinger, R. W., Alonso, R. N., and Drake, R. E. (1994). Late Cenozoic tectonic evolution of the Puna Plateau and adjacent foreland, northwestern Argentine Andes. *Journal of South American Earth Sciences*, 7:179–207.

Matsushima, N., Oshima, O., Ogawa, Y., Takakura, S., Satoh, H., Utsugi, M., and Nishida, Y. (2001). Magma prospecting in Usu volcan, Hokkaido, Japan, using magnetotelluric soundings. *Journal of Volcanology and Geothermal Research*, 109:263–277.

Matteini, M., Mazzuoli, R., Omarini, R., Cas, R., and Maas, R. (2002a). The geochemical variations of the upper cenozoic volcanism along the Calama-Olacapato-El Toro transversal fault system in central Andes ($\sim$24°S): petrogenetic and geodynamic implications. *Tectonophysics*, 345:211–227.

Matteini, M., Mazzuoli, R., Omarini, R., Cas, R., and Maas, R. (2002b). Geodynamical evolution of central andes at 24°S as inferred by magma composition along the Calama-Olacapato-El Toro transversal volcanic belt. *Journal of Volcanology and Geothermal Research*, 118:205–228.

Matthews, S. J., Gardeweg, M. C., and Sparks, R. S. J. (1997). The 1984 to 1996 cyclic activity of Lascar Volcano, northern Chile: cycles of dome growth, dome subsidence, degassing and explosive eruptions. *Bull. Volcanol.*, 59:72–82. doi: 10.1007/s004450050176.

Müller, A. and Haak, V. (2004). 3-D modelling of the deep electrical conductivity of Merapi volcano (Central Java): integrating magnetotellurics, induction vectors and the effects of steep topography. *Journal of Volcanology and Geothermal Research*, 138:205–222.

Mpodozis, C., Arriagada, C., Basso, M., Roperch, P., Cobbold, P., and Reich, M. (2005). Late Mesozoic to Paleogene stratigraphy of the Salar de Atacama Basin, Antofagasta, Northern Chile: Implications for the tectonic evolution of the Central Andes. *Tectonophysics*, 399:125–154.

Mpodozis, C., Marinovic, N., Smoje, I., and Cuitiño, L. (1993). Estudio Geológico-Estructural de la Cordillera de Domeyko entre Sierra Limón Verde y Sierra Mariposas, Región de Antofagasta. *Serv. Nac. Geol. Min.*, IR 93-04.

Mpodozis, C. and Ramos, V. (1989). The Andes of Chile and Argentina. *Geology of the Andes and its relation to hidrocarbon and mineral resources*, 11:59–90. (Ericksen, G.E.; Cañas, M.T.; Reinemund, J.; editors). Circum-Pacific Council for Energy and Mineral Resources, Earth Sciences Series.

Muñoz, N. and Charrier, R. (1996). Uplift of the western border of the Altiplano on a west-vergent thrust system, Northern Chile. *J. South Amer. Earth Sci.*, 9:171–181.

Muñoz, N., Charrier, R., and Jordan, T. (2002). Interactions between basement and cover during the evolution of the Salar de Atacama Basin, northern Chile. *Revista geológica de Chile*, 29:55–80.

Muñoz, N., Charrier, R., and Reutter, K. J. (1997). Evolución de la cuenca del Salar de Atacama: Inversión tectónica y relleno de una cuenca de antepaís de retroarco. *Proc. VIII Congr. Geol. Chileno*, 1:195–199.

Norabuena, E., Leffler-Griffin, L., Mao, A., Dixon, T., Stein, S., Sacks, I., Ocala, L., and Ellis, M. (1998). Space geodetic observations of Nazca-South America convergence across the Central Andes. *Science*, 279:358–362.

Oncken, O., Hindle, D., Kley, J., Elger, K., Victor, P., and Schemmann, K. (2006). Deformation of the Central Andean Upper Plate System - Facts, Fiction, and Constraints for Plateau Models. *The Andes: Active Subduction Orogeny*, pages 3–27. Oncken et al. (editors), Frontiers in Earth Sciences, Springer-Verlag, Berlin.

Oppenheimer, C., Francis, P. W., Rothery, D. A., and Carlton, R. W. T. (1993). Infrared image analysis of volcanic thermal features: Lascar Volcano, Chile. *J. Geophys. Res.*, 98:4269–4286.

Pardo-Casas, F. and Molnar, P. (1987). Relative motion of the Nazca (Farallon) and South American plates since Late Cretaceous time. *Tectonics*, 6:233–248.

Pavez, A., Remy, D., Bonvalot, S., Diament, M., Gabalda, G., Froger, J.-L., Julien, P., Legrand, D., and Moisset, D. (2006). Insight into ground deformations at Lascar volcano (Chile) from SAR interferometry, photogrammetry and GPS data: Implications on volcano dynamics and future space monitoring. *Remote Sensing of Environment*, 100:307–320.

Petrinovic, I. A., Arnosio, J. M., Alvarado, G. E., and Guzmán, S. (2005). Erupciones freáticas sintectónicas en el campo geotérmico de Tocomar, Salta. *Revista de la Asociación Geológica Argentina*, 60:132–141.

Putirka, K. D. (2008). Thermometers and barometers for volcanic systems. *Reviews in Mineralogy and Geochemistry*, 69:61–120.

Ramírez, R. and Gardeweg, M. (1982). Hoja Toconao, Región de Antofagasta. Carta Geológica de Chile, 1:250000. Servicio Nacional de Geología y Minería de Chile, Santiago.

Randall, D. E., Taylor, G. K., and Grocott, J. (1996). Major crustal rotations in the Andean margin: Palaeomagnetic results from the Coastal Cordillera of northern Chile. *J. Geophys. Res.*, 101:783–798.

Reutter, K. J., Charrier, R., Götze, H. J., Schurr, B., Wigger, P., Scheuber, E., Giese, P., Reuther, C. D., Schmidt, S., Rietbrock, A., Chong, G., and A., B.-P. (2006). The Salar de Atacama Basin: a Subsiding Block within the Western Edge of the Altiplano-Puna Plateau. *The Andes: Active Subduction Orogeny*, pages 303–325. Oncken et al. (editors), Frontiers in Earth Sciences, Springer-Verlag, Berlin.

Riller, U. and Oncken, O. (2003). Growth of the Central Andean Plateau by Tectonic Segmentation Is Controlled by the Gradient in Crustal Shortening. *The Journal of Geology*, 111:367–384.

Riller, U., Petrinovic, I., Ramelow, J., Strecker, M., and Oncken, O. (2001). Late cenozoic tectonism, collapse caldera and plateau formation in the central Andes. *Earth Planet. Sci. Lett.*, 188:299–311.

Rodi, W. and Mackie, R. L. (2001). Nonlinear conjugate gradients algorithm for 2-D magnetotelluric inversions. *Geophysics*, 66:174–187.

Salfity, J. A. (1985). Lineamientos transversales al rumbo andino en el noroeste argentino. *IV Congreso Geologico Chileno*, Acta 2:119–137.

Scheuber, E., Mertmann, D., Harald, E., Silva-Gonzalez, P., Heubeck, C., Reutter, K. J., and Jacobshagen, V. (2006). Exhumation and basin development related to formation of the central andean plateau, 21°S. *The Andes: Active Subduction Orogeny*, pages 285–301. Oncken et al. (editors), Frontiers in Earth Sciences, Springer-Verlag, Berlin.

Scheuber, E. and Reutter, K. J. (1992). Magmatic arc tectonics in the Central Andes between 21° and 25°s. *Tectonophysics*, 205:127–140.

Schilling, F. R., Partzsch, G. M., Brasse, H., and Schwarz, G. (1997). Partial melting below the magmatic arc in the central Andes deduced from geoelectromagnetic field experiments and laboratory data. *Phys. Earth Planet. Inter.*, 103:17–31.

Schilling, F. R., Trumbull, R. B., Brasse, H., Haberland, C., Asch, G., Bruhn, D., Mai, K., Haak, V., Giese, P., Muñoz, M., Ramelow, J., Rietbrock, A., Ricaldi, E., and Vietor, T. (2006). Partial Melting in the Central Andean Crust: a Review of Geophysical, Petrophysical, and Petrologic

Evidence. *The Andes: Active Subduction Orogeny*, pages 459–474. Oncken et al. (editors), Frontiers in Earth Sciences, Springer-Verlag, Berlin.

Schmidt, M. W. and Poli, S. (1998). Experimentally based water budgets for dehydrating slabs and consequences for arc magma generation. *Earth Planet. Sci. Lett.*, 163:361–379.

Schmitz, M., Lessel, K., Giese, F., Wigger, P., Araneda, M., Bribach, J., Graeber, F., Grunewald, S., Haberland, C., Lüth, S., Röber, F., Ryberg, T., and Schulze, A. (1999). The crustal structure beneath the Central Andean forearc and magmatic arc as derived from seismic studies - the PISCO 94 experiment in northern Chile (21°- 23°s). *J. South Amer. Earth Sci.*, 12:237–260.

Schurr, B., Asch, G., Rietbrock, A., Trumbull, R., and Haberland, C. (2003). Complex patterns of fuid and melt transport in the central Andean subduction zone revealed by attenuation tomography. *Earth Planet. Sci. Lett.*, 215:105–119.

Schurr, B. and Rietbrock, A. (2004). Deep seismic structure of the Atacama Basin, Northern Chile. *Geophys. Res. Lett.* 31, L12601, doi: 10.1029/2004GL019796.

Schurr, B., Rietbrock, A., Asch, G., Kind, R., and Oncken, O. (2006). Evidence for lithospheric detachment in the central Andes from local earthquake tomography. *Tectonophysics*, 415:203–223.

Schwalenberg, K., Rath, V., and Haak, V. (2002). Sensitivity studies applied to a two-dimensional resistivity model from the Central Andes. *Geophys. J. Int.*, 150:673–686.

Sims, W. E., Bostick, F. X., and Smith, H. W. (1971). The estimation of magnetotelluric impedance tensor elements from measured data. *Geophysics*, 36:938–942.

Singer, B. S. (1992). Correction for distortions of magnetotelluric fields: limits of validity of the static approach. *Surv. Geophys.*, 13:309–340.

Siripunvaraporn, W. and Egbert, G. (2000). An efficient data-subspace inversion method for 2-D magnetotelluric data. *Geophysics*, 65:791–803.

Siripunvaraporn, W., Egbert, G., Lenbury, Y., and Uyeshima, M. (2005). Three-dimensional magnetotelluric inversion: data-space method. *Phys. Earth Planet. Inter.*, 50:3–14.

Smith, J. T. (1995). Understanding telluric distortion matrices. *Geophys. J. Int*, 122:219–226.

Somoza, R. (1998). Updated Nazca (Farallon)-South America relative motions during the last 40 My: implications for mountain building in the central Andean region. *Journal of South American Earth Sciences*, 11:211–215.

Swift, C. M. (1967). A Magnetotelluric Investigation of an Electrical Conductivity Anomaly in the Southwestern United States. *PhD thesis*. Massachusetts Institute of Technology, Cambridge, Massachusetts, USA.

Tikhonov, A. N. (1950). The determination of the electrical properties of deep layers of the earth's crust. *Dokl. Akad. Nauk.*, SSR 73:295–297.

Tikhonov, A. N. and Berdichevsky, M. N. (1966). Experience in the use of magnetotelluric methods to study the geological structures of sedimentary basins. *Izv. Acad. Sci. USSR Phys. Solid Earth Eng. transl.*, 2:34–41.

Utada, H. and Munekane, H. (2000). On galvanic distortion of three dimensional magnetotelluric impedances. *Geophys. J. Int.*, 140:385–398.

van Keken, P. E. (2003). The structure and dynamics of the mantle wedge. *Earth Planet. Sci. Lett.*, 215:323–338.

Victor, P., Oncken, O., and Glodny, J. (2004). Uplift of the western Altiplano plateau: Evidence from the Precordillera between 20° and 21°s (northern Chile). *Tectonics*, 23. TC4004, doi:10.1029/2003TC001519.

Whitman, D., Isacks, B. L., Chatelain, J. L., Chiu, J. M., and Perez, A. (1992). Attenuation of high-frequency seismic waves beneath the central Andean plateau. *J. Geophys. Res.*, 97:19929–19947.

Whitman, D., Isacks, B. L., and M., K. S. (1996). Lithospheric structure and along-strike segmentation of the central andean plateau: Topography, tectonics, and timing. *Tectonophysics*, 259:29–40.

Wörner, G., Hammerschmidt, K., Henjes-Kunst, F., Lezaun, J., and Wilke, H. (2000). Geochronology (^{40}ar/^{39}ar, k-ar and he-exposure ages) of Cenozoic magmatic rocks from Northern Chile (18-22°s): implications for magmatism and tectonic evolution of the central Andes. *Revista Geológica de Chile*, 27:205–240.

Yañez, G. and Cembrano, J. (2004). Role of viscous plate coupling in the late tertiary andean tectonics. *J. Geophys. Res.*, 109. B02407, doi: 10.1029/2003JB002494.

Yuan, X., Sobolev, S. V., Kind, R., Oncken, O., Bock, G., G., A., Schurr, B., Graeber, F., Rudloff, A., Hanka, W., Wylegalla, K., Tibi, R., Haberland, C., Rietbrock, A., Giese, P., Wigger, P., Röwer, P., Zandt, G., Beck, S., Wallace, T., Pardo, M., and Comte, D. (2000). Subduction and collision processes in the Central Andes constrained by converted seismic phases. *Nature*, 408:958–961.

List of Figures

1.1 Main structures characterizing the Central Andes. Red stars show the location of magnetotelluric profiles (A, B, C and D) in the Central Andes, with results described in: A) Brasse and Eydam (2008); B) Echternacht et al. (1997); Lezaeta (2001); C) Lezaeta (2001); Brasse et al. (2002); Schwalenberg et al. (2002); D) this work. Lines C1 and C2 are planned profile prolongations for future field campaigns. Red triangle indicates the position of Lascar volcano, and the dashed rectangle the location of figure 1.2. 9

1.2 Study zone and location of sites. Green triangles are AMT stations and blue squares are LMT stations. 10

2.1 Variation of the Wadati-Benioff plane in the Central Andes and bathymetric-topographic profiles (Yañez and Cembrano, 2004) 13

2.2 Location map showing the extent of the high plateau of the Central Andes. Dark gray shows area above 3 km elevation; the plateau is defined by the wide area above 3 km between 13 and 27°S. The light gray zones are thin-skinned thrust belts in the Subandean ranges of Bolivia/Peru and the Precordillera (PC) in Argentina. The Sierras Pampeanas and Santa Barbara System (SB) are thick-skinned foreland provinces. The hachured zone trending NW-SE across the Argentine-Bolivian border corresponds to a variety of lateral change in Andean and pre-Andean features, and can be considered as the Altiplano-Puna boundary (Allmendinger et al., 1997). 14

2.3 Structural map of the Salar de Atacama area showing some of the first and second order faults controlling the structural style of this area. Extracted from Aron et al. (2008). 16

2.4 Topography, residual gravity, and interpretational cross section through the Salar de Atacama basin at 23.2°S. Abbreviations are as follows: PC - Precordillera, PCFS - Precordilleran fault system, AD - Salar de Atacama depression, AB - Atacama block, WC - Western Cordillera (extracted and edited from Schurr and Rietbrock (2004)). 18

2.5 Geological map of the area east of Salar de Atacama, from Breitkreuz and Zeil (1994). A, B and C represent 3 zones to the E of the Salar de Atacama, as shown in the leftmost image. 20

2.6 Aerial photograph of the active area of Lascar volcano acquired in 1998 (extracted and edited from Pavez et al. (2006)). 22
2.7 Geology around Lascar volcano (Gardeweg et al., 1998) showing the different evolutionary stages. Scale 1:50.000. 23

4.1 Apparent resistivity and phase curves, for the AMT station L03. In this case, the phase curves for both polarization modes are plotted in the first quadrant. Curves obtained with single site processing (left) and remote reference processing (right) are shown for comparison. 36
4.2 Real induction vectors of LMT stations for periods of 10 s, 102 s, 1311 s and 7282 s. 39
4.3 Real induction vectors of AMT stations for periods of 0.0078 s (frequency 128 Hz), 0.083 s (frequency 12 Hz), 2 s, 11 s, 89 s and 1024 s. Yellow triangle shows the position of Lascar volcano. 40
4.4 LMT profile showing the skewness in the definitions of Bahr (above) and Swift (below). White and light tones indicate a skewness below 0.3, as a tentative measure for two-dimensionality. 43
4.5 Skew for six AMT stations according to Swift (blue circles) and Bahr (red triangles) definitions. Note that very high skew values in L01 and L15 between 1 s and 10 s are due to noise. 44
4.6 Strike direction determined for each LMT station and rose diagram calculated for the total period range between 10 s and 10000 s. 46
4.7 Strike direction determined for each LMT station and Rose diagram calculated for a period range between 10 s and 100 s. 46
4.8 Strike direction determined for each LMT station and Rose diagram calculated for a period range between 100 s and 1000 s. 47
4.9 Strike direction determined for each LMT station and Rose diagram calculated for a period range between 1000 s and 10000 s. 47
4.10 Strike direction for the AMT stations calculated for 4 period ranges. 48
4.11 Graphical representation of the phase tensor (Caldwell et al., 2004). 50
4.12 Phase tensor ellipses for the LMT profile normalized by the maximum phase value, color scale represents β. The ellipses are plotted so that the horizontal axis corresponds to an east-west orientation. The segmented line encloses the ellipses with $|\beta| < 5$ 51
4.13 Phase tensor ellipses for the LMT profile normalized by the maximum phase value, color scale represents Φ_{min}. The segmented line encloses the ellipses with a $tan^{-1}\Phi_{min} > 45$, indicating increasing conductivity with depth. 52
4.14 Phase tensor ellipses for the AMT stations normalized by the maximum phase value, color scale represents the $\tan^{-1}\Phi_2$, with $\Phi_2 = \sqrt{\Phi_{max}\Phi_{min}}$. Yellow triangle shows the position of Lascar volcano. 53

5.1 Tradeoff between roughness and RMS. The roughness is controlled by τ indicated in this plot next to the red dots. 56

5.2 2D inversion of LMT data (10 s - 10000 s) measured during the first field campaign in 2007. RMS: 1.759 57

5.3 Starting model for the inversion of LMT data including the sea (red layer, top left) and the Salar de Atacama basin (red layer, top center) as conductive layers, and the subducting slab as a resistive zone (in light blue). 58

5.4 2D inversion of LMT data. (A) 2D inversion of tipper data only, including stations ATA and SAL, RMS: 1.661. (B) 2D inversion of tipper, TE and TM modes, RMS: 1.957. Note that stations ATA and SAL were not considered for the joint inversion shown in the image below, as for these stations no electric fields but only magnetic fields were measured. 59

5.5 Comparison between measured and calculated data from the 2D inversion of TE, TM and tipper shown in figure 5.4 B. Dots are measured data and curves are the data calculated with the 2D inversion program. 60

5.6 Comparison between measured data (dots) and model responses (lines) for station SOC, located in the western border of the volcanic arc for a forward model based on the 2D inversion result shown in figure 5.4 B, without the relatively conductive zone beneath the volcanic arc (enclosed by a segmented line). The black arrow is indicating the slight but perceptible misfit between 100 and 1000 s in the TE curve due to the absence of the relatively conductive zone. 61

5.7 Comparison between measured data (dots) and model responses (lines) for station ARC, located in the Argentinian Puna, for a forward model based on the 2D inversion result shown in figure 5.4 B, with the bottom of the highly conductive zone below the Puna set at (A) 35 km , (B) 55 km and (C) 80 km 62

5.8 Comparison between measured data (dots) and model responses (lines) for station CNE, located in the Domeyko Cordillera, for a forward model based on the 2D inversion result shown in figure 5.4 B, with the highly resistive zone at the western border divided in two parts. Note the larger misfit observed for the TM curve compared with the response of the 2D inversion for the same station, shown in figure 5.5 63

5.9 Discretization of the study area around Lascar, for the development of a 3D forward model. Central part of the grid (approx. 20 x 20 km^2) with a cell size of 500 m x 500 m in the horizontal directions and 100 m in depth for the first layer. 65

5.10 Effect of a conductive anomaly with distance. Conductive block of 1.5 km x 3 km x 1 km and resistivity of 1 Ωm, placed between 500 and 1500 m depth. Results according to the positions shown in A, B and C. Yellow star represents the measuring site. Induction vectors are small and point E-W; therefore they are badly visible. . . 66

5.11 Effect of the relative position between anomaly and station. Conductive block of approx. 4 km x 4 km x 1 km and resistivity of 1 Ωm, placed between 500 and 1500 m depth. Results according to the positions shown in A, B, C and D. Yellow star represents the measuring site. 68

5.12 Effect of a different depth extension and resistivity contrast. Conductive block of approx. 4 km x 4 km horizontal area. Case (A) resistivity of 1 Ωm, placed between 500 and 1500 m depth, case (B) resistivity of 1 Ωm, placed between 500 and 10000 m depth, and case (C) resistivity of 10 Ωm, placed between 500 and 10000 m depth. Yellow star represents the measuring site. 69

5.13 3D model for the topographic effect estimation. View from the south, Lascar and Aguas Calientes volcanoes. 70

5.14 Real data and topographic effect shown as apparent resistivity curves, phase curves and induction vectors for sites L01 and L08. For the curves, dotted lines are real data and continuous lines are modeled data. Cell size of the central part of the model is 500 m x 500 m x 100 m. 71

5.15 Real data and topographic effect shown as apparent resistivity curves, phase curves and induction vectors for sites L01 and L08. For the curves, dotted lines are measured data and continuous lines are modeled data. Cell size of the central part of the model is 100 m x 100 m x 100 m. Note that, as in the previous case, model responses have not much similarity with data, so additional structures are necessary 72

5.16 3D model including a main conductive zone below Lascar volcano. 74

5.17 Comparison between measured data and model response for 3 sites around Lascar for the model shown in figure 5.16. Continuous lines and blue arrows represent the modeled data. 74

5.18 Examples of different modeling attempts with a unique conductive zone beneath the volcano. In these examples the red zones are representing a resistivity of 1 Ωm, green of 100 Ωm and blue of 800 Ωm. 75

5.19 3D model including a conductive zone extending to the S of Lascar. This model includes the Atacama Block and the Salar de Atacama, which are relatively far from the central part of the grid. 76

5.20 3D view from the southeast of the model shown in figure 5.19. The segmented line in image A is marking the zone shown in image B. In this figure only the conductive zones (<30 Ωm) and resistive zones (> 1000 Ωm) are shown. A conductive zone of 1-5 Ωm to the southeast of the volcano is extending 12 km in depth close to it and 25 km in depth further to the south. S-A is the Salar de Atacama, modeled as a thin conductive zone of ∼1 Ωm. A-B is the Atacama block, modeled as a resistive zone starting at 5 km beneath the Salar de Atacama and extending 60 km in depth. No vertical exaggeration. 77

5.21 Comparison between measured data and the response of the model shown in figure 5.19 and for 9 sites around Lascar volcano. Main diagonal elements are not considered here as they are rather noisy and difficult to fit (comes from p. 78). . . . 79

5.22 3D model including a conductive zone extending to the S of Lascar. This model includes the data from 3 new stations measured in early 2010. 80

5.23 3D view of the model shown in figure 5.22. The segmented line in this image is marking the zone shown in figure 5.24. In this figure only the conductive zones (<30 Ωm) and resistive zones (> 1000 Ωm) are shown. Note the presence of the resistive block at the eastern border of the Salar de Atacama reaching 10 km depth. The conductive zone of 1-5 Ωm to the southeast of the volcano is shown in detail in figure 5.24 80

5.24 Detailed view of the model shown in figure 5.23. In this figure only the conductive zones (<30 Ωm) and resistive zones (> 1000 Ωm) are shown. A conductive zone of 1-5 Ωm to the southeast of the volcano is extending 12 km in depth close to it and 25 km further to the south. No vertical exaggeration. 81

5.25 Comparison between measured data and the response of the model shown in figure 5.22 and 5.24 for 9 sites around Lascar volcano (comes from p. 81). 82

5.26 3D model including a conductive zone extending to the S of Lascar, plain view at 2 km depth. Depth extension of the conductive structure reaching 6 km beneath the surface. 83

5.27 3D view from the southeast of the model shown in figure 5.26. The segmented line in image A is marking the zone shown in image B. In this figure only the conductive zones (<30 Ωm) and resistive zones (> 1000 Ωm) are shown. A conductive zone of 1-5 Ωm to the southeast of the volcano is extending 1.5 km in depth close to it and 6 km further to the south. Another conductive zone of 1 Ωm to the east of the volcano is extending between 10 and 70 km depth. No vertical exaggeration. 84

5.28 Comparison between measured data and the response of the model shown in figure 5.26 and 5.27 for 9 sites around Lascar volcano (comes from p. 85). 86

5.29 Result of a 3D inversion with AMT data around Lascar volcano. Red indicates conductive zones (∼1 Ωm), green, intermediate zones (∼100 Ωm) and blue, resistive zones (∼1000 Ωm). The altitude of these plan sections is indicated in the top left corner of each image (consider that the surface is at ∼4000 m). 89

5.30 Apparent resistivity and phase of the off-diagonal elements of the impedance tensor, together with the induction vectors for measured and modeled data for six different sites around Lascar. 90

6.1 Induction vectors at four different periods between 0.0625 s (16 Hz) and 11 s. . . . 93

6.2 Geology of Cuyugas and Allana hills, and its position relative to the AMT sites. Geology extracted from Breitkreuz and Zeil (1994). 94

6.3 Isostatic residual gravity from Götze et al. (1994), showing a gravity high to the north-west, east and south of the Salar de Atacama basin. Salar de Atacama as well as the 3500 m elevation contour line is drawn here for orientation. Edited image extracted from Schurr and Rietbrock (2004). 94

6.4 Extract from the Geological Map of Chile 1:1.000.000 (SERNAGEOMIN, 2002). Units P3l, P3t, Q3l and Q3t are ignimbrites and volcanic units from Pliocene and Quaternary ages; Ms3l are domes of Miocene age and CP2 and Ptrg are Paleozoic volcanic and volcano sedimentary units. 95

6.5 Some of the main faults present around Lascar volcano. In blue, the Olacapato - El Toro fault system inferred from Matteini et al. (2002a), and the Puntas Negras volcanic chain related to it (Matteini et al., 2002a,b). In green, the Miscanti Fault system and its northward prolongation (Aron et al. (2008); González et al. (2009) and F. Aguilera, pers. comm.). The main volcanic centers are named as follows. S: Saltar, La: Lascar, A: Aguas Calientes, C: Corona, T: Tumisa, O: Overo, L: Lejía, Ch: Chiliques, M: Miscanti, Mi: Miñiques. Red squares represent the AMT stations. 96

6.6 View from the SE of the volcanic centers in this area. From the 3D forward modeling, 3 main conductive zones can be identified: zone A, extending from the base of Lascar volcano some hundreds of meters in depth; zone B, covering a wide area and extending to the SE of Lascar, between 1 and 3 km beneath the surface; and zone C, which is at the southern extreme of zone B, but reaching larger depths and resistivities of $\sim$1 Ωm. 98

6.7 Pressure-Temperature plot for Clinopyroxene and Orthopyroxene present in rock samples of the different evolutionary stages of Lascar volcano (André Stechern, pers. comm.). 100

6.8 Gravity profile and density model along a section through the Salar de Atacama at 23°32’S (Reutter et al., 2006). 101

6.9 2D inversion of tipper, TE and TM modes of LMT data, including a roughly approximated Moho from Yuan et al. (2000) and the Wadati-Benioff zone (W-B zone) approximated from Cahill and Isacks (1992). The dashed area beneath the Puna is not resolved. 102

6.10 Cross sections from a 3D tomography showing seismic attenuation (Schurr et al. (2003); B. Schurr, pers. comm.). The LMT profile is located between these two cross sections, (A) at -23.5°S and (B) at -24.2°S 104

6.11 2D inversion result of the LMT profile, and earthquakes locations between 23.5°S and 24°S, from Engdahl and Villaseñor (2002). Resistivity structures beneath 140 km are not resolved and thus not shown in this section. 106

Acknowledgments

I would like to thank Dr. Heinrich Brasse, who gave me the chance to come to Berlin and live in this interesting city, for his friendly support and active guidance through all this work.

Special thanks to Prof. Dr. Serge Shapiro and PD Dr. Oliver Ritter for their time and dedication in the review of this thesis.

I'm very grateful to the members of the geophysics department of the Freie Universität Berlin for creating a good work environment. Also to the magnetotelluric working group of the GFZ Potsdam for the interesting working meetings during these years.

Thanks to the working groups of Prof. Francois Holz from the Institut of Mineralogy of the Leibniz Universität Hannover and of Prof. Gerhard Wörner in the Geochemistry Department of the Geowissenschaftliches Zentrum Göttingen, for the information exchange and interesting feedback.

I am also thankful to Ricardo Alzugaray for the linguistic correction of part of this thesis, and to Ingmar Budach for his help in the translation of the abstract and active participation in the field work.

Many thanks to Dr. Felipe Aguilera and Dr. Andrés Pavez for their assistance in the geology of the Lascar volcano area, and Dr. Guillermo Chong for the helpful information regarding the Salar de Atacama.

I am grateful also to all the people who participated in the field campaigns in North Chile and Argentina, and particularly to Faustino Ticona for his invaluable help and experience.

To my friends and colleagues Dirk Brändlein, Anja Schäfer, and Gerhard Kapinos, I am very grateful for their friendly advice and help during all this time, especially during my first months in Berlin.

To my friends Trau and Ricardo, thanks for always be there. Muchas gracias amigos.

The financial support of the DFG allowed the realization of this investigation, and my participation in international workshops.

Finally, I would like to thank my family, for their love and support before and during this PhD, and among them, to the person who left everything behind to follow me, to my wife for her love, patience and generous determination in sharing all this experience with me. Juntos, juntos para siempre.

Curriculum Vitae

For reasons of data protection,
the curriculum vitae is not included in the online version

For reasons of data protection,
the curriculum vitae is not included in the online version